

FROM TOPOLOGICAL TO ANOMALOUS QUANTUM PHASES IN HYBRID WIRES

Saulius Vaitiekėnas

Ph.D. Thesis

Center for Quantum Devices
Niels Bohr Institute
University of Copenhagen

Academic advisor:
Charles M. Marcus

Assessment committee:
Thomas Sand Jespersen
Hugues Pothier
Yuval Oreg

December 2019

CONTENTS

ABSTRACT	vii
ACKNOWLEDGMENTS	ix
1 SUPERCONDUCTIVITY	1
1.1 Normal State	1
1.2 Microscopic BCS Theory	3
1.3 Superconducting State	4
1.4 Macroscopic Ginzburg-Landau Theory	7
1.5 London Equations	8
1.5.1 Supercurrent Density	8
1.5.2 Hallmarks of Superconductivity	9
1.6 Fluxoid Quantization	10
1.7 Little-Parks Effect	11
1.8 Andreev Reflection	14
1.9 BTK Model	15
1.9.1 Interfacial Scattering	15
1.9.2 Measuring Density of States	18

2	ENTER MAJORANA	21
2.1	From Fermions to Non-Abelian Anyons	21
2.1.1	Fundamental Particles	21
2.1.2	Majorana Zero Modes	22
2.1.3	Exotic Exchange	22
2.2	Hybrid Nanowires	23
2.2.1	Blueprint	23
2.2.2	Topological Phase Transition	27
2.2.3	Spin-Orbit Coupling	28
2.2.4	Chemical Potential and Orbital Effects	30
2.2.5	Full-Shell Nanowires	32
3	EFFECTIVE g FACTOR IN MAJORANA WIRES	35
3.1	g Factor in InAs	35
3.2	Half-Shell Devices	38
3.3	Steplike Decrease	40
3.4	Gap Closing & Reopening	42
3.5	Conclusion	46
4	MAJORANA MODES IN FULL-SHELL WIRES	47
4.1	Wire-Vortex Analogy	48
4.2	Full-Shell Devices	50
4.3	Tunneling Spectroscopy	52
4.4	Coulomb Spectroscopy	55
4.5	Sanity Check	60
4.6	Discussion	62
5	ANOMALOUS PHASE IN DESTRUCTIVE SUPERCONDUCTORS	63
5.1	Small Cylindrical Shells	64
5.2	Pair-Breaking with Temperature & Flux	66
5.3	Current-Driven Phase Transitions	70
5.4	Perpendicular Magnetic Field	71
5.5	Summary	77

6	SELECTIVE AREA GROWN HYBRIDS	79
6.1	Loops & Branches	79
6.2	Electron Distribution in SAG Wires	82
6.3	Thermodynamics of Coulomb Blockade	84
6.4	Coulomb Peak Motion in Field	86
6.5	Field Effect Mobility	88
6.6	Minimal Network	90
6.7	Summary	92
A	APPENDIX MATERIALS & METHODS	95
A.1	Nanowire Growth	95
A.2	Full-Shell Device Fabrication	96
A.3	Selective Area Grown Sample Preparation	97
A.4	Measurement Setup	97
B	APPENDIX COULOMB SPECTROSCOPY	99
B.1	Hybridization Amplitude	99
B.2	Peak Spacing Analysis	100
C	APPENDIX ANOMALOUS PHASE	105
C.1	Full-Shell Wire Parameters	105
C.2	Density of States	107
C.3	Non-Saturating Resistance	107
C.4	Flux-Dependent Resistance Saturation	110
C.5	Outer Segments	113
C.6	Anomalous Phase vs. Mean-Field Theory	113
D	APPENDIX COULOMB BLOCKADE	115
D.1	Free Energy Model	115
D.2	Device Energy	116
	PUBLICATIONS	119
	REFERENCES	121

ABSTRACT

The thesis at hand deals with quantum phase transitions in hybrid semiconductor-superconductor nanowires. After reviewing some concepts of superconductivity, it introduces Majorana zero modes in condensed matter and their realization in hybrid semiconductor-superconductor nanowires.

We begin the experimental part by showing that the effective g factor of Andreev bound states in half-shell wires is a steplike function of gate voltage, that tunes the charge carrier density and improves the hard induced gap. We observe the closing and reopening of the superconducting gap in the subgap spectrum coincident with the appearance of a zero-bias conductance peak.

The following chapter demonstrates a novel means of creating Majorana zero modes in full-shell wires by using magnetic-flux. Around one applied flux, tunneling spectroscopy reveals a gapped region with a discrete zero-energy state, whereas Coulomb peak spacing shows exponentially decreasing deviation from $1e$ periodicity with device length.

We continue with a study of magnetic-flux driven reentrant quantum phase transitions between superconducting and metallic phases in full-shell wires. By tuning axial and transverse magnetic fields we control the crossover between the conventional and destructive Little-Parks regimes bridged by an anomalous metal phase.

The thesis is concluded with a presentation of selective area grown hybrid wires as a basis for topological networks. The novel scalable system displays a hard induced gap, unpoisoned $2e$ -periodic Coulomb blockade, strong spin-orbit coupling and coherence length of several microns.

ACKNOWLEDGMENTS

My biggest thanks goes to Charlie for introducing me to condensed matter physics and its community; for creating all the great opportunities and encouraging me to be daring; for showing that there is always room for improvement and teaching me how to *press on* and *have fun*.

Speaking of great mentors, I would like to thank my dear friend Mingtang—a brilliant scientist and a remarkable human being—for teaching me *Majorana 101* and being an amazing role model.

The years in Copenhagen would not have been as fun without my friends there. *Mange tak* to Fabio for trying to keep everyone young; to Asbjørn for the sophisticated small-talks; to Anders for showing an example of a healthy superposition of $1/\sqrt{2} (|\text{mature}\rangle + |\text{adolescent}\rangle)$; to Filip for the memorable evenings; to Dovydas for the superb impressions; to Shiv for many helpful phone calls; to Judith for never failing to create a cheerful atmosphere; to Alexander for teaching me how to rock'n'roll; and to Sachin for the two efficient jogging sessions. And of course, a *tak* to Abhishek, Damon, Anasua, Lucas, Federico, Antonio, Erikas, Andrew, Esteban, Gerbold, Eoin, Rob, and others for the good company and discussions.

A big *ačiū* to mama Vaida for keeping me on the track; to *tètè* Aleksandras for introducing me to the precision work; to Gintarė for

all the caring; to Monika and Edgaras for the support and letting me crash at their place, and Kotryna for joining me in doing so.

Finally, I would like to take the opportunity and acknowledge valuable discussions with A. E. Antipov, M. Feigel'man, K. Flensberg, L. I. Glazman, T. Karzig, S. Kivelson, R. M. Lutchyn, A. E. Mikkelsen, C. Nayak, Y. Oreg, G. Refael, B. Spivak, B. van Heck, and G. W. Winkler as well as experimental and materials assistance from J. Arbiol, P. Krogstrup, S. Marti-Sanchez, J. Nygård, C. J. Palmstøm, J. E. Sestoft, C. Sørensen, and R. Tanta that contributed greatly to this work.

SUPERCONDUCTIVITY

Due to its intriguing quantum-mechanical nature and diverse potential applications, superconductivity continues to be a fascinating and growing field of research, long after its discovery [1]. This chapter introduces the basic properties of superconductivity and some of the related phenomena.

1.1 NORMAL STATE

In the Landau-Fermi liquid model [2], the ground state of a normal conductor is constructed by filling all the available energy states with electrons up to the characteristic Fermi energy, E_F . In the momentum space, this can be illustrated by a filled sphere with a radius k_F , which defines the Fermi surface [Fig. 1.1(a)]. Adding or removing electrons excites the system to a higher energy state. More specifically, removing an electron with momentum \mathbf{k}_v below the Fermi surface, creates a *hole* excitation with opposite momentum $-\mathbf{k}_v$. Similarly, adding an electron with momentum \mathbf{k}_u above the Fermi surface, creates a *particle* excitation with the same momentum \mathbf{k}_u .

Close to the Fermi surface, the so-called quasi-particle excitations behave effectively as free electrons, hence their electronic wave functions can be described by plane waves

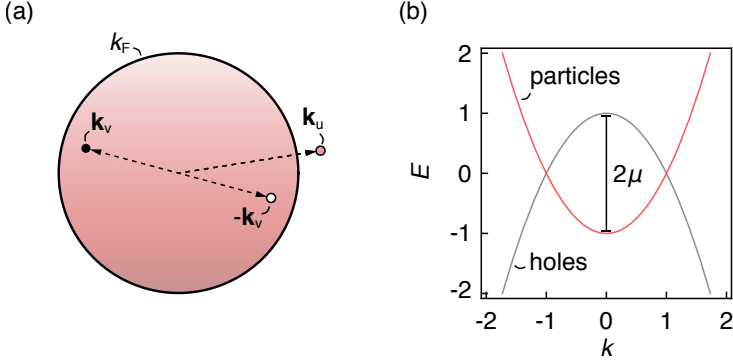


Fig. 1.1: (a) Momentum space representation of the normal ground state. Electrons fill the states below the characteristic Fermi wave-vector, k_F , defining the Fermi surface. The hole excitations (white circle) below the Fermi surface are created by removing an electron (black circle) with an opposite momentum, whereas the particle-like excitations (red circle) are obtained by adding an electron above the Fermi surface. (b) Single quasi-particle spectrum given by Eq. (1.4), with $\hbar^2/m = 2$ and $\mu = 1$.

$$\begin{pmatrix} u_{\mathbf{k}}(\mathbf{r}) \\ v_{\mathbf{k}}(\mathbf{r}) \end{pmatrix} = e^{i\mathbf{k}\mathbf{r}} \begin{pmatrix} u_0 \\ v_0 \end{pmatrix} \quad (1.1)$$

where u_0 and v_0 are the wave amplitudes for the particle and hole excitations, respectively. The single quasi-particle spectrum can be obtained by solving the Schrödinger equation

$$\begin{pmatrix} H(\mathbf{r}) & 0 \\ 0 & -H(\mathbf{r}) \end{pmatrix} \begin{pmatrix} u_{\mathbf{k}}(\mathbf{r}) \\ v_{\mathbf{k}}(\mathbf{r}) \end{pmatrix} = E \begin{pmatrix} u_{\mathbf{k}}(\mathbf{r}) \\ v_{\mathbf{k}}(\mathbf{r}) \end{pmatrix} \quad (1.2)$$

with the single quasi-particle Hamiltonian defined as

$$H(\mathbf{r}) = -\frac{\hbar^2}{2m}\partial_{\mathbf{r}}^2 - \mu \quad (1.3)$$

where \hbar is the reduced Planck constant, m is the effective mass, $\partial_{\mathbf{r}}$ is the partial derivative with respect to the spatial coordinate \mathbf{r} and μ is the chemical potential, which at zero temperature equals E_F . The corresponding energy eigenvalues, given by

$$E = \pm \left(\frac{\hbar^2 k^2}{2m} - \mu \right) \quad (1.4)$$

are illustrated in Fig. 1.1(b).

1.2 MICROSCOPIC BCS THEORY

In the early 1950s, inspired by experimental observations [3, 4], John Bardeen argued in his seminal work [5] that superconductivity is mediated via electron-phonon interactions. In a semi-classical picture, this can be illustrated by an electron propagating through a metal attracting neighboring positive lattice ions, which in turn attract other electrons, effectively creating electron-electron bound pairs. These were indeed stimulating ideas, however, suffering from mathematical limitations they failed to properly describe superconductivity.

While studying superconductivity, in 1956, Leon N. Cooper considered two interacting electrons with opposite momenta (and spins) above the Fermi surface (Fig. 1.2 and Ref. [6]). He found that in case of attractive interactions, the two electrons form an energy-lowering bound state. Cooper theorized that such pairs are responsible for superconductivity, but the complete proof was still lacking.

Early in the following year, J. Robert Schrieffer realized that a collection of the so-called Cooper pairs in a superconductor can be

described with one single wave function, which combined with the ideas of Bardeen and Cooper gave rise to the microscopic theory of superconductivity [7], usually referred to as the BCS theory.

1.3 SUPERCONDUCTING STATE

For the excitation close to the Fermi surface, the annihilation of a hole with momentum $-\mathbf{k}_v$ is, in a sense, equivalent to the creation of a particle with an opposite momentum \mathbf{k}_u that is approximately equal to \mathbf{k}_v [Fig. 1.2(a)]. As a result, the ground state of the superconductor can be considered as a linear superposition of states with occupied and unoccupied Cooper pairs. This coupling between the particles and holes modifies the single quasi-particle spectrum considerably.

To describe the hybridization between the different excitations one can introduce a pairing potential $\Delta(\mathbf{r})$ into the normal state particle and hole Eq. (1.2). The resulting Bogoliubov-de Gennes equations, as they are called, are given by [8]

$$\begin{pmatrix} H(\mathbf{r}) & \Delta(\mathbf{r}) \\ \Delta^*(\mathbf{r}) & -H(\mathbf{r}) \end{pmatrix} \begin{pmatrix} u_{\mathbf{k}}(\mathbf{r}) \\ v_{\mathbf{k}}(\mathbf{r}) \end{pmatrix} = E \begin{pmatrix} u_{\mathbf{k}}(\mathbf{r}) \\ v_{\mathbf{k}}(\mathbf{r}) \end{pmatrix} \quad (1.5)$$

In general, $\Delta(\mathbf{r})$ —referred to as the order parameter or simply as the superconducting energy gap—can fluctuate in space. Roughly speaking, the length scale over which the superconducting gap can vary is given by the distance between two electrons forming a Cooper pair called the coherence length, ξ [9]. For typical superconductors, ξ is of the order micrometers. Therefore, for a homogeneous, macroscopic scale superconductors, the order parameter can be assumed to be constant in space, in which case it is given by

$$\Delta = |\Delta|e^{i\varphi} \quad (1.6)$$

where $|\Delta|$ is the magnitude of the superconducting gap and φ is the

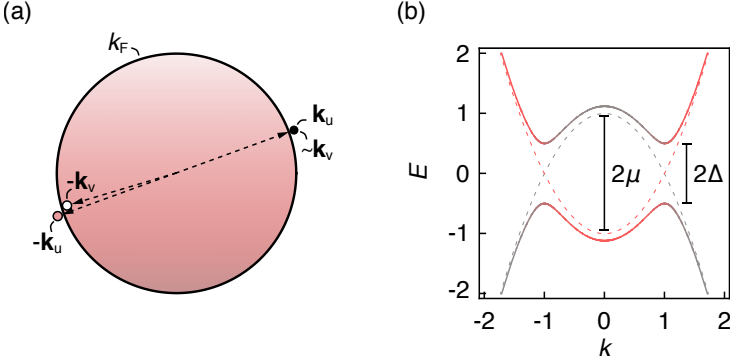


Fig. 1.2: (a) Illustration of the Cooper problem: in the single particle picture, an excitation in a superconductor can be composed out of two particle-like excitations with opposite momenta \mathbf{k}_u and $-\mathbf{k}_u$, just above the Fermi surface. For the excitations close to the Fermi surface, annihilation of a hole with momentum $-\mathbf{k}_v$ resembles the creation of a particle with a nearly equal, but opposite momentum $\mathbf{k}_u \sim \mathbf{k}_v$. (b) Single particle dispersion relation with superconducting pairing potential Δ , described by Eq. (1.7), with $\hbar^2/m = 2$, $\mu = 1$ and $\Delta = 0.5$ (solid lines), and $\hbar^2/m = 2$, $\mu = 1$ and $\Delta = 0$ [dashed lines, same as Fig. 1.1(b)]. The line-shading illustrates the particle (red) and hole (gray) weights.

global phase of the superconductor wave function [10].

Keeping this in mind, the Bogoliubov-de Gennes Eqs. (1.5) together with the plane-wave solution [Eq. (1.1)] yield energy eigenvalues of the form

$$E = \pm \sqrt{\varepsilon_{\mathbf{k}}^2 + |\Delta|^2} \quad (1.7)$$

where $\varepsilon_{\mathbf{k}} = \hbar^2 k^2 / 2m - \mu$ is the single particle energy relative to the Fermi level. The energy spectrum displays a gapped dispersion relation with the lowest single particle excitation energy $\pm |\Delta|$ [Fig. 1.2(b)].

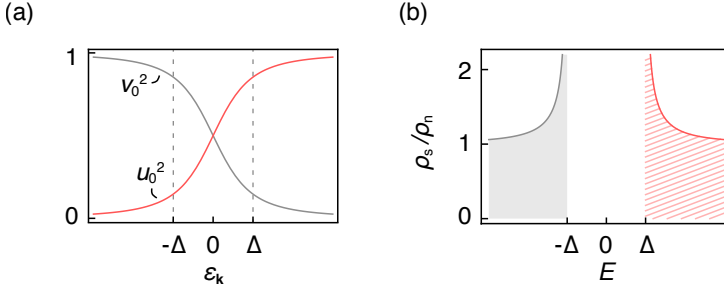


Fig. 1.3: (a) The BCS wave-function probabilities for the particle (u_0^2) and hole (v_0^2) components [given by Eqs. (1.8)] as a function of the single-particle energy relative to the Fermi energy, $\varepsilon_{\mathbf{k}} = \hbar^2 k^2 / 2m - \mu$. Both occupation fractions are non-zero at zero energy illustrating the mixing between particle and hole excitation in the superconducting state. (b) The single quasi-particle density of states, ρ_s , in the superconducting state as a function of energy, E , where ρ_n is the density of states in the normal state.

For a better intuition, it is informative to look at the single quasi-particle weights of the superconducting excitation. The normalization condition $u_0^2 + v_0^2 = 1$ together with Eqs. (1.5) and (1.7) yield the probabilities for the superconducting excitation to be particle- or hole-like [8, 10]

$$u_0^2 = \frac{1}{2} \left(1 + \frac{\sqrt{E^2 - |\Delta|^2}}{E} \right) \quad \text{and} \quad v_0^2 = 1 - u_0^2 \quad (1.8)$$

which are illustrated in Fig. 1.3(a). Contrary to the normal state ($\Delta = 0$), both u_0^2 and v_0^2 are finite within approximately $\pm|\Delta|$ around the Fermi energy ($\varepsilon_{\mathbf{k}} = 0$).

Finally, the single quasi-particle superconducting density of states

[Fig. 1.3(b)] can be deduced using Eq. (1.7)

$$\rho_s = \frac{dN}{dE} = \frac{dN}{d\varepsilon_{\mathbf{k}}} \frac{d\varepsilon_{\mathbf{k}}}{dE} = \rho_n \frac{E}{\sqrt{E^2 - |\Delta|^2}} \quad (1.9)$$

with the normal density of states $\rho_n = dN/d\varepsilon_{\mathbf{k}}$ and the number of occupied states below the Fermi energy N .

1.4 MACROSCOPIC GINZBURG-LANDAU THEORY

It is important to note that pair formation is not sufficient to compose a superconducting ground state. The rigidity of the superconducting state arises from the bosonic nature of the Cooper pairs (integer effective spin) allowing them to condense into a single coherent quantum state with a global phase. In certain situations, however, spatial inhomogeneity can give rise to new phenomena, where the fully microscopic treatment becomes rather complicated. In such cases, it is advantageous to invoke a more macroscopic description of superconductivity.

In 1950, Vitaly Ginzburg and Lev D. Landau developed a phenomenological theory of superconductivity that accounted for spatial variation of both the magnetic field and the order parameter [11]. In 1959, after the BCS theory was published, Lev P. Gor'kov showed that the Ginzburg-Landau theory is derivable as a limiting case of the microscopic theory [12].

The macroscopic superconductor wave function is defined as

$$\psi(\mathbf{r}, t) = |\psi(\mathbf{r}, t)| e^{i\varphi(\mathbf{r}, t)} \quad (1.10)$$

where $|\psi(\mathbf{r}, t)|^2$ is the electric-charge density of the Cooper pairs. Note that in some literature $|\psi(\mathbf{r}, t)|^2$ is defined as the particle density. For the purpose of this work, the macroscopic wave function can be thought of as a generalization of Eq. (1.6), accounting for the spatial and time dependence of both the superconducting gap and phase.

1.5 LONDON EQUATIONS

1.5.1 Supercurrent Density

Global phase coherence has far-reaching consequences for the superconductor nature in electric (\mathbf{E}) and magnetic (\mathbf{B}) fields. Many of these characteristics can be derived by solving the time-dependent Schrödinger equation for a charged particle in an electromagnetic field. With the appropriate Hamiltonian, the equation is given by

$$i\hbar\partial_t\psi(\mathbf{r}, t) = \frac{1}{2m} (-i\hbar\partial_{\mathbf{r}} - q\mathbf{A})^2 \psi(\mathbf{r}, t) - \mu\psi(\mathbf{r}, t) \quad (1.11)$$

Here ∂_t is the partial derivative with respect to time, \mathbf{A} is the vector potential and q is the charge of the particle, which for Cooper-pairs equals $2e$. Substituting $\psi(\mathbf{r}, t)$ with Eq. (1.10) and abbreviating $|\psi(\mathbf{r}, t)| = |\psi|$ as well as $\varphi(\mathbf{r}, t) = \varphi$, the real part of Eq. (1.11) (after some algebraic acrobatics) can be written as [13]

$$-\hbar|\psi| \partial_t\varphi = -\frac{\hbar}{2\pi} \left[\partial_{\mathbf{r}}^2 - \left(\partial_{\mathbf{r}}\varphi + \frac{2e}{\hbar}\mathbf{A} \right)^2 \right] |\psi| - \mu|\psi| \quad (1.12)$$

The imaginary part, multiplied by $|\psi|$, can be massaged into the form of the continuity equation

$$\begin{aligned} \partial_t\rho_s + \partial_{\mathbf{r}}\mathbf{j}_s = \\ \partial_t|\psi|^2 + \partial_{\mathbf{r}} \left[\frac{\hbar}{m} |\psi|^2 \left(\partial_{\mathbf{r}}\varphi - \frac{2e}{\hbar}\mathbf{A} \right) \right] = 0 \end{aligned} \quad (1.13)$$

with the aforementioned charge density $\rho_s = |\psi|^2$ and the electric

current density

$$\mathbf{j}_s = \frac{\hbar}{m} |\psi|^2 \left(\partial_r \varphi - \frac{2e}{\hbar} \mathbf{A} \right) \quad (1.14)$$

1.5.2 Hallmarks of Superconductivity

For a homogeneous, bulk superconductor with a constant density and constant phase, Eq. (1.14) simplifies to

$$\mathbf{j}_s = -\frac{2e}{m} |\psi|^2 \mathbf{A} \quad (1.15)$$

The time derivative of the supercurrent density (known as the first London equation [14])

$$\partial_t \mathbf{j}_s = \frac{2e}{m} |\psi|^2 \mathbf{E} \quad (1.16)$$

implies that the supercurrent is non-dissipative, explaining the perfect conductivity—the first hallmark of superconductivity [1].

The curl of the supercurrent density

$$\partial_r \times \mathbf{j}_s = -\frac{2e}{m} |\psi|^2 \mathbf{B} \quad (1.17)$$

is known as the second London equation [14]. Together with Ampere's law and Gauss's law for magnetism

$$\partial_r \times \mathbf{B} = \mu_0 \mathbf{j}_s \quad \& \quad \partial_r \mathbf{B} = 0 \quad (1.18)$$

Eq. (1.17) yields

$$\partial_r^2 \mathbf{B} = -\frac{2e \mu_0}{m} |\psi|^2 \mathbf{B} = -\frac{1}{\lambda^2} \mathbf{B} \quad (1.19)$$

with the magnetic constant μ_0 and the London penetration depth λ . The second-order differential Eq. (1.19) indicates that the amplitude

of the magnetic field decays exponentially inside the superconductor and otherwise is expelled from its interior. The so-called Meissner effect [15] explains the perfect diamagnetism—the second hallmark of superconductivity.

1.6 FLUXOID QUANTIZATION

In superconductors that enclose a non-superconducting region (for example rings or cylinders), due to the single-valuedness of the wave function, the superconducting phase can change only by integer multiples of 2π , while winding around the non-superconducting region. The number of the phase windings around a hole is called fluxoid quantum [16]. Mathematically, the fluxoid can be defined as the phase that $\psi(\mathbf{r}, t)$ acquires along a closed contour, which [using Eq. (1.14)] is given by [10]

$$\frac{\hbar}{2e} \oint \partial_{\mathbf{r}} \varphi \, d\mathbf{r} = \oint (\lambda^2 \mu_0 \mathbf{j}_s + \mathbf{A}) \, d\mathbf{r} \quad (1.20)$$

For a contour c that encloses a surface s with a surface element ds the second term on the right hand side of Eq. (1.20) (using Stokes' theorem) becomes

$$\oint_c \mathbf{A} \, d\mathbf{r} = \int_s (\partial_{\mathbf{r}} \times \mathbf{A}) \, ds = \int_s \mathbf{B} \, ds = \Phi_c \quad (1.21)$$

where Φ_c is the magnetic flux that threads the surface s enclosed by the contour c .

Due to the single valuedness of the wave function, the left hand side of Eq. (1.20) has to vanish for any contour c_0 that does not enclose a hole. Differently put, the fluxoid equals zero for every contour that can be retracted to a point [Fig. 1.4(a)]. On the other hand, if a contour c_1 encircles a hole it can only be shrunk to the outline of the hole [Fig. 1.4(b)]. In this case the fluxoid does not have

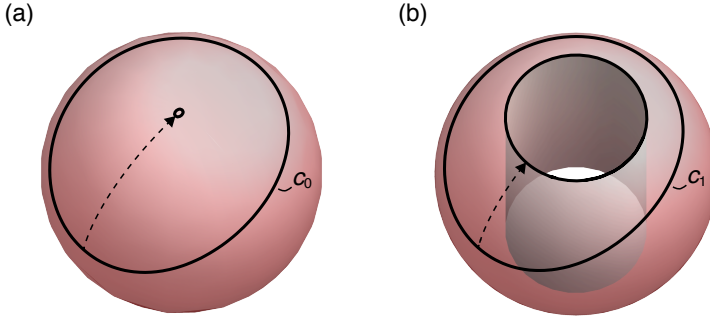


Fig. 1.4: (a) The fluxoid—given by Eq. (1.20)—is ill-defined for any contour c_0 in a superconductor (sphere) that does not enclose any holes. (b) For any contour c_1 around a given hole (cylinder), the fluxoid equals $\Phi_0 n$ —integral multiples of the flux quantum.

to vanish. In general, the fluxoid can be expressed by

$$\frac{\hbar}{2e} \oint \partial_r \varphi \, d\mathbf{r} = \frac{\hbar}{2e} 2\pi n = \Phi_0 n \quad (1.22)$$

where $\Phi_0 = h/2e$ is the flux quantum and n is an integer corresponding to the number of phase windings around the hole.

It is interesting to note, that the supercurrent density is zero [$\mathbf{j}_S = 0$ in Eq. (1.20)] in the bulk of a superconductor with dimensions much larger than the London penetration depth, λ . As a result, the fluxoid is equal to the magnetic flux; in the bulk limit they are both quantized.

1.7 LITTLE-PARKS EFFECT

Consider a thin-walled ($< \lambda$) superconducting ring with radius R , in an external magnetic field through the ring of a magnitude B . The flux associated with the field, $\Phi = \pi R^2 B$, induces a supercurrent with kinetic energy, which reduces the relative free energy of the

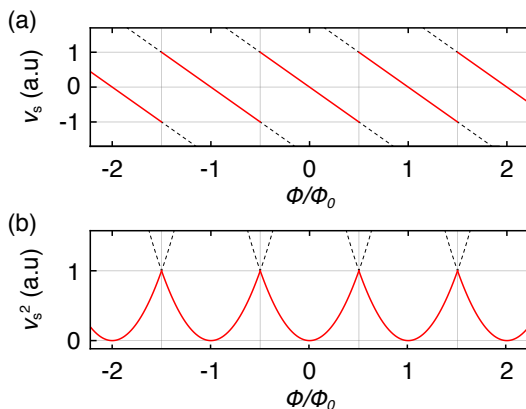


Fig. 1.5: (a) Induced supercurrent velocity v_s and (b) kinetic energy proportional to v_s^2 as a function of normalized flux Φ/Φ_0 threading a superconducting ring. The red curves indicate the ground state, whereas the black dashed lines show the possible excited states.

superconducting state. Since Cooper pairs are all condensed in the same state, the supercurrent velocity equals the ratio of the supercurrent density and the charge density of the Cooper pairs [8]

$$\mathbf{v}_s = \mathbf{j}_s / |\psi|^2 \quad (1.23)$$

which together with Eqs. (1.20)–(1.22) leads to

$$v_s = \frac{\hbar}{mR} \left(n - \frac{\Phi}{\Phi_0} \right) \quad (1.24)$$

For a fixed Φ there are infinitely many discrete values that v_s can take; due to energy minimization, however, the superconducting ring will favour the integer n for which v_s is minimal, corresponding to the ground state. As a result, v_s is a periodic function of Φ/Φ_0 as shown in Fig. 1.5(a). The kinetic energy of the supercurrent is proportional

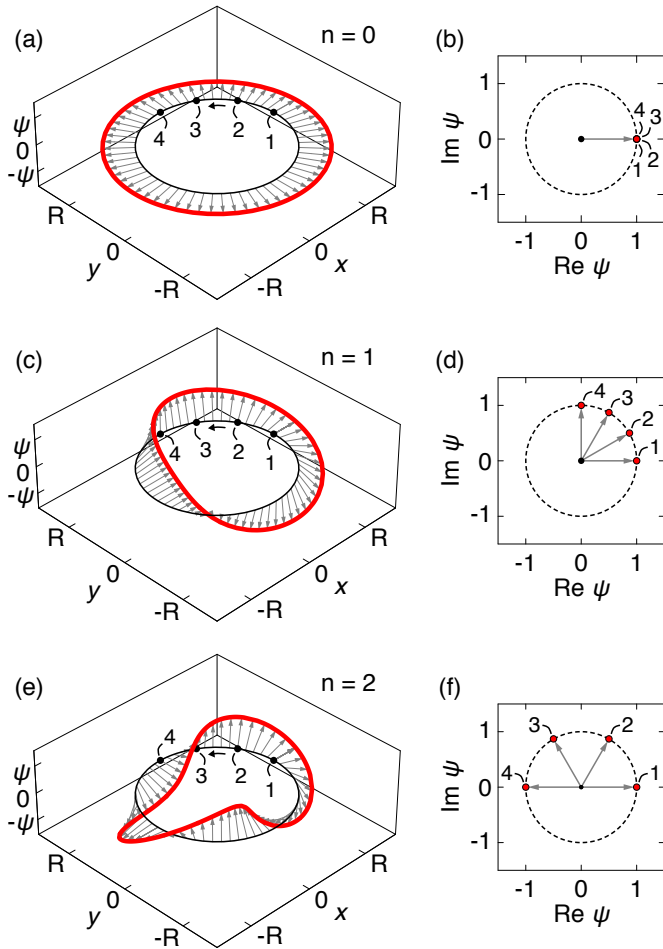


Fig. 1.6: (a) Schematic representation of the superconducting ring (black) with radius R and the evolution of the macroscopic wave function (red) $\psi(\mathbf{r}) = |\psi|e^{i\varphi(\mathbf{r})}$ at a fixed time along the ring at $n = 0$ fluxoid quanta. (b) Polar representation of the complex wave function at four points on the ring marked in (a). (c) and (d) as well as (e) and (f) are similar to (a) and (b) but for $n = 1$ and $n = 2$, respectively.

to v_s^2 [Fig. 1.5(b)]. The oscillatory kinetic energy competes with the superconducting condensation energy, resulting in the Little-Parks effect—periodic modulation of the order parameter, Δ , and the superconducting transition temperature, T_C , with flux.

To maximize the relative free energy of the superconducting state, the fluxoid quantum number n changes around odd half-integer multiple of Φ_0 as the flux is varied. In turn, the number of the phase windings in the macroscopic wave function changes, as illustrated in Fig. 1.6. For $n = 0$, the superconducting phase, φ , is constant around the superconducting ring; without loss of generality $\psi(\mathbf{r}, t)$ can be chosen to be real. For $n = 1$, $\psi(\mathbf{r}, t)$ winds once around the circumference of the ring; the azimuthal angle and φ are in phase. For $n = 2$, there are two twists in $\psi(\mathbf{r}, t)$ around the ring.

1.8 ANDREEV REFLECTION

The proximity effect at the interface between the normal and superconducting phases allows the superconducting wave function to leak into the normal side of the interface. The induced superconducting order parameter in the normal phase decays on a length scale of the coherence length, ξ . At the heart of the proximity effect is the Andreev reflection—a quantum-mechanical scattering process that is responsible for converting single-particle states from a normal metal to Cooper pairs in the superconducting condensate.

First suggested by Alexander F. Andreev in 1964 [18], the unusual scattering considers an incident particle at the normal side of the interface between the two phases [Fig. 1.7(a)]. Because of the energy gap, Δ , in the superconductor, the transfer of single particles with an energy below the gap, $E < \Delta$, is forbidden. However, in the absence of conventional scattering, which is often the case for a very pristine interface, the incoming electron has to be transferred into the superconductor. This is only possible if the electron pairs up with a second electron at the interface forming a Cooper pair. The charge

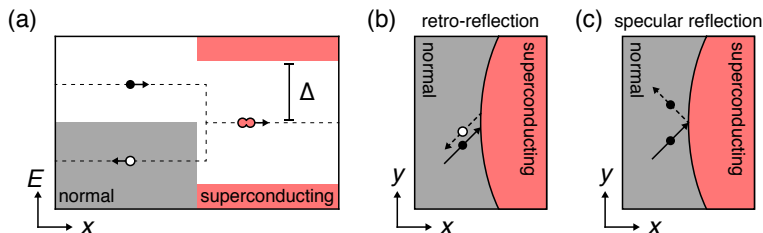


Fig. 1.7: (a) Schematic representation of the Andreev reflection at the interface between the normal (left) and superconducting (right) regions. An incident particle (black) enters the superconductor as a Cooper pair (red) by pairing up with a second electron and retro-reflecting a hole (white) at the interface. (b) and (c) Trajectory of a particle undergoing an Andreev retro-reflection in (b) and normal specular reflection in (c) at the interface between the normal and superconducting phases.

and momentum of this process are conserved by retro-reflecting a hole back into the normal region [Fig. 1.7(b)].

It is interesting to note, that a sequence of Andreev reflections, for example in a normal conductor sandwiched between two superconductors, can lead to standing, single-particle waves termed Andreev bound states (ABS).

1.9 BTK MODEL

1.9.1 Interfacial Scattering

In case of a clean normal-superconductor contact and low energy ($E < \Delta$) incident particles, the only scattering process allowed is Andreev reflection. This is, however, not a general scenario. For a less-transparent interface, normal specular reflection can also take

place [Fig. 1.7(c)]. Furthermore, the probability of Andreev reflection decreases for particles with higher incident energy, as the single-particle channel opens up at $E > \Delta$. A detailed study of the electrical transport across a normal-superconductor interface as a function of its transparency and incident particle energy was first put forward in 1982 by Greg Blonder, Michael Tinkham, and Teun Klapwijk [19].

The BTK model, as it is called, considers an effectively one-dimensional normal-superconductor junction with a repulsive potential $V(x) = \hbar v_F Z \delta(x)$, that accounts for any essential scattering at the interface, where Z is a dimensionless parameter characterizing the height of the potential. The system is described by the Bogoliubov-de Gennes Eqs. (1.5) with

$$H(x) = -\frac{\hbar^2}{2m} \partial_x^2 - \mu + V(x) \quad (1.25)$$

and $\Delta(x) = 0$ for $x < 0$, $\Delta(x) = \Delta$ for $x > 0$.

The direction of a quasi-particle propagation is determined by the group velocity $v_i = dE_i/d\hbar k_i$, where $i = \{N, S\}$ denote the energy eigenvalues (E_i) and momenta (k_i) on either the normal (N) or the superconducting (S) side of the barrier.

Consider an incident normal particle with a positive group velocity $v_N \sim v_F$ and a plane wave solution

$$\psi_{\text{in}}(x) = \begin{pmatrix} 1 \\ 0 \end{pmatrix} e^{ik_F x} \quad (1.26)$$

see Fig. 1.8. The reflected (negative v_N) and transmitted (positive v_S) excitations can be described by

$$\psi_{\text{r}}(x) = a \begin{pmatrix} 0 \\ 1 \end{pmatrix} e^{ik_F x} + b \begin{pmatrix} 1 \\ 0 \end{pmatrix} e^{-ik_F x} \quad (1.27)$$

$$\psi_{\text{t}}(x) = c \begin{pmatrix} u_0 \\ v_0 \end{pmatrix} e^{ik_F x} + d \begin{pmatrix} v_0 \\ u_0 \end{pmatrix} e^{-ik_F x} \quad (1.28)$$

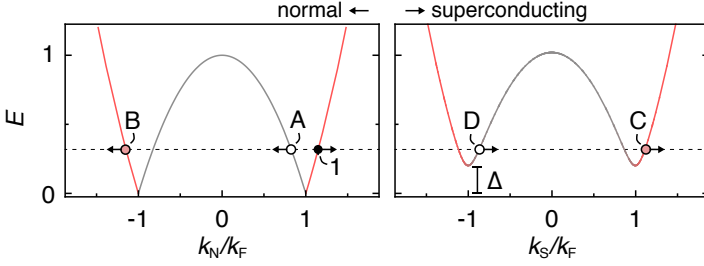


Fig. 1.8: Schematic representation of dispersion relations at normal-superconducting interface. An incoming normal particle (1) can be reflected back as a hole (A) or a particle (B), as well as transmitted through as a particle-like (C) or hole-like (D) excitation. The arrows indicate the direction of the group velocity. For $E < \Delta$, no single particle solutions exist in superconductor hence $C = D = 0$. The spectra were computed using Eqs. (1.4) and (1.7) with $\hbar^2/m = 2$, $\mu = 1$ and $\Delta = 0.2$ for the superconducting side. The line-shading illustrates the particle (red) and hole (gray) weights.

with the BCS coherence factors u_0 and v_0 given by Eq. (1.8). The energy-dependent scattering probabilities $A = a^*a$ of Andreev and $B = b^*b$ of normal reflections, as well as $C = c^*c(u_0^2 - v_0^2)$ of particle-like and $D = d^*d(u_0^2 - v_0^2)$ of hole-like transmissions (Fig. 1.8) can be calculated by applying the boundary conditions at $x = 0$ [20]. Note that for the transmission probabilities an additional factor of $(u_0^2 - v_0^2)$ arises due to the different group velocities in the normal and superconducting phases [19]. Imposing the conservation of probabilities, $A + B + C + D = 1$, the probability solutions are summarized in Table 1 as a function of incident particle energy E , barrier height Z and superconducting gap Δ .

	$E < \Delta$	$E > \Delta$
A	$\frac{\Delta^2}{E^2 + (\Delta^2 - E^2)(1 + 2Z^2)^2}$	$\frac{\Delta^2}{\Gamma^2}$
B	$1 - A$	$\frac{4Z^2(1 + Z^2)(E^2 - \Delta^2)}{\Gamma^2}$
C	0	$\frac{2(1 + Z^2)\sqrt{E^2 - \Delta^2}(E + \sqrt{E^2 - \Delta^2})}{\Gamma^2}$
D	0	$\frac{2Z^2\sqrt{E^2 - \Delta^2}(E - \sqrt{E^2 - \Delta^2})}{\Gamma^2}$

Table 1: Scattering probabilities for an incoming normal particle at the normal-superconducting boundary. A and B are the probabilities of Andreev and normal reflections back to the normal region, whereas C and D are the probabilities of transmissions into the superconductor as particle-like and hole-like excitations, respectively. $\Gamma^2 = (E + (1 + 2Z^2)\sqrt{E^2 - \Delta^2})^2$.

1.9.2 Measuring Density of States

According to the Landauer formula [21] a voltage V across a channel generates a current [22]

$$I = \frac{G_0}{e} \int T(E) [f_0(E - eV) - f_0(E)] dE \quad (1.29)$$

where G_0 is the conductance quantum, e is the elementary charge, $T(E)$ is the transmission probability and $f_0(E)$ is the Fermi function. For a scattering-free normal region $T(E)$ is unity. At the normal-superconducting interface $A(E)$ effectively increases the transmission probability, whereas $B(E)$ reduces it. Furthermore, at low temperatures, the difference Fermi-functions reduces to $\delta(E - eV)$. As a result, voltage-derivative of Eq. (1.29), that is the differential conductance,

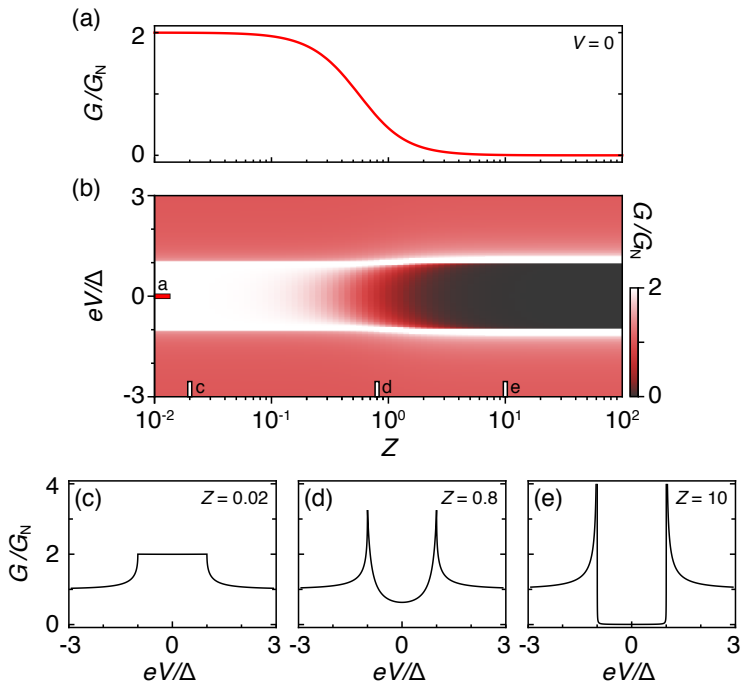


Fig. 1.9: (a) Differential conductance, G , normalized to the normal-state value, G_N , as a function of the dimensionless barrier height Z computed at zero voltage, $V = 0$. (b) Conductance as a function of V across the normal-superconducting interface and Z , constructed using Eq. (1.30) (c)–(e) Conductance cuts from (b) showing the evolution of $G(V)$ from open (low Z) to tunneling (high Z) regime. For high barriers $G(V) \propto \rho_s(eV)$.

can be expressed as

$$G(V) \equiv \frac{dI}{dV} = G_0 [1 + A(eV) - B(eV)] \quad (1.30)$$

which for $eV \gg \Delta$ corresponds to the normal state conductance $G_N = G_0/(1 + Z^2)$. The evolution of $G_{NS}(V)$ with Z is illustrated in Fig. 1.9.

Finally, for a strong barrier ($Z \gg 1$), Eq. (1.30) together with the reflection probabilities from Table 1 and superconducting density of states [Eq. (1.9)] simplifies to the celebrated BTK expression

$$G(V) = G_N \frac{E}{\sqrt{E^2 - \Delta^2}} = \frac{G_N}{\rho_n} \rho_s(eV) \quad (1.31)$$

implying that the differential tunneling conductance between the normal and superconducting contacts is a direct measure of the superconducting density of states.

ENTER MAJORANA

As condensed matter analogs of Majorana fermions—particles that are their own antiparticles [23]—Majorana bound states are predicted to exhibit non-abelian braiding statistics [24,26], providing naturally fault-tolerant qubits [25,27]. This chapter introduces some of the Majorana mode phenomenology and a proposal for their physical realization.

2.1 FROM FERMIONS TO NON-ABELIAN ANYONS

2.1.1 *Fundamental Particles*

Electrons are particles with charge, hence their description requires complex wave functions. With this in mind, in 1928, Paul A. M. Dirac correctly predicted the existence of positrons [28], the antiparticles of electrons [29], and laid the foundation for the concept of antimatter. An ingenious idea put forward by Ettore Majorana in 1937 demonstrated that real wave functions can describe charge-neutral fermions, that are their own antiparticles [23]. A few fundamental particles have been suggested as candidates to satisfy this condition, however, due to the lack of decisive experimental evidence the pursuit of Majorana fermions in high-energy physics remains a subject of ongoing research [30].

2.1.2 *Majorana Zero Modes*

In condensed matter, on the other hand, certain systems can host exotic quasi-particle excitations that are analogs to the Majorana fermions—they are their own quasi-holes. In the normal state, particles and holes do not fit the description as they are oppositely charged (see Section 1.1). Excitons—particle-hole bound states—have zero net charge and are their own antiparticles; however, they also have integer spin and therefore are effectively bosonic excitations.

The picture is different in the superconducting state: the clear distinction between particles and holes is smeared out by the superconducting condensate (see Section 1.3). Here, the elementary-particle excitations above the ground state are neutral fermions described by a superposition of particle- and hole-like excitations [31]. Strictly speaking, the weights for the particle (u_0) and hole (v_0) components are in general different [Eq. (1.8)] and therefore such excitations are not Majorana modes either. Nevertheless, the conditions for $u_0 = v_0$ can be engineered by careful consideration. For instance, Majorana-like excitations can be trapped in certain types of superconducting vertices [30, 32]. Due to the particle-hole symmetry in superconductors, Majorana modes have zero energy.

2.1.3 *Exotic Exchange*

Majorana zero modes (MZMs), as they are called, are known to emerge at the boundaries of one- and two-dimensional superconductors with effectively spinless (p-wave) pairing [33], contrary to the conventional (s-wave) pairing discussed in Section 1.3. Mathematically, two MZMs combine into a single quasi-particle excitation. The resulting fermionic state is two-fold degenerate in energy and can be either occupied or empty. This has peculiar implications on the interchange of two MZMs [34].

In two spatial dimensions, quasiparticles—not restricted to follow fermionic or bosonic statistics—are termed anyons [35]. In the

simplest case, upon exchanging two indistinguishable *abelian* anyons, the corresponding two-particle wave function acquires a complex phase prefactor $e^{i\theta}$, that can vary between -1 and 1 ($\theta = \pi$ for fermions and $\theta = 2\pi$ for bosons) [36]. Majorana modes, that comprise a single, non-local fermionic excitation, are the so-called *non-abelian* anyons, which follow rather exotic exchange statistics: a swap of two MZMs not only develops a phase for the two-particle wave function but can rotate it within the ground-state manifold while maintaining the same particle configuration [37]. Due to these properties, Majorana excitations in condensed matter are thought to be useful for fault-tolerant quantum computing [38, 39].

2.2 HYBRID NANOWIRES

Quantum Hall states with even-denominator fractional filling were the first theorized realization of MZMs proposed in the early 1990s [40]; the experimental verification, however, has proven itself to be rather elusive [41]. The search of MZMs got a boost, when, in 2008, Liang Fu and Charles L. Kane showed that the surface of a topological insulator coupled to an ordinary s-wave superconductor mimics the properties of a $p+ip$ superconductor [42]. After several simplifying suggestions [43], a recipe for realization of MZMs in one-dimensional wires with p-wave pairing was put forward in two back-to-back publications by Roman Lutchyn *et al.* [44] and Yuval Oreg *et al.* [45].

2.2.1 Blueprint

The idea behind the proposed recipe is to design a system whose Hamiltonian would resemble that of a p-wave superconductor. It is, in a sense, natural to take electrons with s-wave pairing and force their spins to align into an effectively spinless channel. To localize the Majorana modes, one spatial dimension is favored, leading to the natural choice of nanowire systems.

With this in mind, consider a one-dimensional, semiconducting nanowire with strong spin-orbit interaction, proximity coupled to an s-wave superconductor and placed in an external magnetic field [Fig. 2.1(a)]. The coordinate system is chosen such that the wire lays along the y -axis, parallel to the particle momentum $\mathbf{p} = \hbar\mathbf{k}$. The superconductor covers the top half of the wire, such that the electrostatic field, \mathbf{E} , points along the z -axis. The resulting Rashba spin-orbit field, $\mathbf{B}_{\text{so}} \propto \mathbf{E} \times \mathbf{k}$ (arising from the relativistic spin-orbit interaction and asymmetry of the crystal potential [46]) is antiparallel the x -axis [Fig. 2.1(b)]. The proximity induced gap is assumed to be homogeneous and equal to the parent superconducting gap, Δ . The external magnetic field \mathbf{B} is oriented along the wire, that is the y -axis. The effective, single-particle Hamiltonian describing the wire reads

$$H = \left(\frac{\hbar^2 k^2}{2m} - \mu \right) \tau_z + \alpha k \sigma_x \tau_z + E_Z \sigma_y + \Delta \tau_x \quad (2.1)$$

where τ_i and σ_i are the Pauli matrices acting in particle-hole and spin spaces, respectively; α is the spin-orbit strength; $E_Z = g\mu_B B/2$ is the Zeeman energy, with the effective g factor, Bohr magneton μ_B and the amplitude of the external magnetic field B . The corresponding eigenenergies, given by

$$E^2 = \varepsilon_{\mathbf{k}}^2 + (\alpha k)^2 + E_Z^2 + \Delta^2 \pm 2\sqrt{(\alpha k)^2 \varepsilon_{\mathbf{k}}^2 + E_Z^2 \Delta^2 + E_Z^2 \varepsilon_{\mathbf{k}}^2} \quad (2.2)$$

with $\varepsilon_{\mathbf{k}} = \hbar^2 k^2 / 2m - \mu$, are illustrated in Fig. 2.1, by introducing one term after the other. The spin orientations are illustrated semi-classically by a total magnetic field $\mathbf{B}_{\text{so}} + \mathbf{B}$. The weights of the particle- and hole-like excitations are illustratively shaded in red and gray, respectively.

The first term in Eq. (2.1) describes the kinetic energy of the electrons in the wire and is discussed in Section 1.1. The chemical potential in the semiconductor can be tuned by electrostatic gates

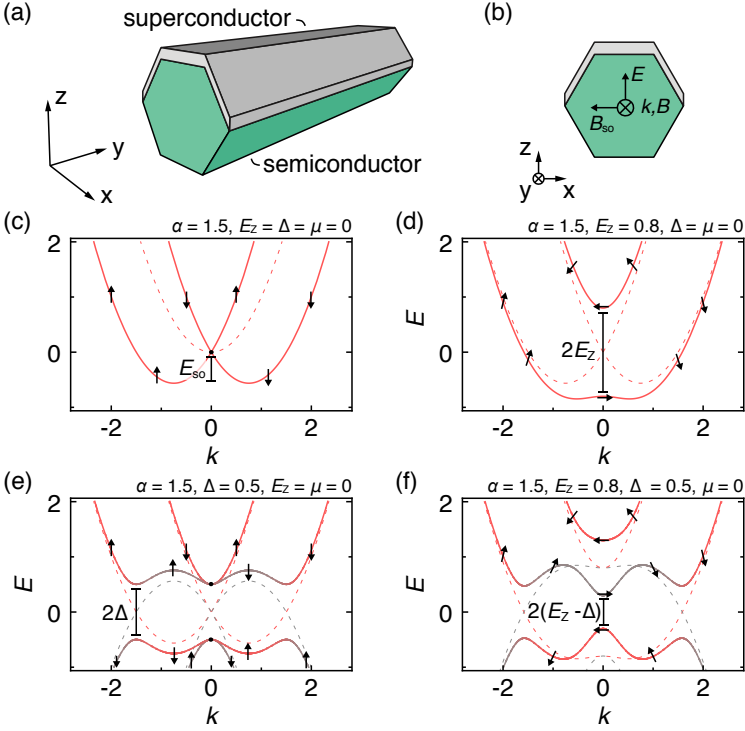


Fig. 2.1: (a) Schematic of a semiconducting (green) nanowire in proximity to a superconducting (gray) shell. (b) Orientation of particle momentum $\mathbf{k} = k \hat{y}$, electric field $\mathbf{E} = E \hat{z}$, spin-orbit field $\mathbf{B}_{so} = -B_{so} \hat{x}$ and external magnetic field $\mathbf{B} = B \hat{y}$. Single particle dispersion relations given by Eq. (2.2) (with $\mu = 0$, $m/\hbar^2 = 2$ and the spin orientation given by Eq. (2.2)). (c) For $B = 0$, the normal-state particle spectrum (dashed) is spin-split due to the spin-orbit coupling along k , depending on the particle spin orientation. The excitation energy is lowered by $E_{so} = m\alpha^2/2$. (d) Applying axial B hybridizes the spins and opens a Zeeman gap, E_z , at $k = 0$. (e) Inducing the superconductivity at $B = 0$ couples the spin-split particle and hole excitation bands (dashed), opening the superconducting gap Δ . (f) For a finite $\Delta < E_z$ the system is in the topological regime, with the zero-momentum gap given by $2(E_z - \Delta)$.

placed in the vicinity (capacitive coupling) of the wire. Consider, for now, the case with $\mu = 0$.

Introducing spin-orbit coupling to the system boosts the momenta of the particles depending on their spin orientation. The dispersion relation consists of two parabola shifted with respect to zero momentum by $k_{\text{so}} = \pm m\alpha$ and reduced in energy by $E_{\text{so}} = m\alpha^2/2$ [Fig. 2.1(c)]. Note that spin-orbit coupling does not break time-reversal symmetry; consequently, the two different spin species are present for all the eigenenergies.

Applying an axial magnetic field hybridizes the spins around zero momentum, opening a gap equal to $2E_Z$ [Fig. 2.1(d)]. In addition, the combination of spin-orbit and Zeeman fields gives rise to a non-trivial spin texture in momentum space. Within the Zeeman gap, only the lowest energy band is occupied; the spin components along \mathbf{B} (and \mathbf{k}) of the left- and right-moving particles are parallel—the system is effectively spinless.

It is interesting to note that any magnetic field applied perpendicular to the spin-orbit field lifts the degeneracy at $k = 0$; in practice, however, the superconducting shell has the highest superconducting critical field along the wire. Furthermore, the Zeeman field parallel to the spin-orbit field does not couple opposite spins and the effectively spinless condition cannot be achieved.

Inducing superconductivity at zero magnetic field couples the spin-split particles and holes and opens a superconducting gap in the quasi-particle excitation spectrum [Fig. 2.1(e)], similar to the spin-degenerate case discussed in Section 1.3. The spin degeneracy is preserved in this case—the wire remains in a topologically trivial regime.

With a finite order parameter, the Zeeman field hybridizes and splits the opposite-spin bands, which again produces a non-trivial spin texture [Fig. 2.1(f)]. In this case, the induced superconductivity is a mixture of s-wave and p-wave components [47]. For $E_Z > \Delta$ the system is in a topological regime.

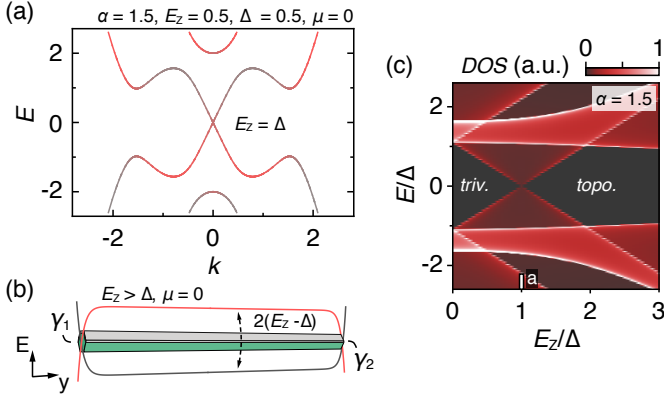


Fig. 2.2: (a) Dispersion relation of a hybrid nanowire computed using Eq. (2.2) evaluated at the critical Zeeman field given by Eq. (2.4). The other parameters are the same as in Fig. 2.1(f). (b) Schematic representation of a hybrid nanowire in a topological regime ($E_Z > \Delta$, $\mu = 0$) with two Majorana modes (γ_1 and γ_2) localized at the wire ends. (c) Qualitative simulations of the density of states (DOS) in the bulk of a hybrid nanowire as a function of the quasi-particle energy, E , and Zeeman energy, E_Z . The data in (a) and (c) were computed using $\hbar^2/m = 2$.

2.2.2 Topological Phase Transition

Realistically the particle-hole pairing amplitude, as well as the spin-orbit interaction strength, are (predominantly) fixed by the choice of the semiconductor and superconductor materials; therefore the external magnetic field is the parameter that drives the topological quantum phase transition by closing and reopening the gap at zero momentum. The gap at $k = 0$ with respect to the chemical potential can be deduced from Eq. (2.2) as

$$E_{G0} = \left| E_Z - \sqrt{\Delta^2 + \mu^2} \right| \quad (2.3)$$

For $B \sim 0$, the wire is in a trivial regime. As the Zeeman field is applied, E_{G0} decreases linearly and closes at the critical value

$$E_{Z,C} = \sqrt{\Delta^2 + \mu^2} \quad (2.4)$$

which is the onset of the topological phase [Fig. 2.2(a)]. The gap re-opens for an even higher Zeeman field, pushing the system into the topological regime with an effectively inverted superconducting gap.

For a finite length nanowire, both Δ and μ change abruptly at its ends. This results in a spatial transition from a topological to a trivial phase, with the Majorana zero modes bound to the end of the wire [Fig. 2.2(b) and Ref. [45]]. This results in a zero-energy peak in the density of states, which can be detected experimentally by measuring tunneling conductance at the end of the nanowire (see Section 1.9). For simplicity, this chapter considers only the bulk properties of the wire.

A heuristic representation of a continuous trivial-topological phase transition can be constructed by evaluating Eq. (2.2) at different k values with a constant step size, and then counting the number of states within a small, constant energy interval, which gives a qualitative measure of the density of states in the bulk of the wire. An example diagram of the computed density of states (DOS) as a function of the quasi-particle energy, E , and E_Z is shown in Fig. 2.2(c).

2.2.3 Spin-Orbit Coupling

Without the spin-orbit interaction, the Zeeman field closes the trivial gap, after which the system remains gapless due to the presence of finite momentum excitations at $E = 0$. The effect of the spin-orbit coupling strength on the trivial-topological phase transition is illustrated in Fig. 2.3 for two different values of α . The features of the main-gap closing and reopening—corresponding to the near-zero momentum excitations—are qualitatively the same for

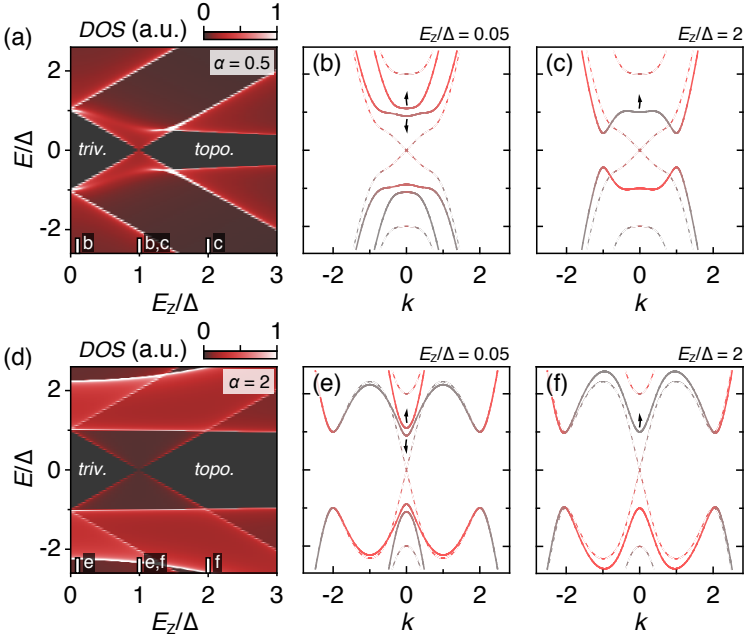


Fig. 2.3: (a) Qualitative simulations of the density of states (DOS) in the bulk of a hybrid nanowire as a function of the quasi-particle energy, E , and Zeeman energy, E_Z . The data was computed using Eq. (2.2) with $\alpha = 0.5$, $\mu = 0$, $\hbar^2/m = 2$ and $\Delta = 0.5$, and applying the heuristic technique described in the text. (b) The dispersion relation that was used to compute the data in (a) at $E_Z/\Delta = 0.05$ (trivial regime). (c) Same as (b) but evaluated at $E_Z/\Delta = 2$ (topological regime). The dashed lines in (b) and (c) correspond to the dispersion relation at $E_Z/\Delta = 1$. The arrows indicate the motion of the bands with E_Z . (d)–(f) Same as (a)–(c) but computed with $\alpha = 2$.

both values of α . In contrast, the appearance of the higher-energy states—arising from the finite momentum excitations—changes considerably with α . If the spin-orbit coupling is weak, the topological gap is small, because the splitting of states is dominated by \mathbf{B} . For a

strong spin-orbit coupling the excitations at higher momenta experience larger \mathbf{B}_{so} ; as a result, they depend less on the external magnetic field and the topological gap is nearly equal to the initial gap, Δ .

2.2.4 Chemical Potential and Orbital Effects

So far, the chemical potential was kept at zero, however, at a sufficiently large E_Z , the topological phase transition can also be driven by varying μ . As Eq. (2.4) suggests, the value of E_Z at which the onset of the topological phase is observed increases as μ deviates from zero. This can be verified numerically by computing the density of states at a given E_Z using the aforescribed heuristic technique to extract the minimal superconducting gap, E_G . Figure 2.4(a) displays E_G multiplied by the topological index $Q = \text{sign}(\sqrt{\mu^2 + \Delta^2} - E_Z)$ as a function of μ and E_Z . $Q = 1$ for trivial and $Q = -1$ for topological gap. While the critical field $E_{Z,C}$ [dashed line in Fig. 2.4(a)] is symmetric around $\mu = 0$ the finite-energy spectra differ notably [compare Fig. 2.4(b) and 2.4(c)].

Taking the orbital effects into account amplifies the contrast between the positive and negative μ . Experimental wires are not strictly one-dimensional; instead, they have a finite diameter. Charged particles moving in an external field experience Lorentz force. As a result, the particles can have a finite angular momentum, that modifies their energy eigenvalues [48]. Roughly speaking, the orbital contribution to the particle kinetic energy can be considered as an effective shift of the chemical potential proportional to the squared magnetic flux threading the wire cross-section [49]. Expressed in terms of E_Z the chemical potential modifies as

$$\mu \rightarrow \mu - \beta E_Z^2 \quad (2.5)$$

where β is a parameter proportional to the squared cross-sectional wire area, that characterizes the strength of the orbital effects. Substituting Eq. (2.5) into Eq. (2.2) yields two solutions for the critical

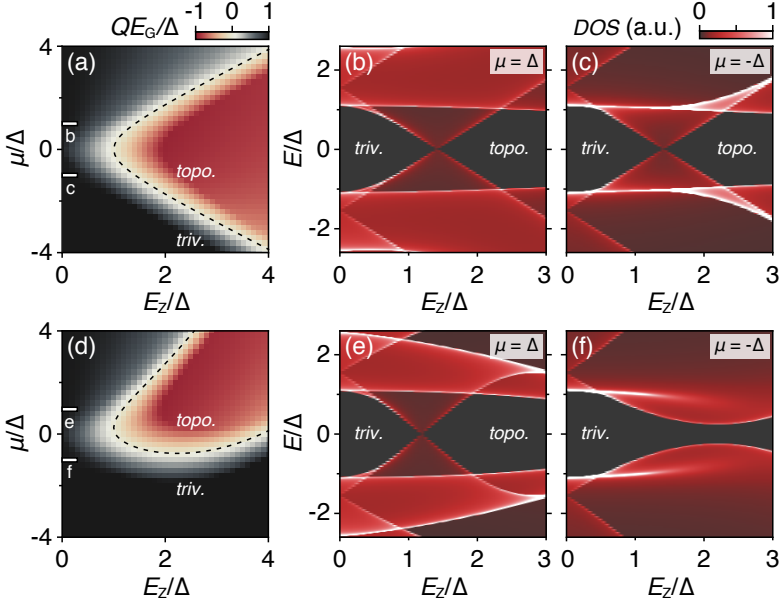


Fig. 2.4: (a) Calculated minimal-energy gap, E_G , multiplied by the topological index, $Q = \text{sign}(\sqrt{\mu^2 + \Delta^2} - E_Z)$, as a function of chemical potential, μ , and Zeeman energy, E_Z showing a topological phase diagram, symmetric around $\mu = 0$. The dashed curve is Eq. (2.4). $Q = 1$ for trivial and $Q = -1$ for topological gap. The data was computed using Eq. (2.2) with $\alpha = 0.5$, $\mu = 0$, $\hbar^2/m = 2$ and $\Delta = 0.5$, and applying the heuristic technique described in the text. (b) Qualitative simulations of the density of states (DOS) in the bulk of a hybrid nanowire, that was used to compute the data in (a) at $\mu = \Delta$. (c) Same as (b) but evaluated at $\mu = -\Delta$. (d)–(f) Same as (a)–(c) but computed by taking the orbital effects into account using Eq. (2.5) with $\beta = 0.5$.

Zeeman field, where the topological phase takes place

$$E_{Z,C}^2 = \frac{1 + 2\mu\beta \pm \sqrt{1 + 4\mu\beta - 4\Delta^2\beta^2}}{2\beta^2} \quad (2.6)$$

suggesting that the topological phase transition occurs twice as a function of E_Z . The modified phase diagrams are illustrated in Figs. 2.4(d)–2.4(f). The chemical potential effectively decreases as the Zeeman field grows. At the same time, the size of the topological regime (in E_Z) shrinks. For a sufficiently negative μ , the system is in a trivial regime for all E_Z [Fig. 2.4(f)].

2.2.5 Full-Shell Nanowires

Inspired by the data presented in Chapter 4, a theoretical study was put forward, demonstrating that semiconducting wires fully coated with a superconducting shell [Fig. 2.5(a)] can also host Majorana excitations [50]. The study shows that for a certain range of parameters, the quantized phase windings, n , in the superconducting full-shell (see Section 1.6) can lead to a topological phase, similar to the one in the conventional half-shell wires [44, 45] introduced in Subsection 2.2.1. The topological phase transition in the full-shell nanowires is driven by flux and not the Zeeman field like in the wires with partial shell coverage.

Because of the shell symmetry, the electric field, E , at the superconductor-semiconductor interface is pointing along the radial direction [Fig. 2.5(b)]. The resulting Rashba spin-orbit field, \mathbf{B}_{so} , at the boundary is along the azimuthal direction. An inherent rotational symmetry together with the single valuedness of the superconducting wave function restricts the total angular momentum quantum number, m_l , to half-integers if n is even or integers if n is odd.

With this in mind, consider the semiconductor-superconductor interface at a radius R . The effective Hamiltonian of a cylindrical

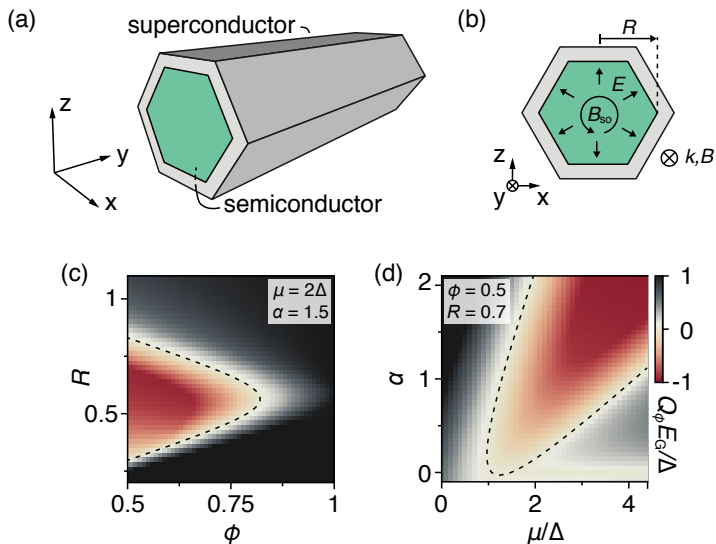


Fig. 2.5: (a) Schematic of a semiconducting (green) nanowire coated with a superconducting (gray) full-shell. (b) Orientation of particle momentum $\mathbf{k} = k \hat{y}$, electric field $\mathbf{E} = E \hat{r}$, spin-orbit field $\mathbf{B}_{so} = -B_{so} \hat{\phi}$ and external magnetic field $\mathbf{B} = B \hat{y}$. The wire radius R is indicated by an arrow. (c) Calculated minimal-energy gap, E_G , multiplied by the topological index, $Q_\phi = \text{sign}(\sqrt{\mu_{m_j}^2 + \Delta^2} - E_{Z,\phi})$, as a function of axial flux threading the wire $\phi = \Phi/\Phi_0$ and R , showing sizable topological phase. The dashed line indicates $E_G = 0$. The data were computed using Eq. (2.7) with $\alpha = 1.5$, $\mu = 2$, $\hbar^2/m = 2$ and $\Delta = 0.5$, and applying the heuristic technique described in the text. (d) Same as (c) but as a function of chemical potential, μ , and spin-orbit coupling, α , computed with $\phi = 0.5$ and $R = 0.7$.

full-shell wire can be cast into [50]

$$H = \left(\frac{\hbar^2 k^2}{2m} - \mu_{m_J} \right) \tau_z + \alpha k \sigma_x \tau_z + E_{Z,\phi} \sigma_y + \Delta \tau_x \quad (2.7)$$

$$+ A_{m_J} + C_{m_J} \sigma_y \tau_z$$

with the effective chemical potential, μ_{m_J} , and effective Zeeman energy, $E_{Z,\phi}$, as well as the couplings of the angular momentum to the magnetic field, A_{m_J} , and to the particle spin, C_{m_J} , given by

$$\mu_{m_J} = \mu - \frac{\hbar^2}{8mR^2} \left[4m_J^2 + 1 + (n - \phi)^2 \right] - \frac{\alpha}{2R} \quad (2.8a)$$

$$E_{Z,\phi} = \left[\frac{\hbar^2}{4mR^2} + \frac{\alpha}{2R} \right] (n - \phi) \quad (2.8b)$$

$$A_{m_J} = -m_J \frac{\hbar^2}{2mR^2} (n - \phi) \quad (2.8c)$$

$$C_{m_J} = -m_J \left[\frac{\hbar^2}{2mR^2} + \frac{\alpha}{R} \right] \quad (2.8d)$$

where $\phi = \Phi/\Phi_0$. Due to the particle-hole symmetry, the states with the opposite m_J are symmetric around zero energy, indicating that $m_J = 0$ is a special case.

For simplicity, take only the $n = 1$ and $m_J = 0$ state, in which case $A_{m_J} = C_{m_J} = 0$ and Eq. (2.7) can be mapped onto Eq. (2.1). The corresponding ϕ - R and μ - α phase diagrams exhibit a sizable topological phase [Fig. 2.5(c) and 2.5(d)]. The results imply that the hybrid full-shell wires can support MZMs.

The arguments above were made considering only the semiconductor-superconductor interface and $m_J = 0$ states. Taking the whole wire as well as the other m_J states into account might alter the shape of the topological phase, but in principle, it should remain finite [50].

3

EFFECTIVE g FACTOR IN MAJORANA WIRES

In this chapter, we use the effective g factor of Andreev subgap states in an axial magnetic field to investigate how the superconducting density of states is distributed between the semiconductor core and the superconducting shell in hybrid nanowires. We find a steplike reduction of the Andreev g factor and improved hard gap with reduced carrier density in the nanowire, controlled by gate voltage. These observations are relevant for Majorana devices, which require tunable carrier density and a g factor exceeding that of the parent superconductor. Additionally, we observe the closing and reopening of a gap in the subgap spectrum coincident with the appearance of a zero-bias conductance peak.

3.1 g FACTOR IN INAs

The electronic properties of a semiconductor nanowire can be altered dramatically by contacting it to a superconductor. If the nanowire has strong spin-orbit coupling, the application of a

This chapter is adapted from Ref. [51]. The experiment was conducted in collaboration with Mingtang Deng under the supervision of Charles Marcus. The nanowire materials were developed by Jesper Nygård and Peter Krogstrup.

magnetic field can induce a transition from trivial to topological superconductivity, with Majorana zero modes localized at the ends of the nanowire (Chapter 2 and Refs. [44, 45]). The Majorana bound states (MBSs) are predicted to exhibit non-abelian statistics, and can serve as a basis for topological quantum computing [25, 38, 52, 53]. Following concrete theoretical proposals to generate MBSs in these systems, several experiments have reported zero-bias conductance peaks [54–56] consistent with theoretical expectation in a number of ways. More recently, the development of epitaxial hybrid nanowires [57] has improved the superconducting gap [58], making evident the coalescence of Andreev bound states (ABSs) to form the zero-bias conductance peak [59, 60].

The rate of linear decrease of the subgap ABSs towards zero energy as a function of magnetic field defines an effective g factor, denoted g^* . Inducing the topological phase using an applied field requires g^* to exceed the g factor of the proximitizing s-wave superconductor, otherwise the field will drive the whole system normal. Studies on hybrid InAs/Al nanowires found $|g^*|$ ranging from 4 to 50 [55, 59, 61], substantially different from the bulk value, $g_{\text{InAs}} \sim -15$ [62, 63]. Gate dependence measurements of g^* have been reported in an InAs/InP core/shell quantum dot coupled to a superconductor [64], where repulsion effect from superconducting continuum suppressed g^* of the spin-down branch, while g^* of the spin-up branch remained around -6 . The effective g factor of a quantum dot electronic states has also been studied in non-proximitized, bare InAs nanowires. A g factor fluctuating between -2 and -18 has been observed in a single-dot geometry [65]. Electric and magnetic field tunable g factor has been demonstrated in a double-dot geometry [66]. Some suppression of g^* can be attributed to spatial confinement [67, 68] as shown experimentally in Ref. [69], while enhancement of g^* can result from a combination of Zeeman and orbital contributions in higher subbands [70].

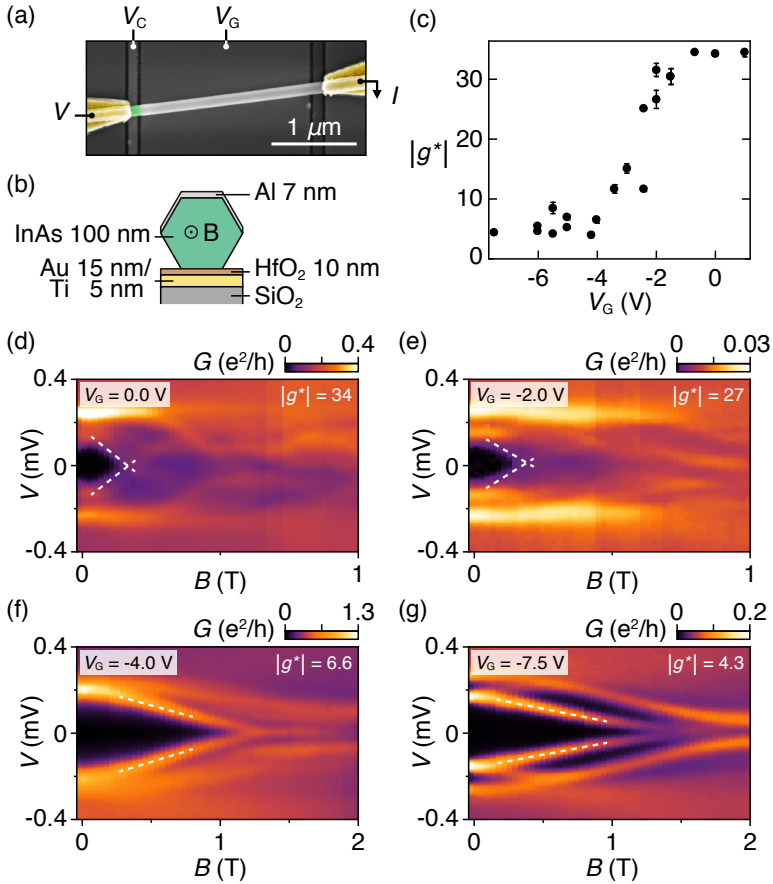


Fig. 3.1: (a) False-color electron micrograph of device g1, showing InAs nanowire (green), three-facet Al shell (light gray), Ti/Au contacts (yellow) and bottom-gates (dark gray). (b) Schematic device cross section, showing orientation of applied magnetic field, B , and Al shell relative to the bottom-gate. (c) Magnitude of effective g factor, $|g^*|$, of the lowest subgap state showing a steplike dependence on bottom-gate voltage, V_G . Error bars are root-mean-square difference between upper (electron) and lower (hole) branches. (d) Differential conductance, G , as a function of source-drain bias, V , at gate voltage $V_G = 0.0$ V. Dashed lines correspond to $|g^*| = 34$. (e)–(g) Similar to (d) but taken at gate voltage (e) $V_G = -2.0$ V, (f) $V_G = -4.0$ V and (g) $V_G = -7.5$ V, giving (e) $|g^*| = 27$, (f) $|g^*| = 6.6$ and (g) $|g^*| = 4.3$.

Here, we show that the effective g factor of ABSs depends sensitively on the carrier density in the wire, controlled by electrostatic gate voltages. We interpret this observation as revealing how the superconducting density of states is distributed throughout the cross section of the hybrid system. The semiconducting InAs nanowire has large spin-orbit coupling and large negative g factor, whereas the superconducting Al shell, which induces the proximity effect, has small spin-orbit coupling, and $g_{\text{Al}} \sim 2$. At high carrier density in the wire, subgap states predominantly reside in the nanowire, reflecting the properties of the semiconductor; as carriers in the nanowire are depleted, the remaining portion of the states are confined against the InAs/Al interface, with relatively small g^* and strong proximity effect.

3.2 HALF-SHELL DEVICES

Five devices, denoted g1 to g5, were investigated. All were $\sim 2 \mu\text{m}$ long, made from MBE-grown [0001] wurtzite InAs nanowires with hexagonal cross-section [57]. Two devices (g2 and g3) had epitaxial Al on two facets, the rest (g1, g4 and g5) had epitaxial Al on three facets [Figs. 3.1(b), 3.2(b) and Table 2]. To form a tunnel probe, the Al shell was removed by wet-etching at one end, leaving a $\sim 100 \text{ nm}$ segment of bare InAs next to one of the normal-metal leads. The tunneling rate was controlled with the

Device	g1	g2	g3	g4	g5
Batch	418	173	578	418	418
Al facets	3	2	2	3	3

Table 2: Measured device number, corresponding nanowire growth batch number and number of Al facets covering the hexagonal InAs core.

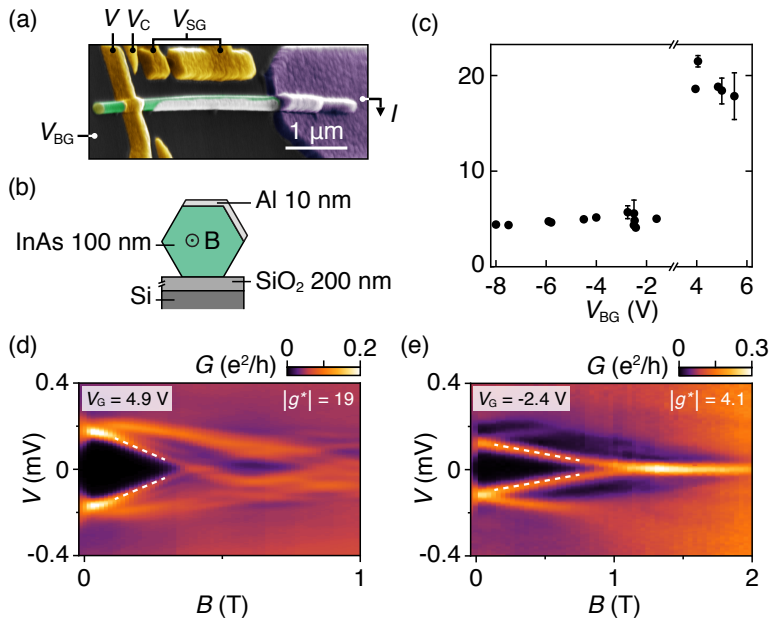


Fig. 3.2: (a) False-color electron micrograph of device g2, consisting of InAs nanowire (green) with two-facet Al shell (blue), Ti/Au contact and side-gates (yellow), and Ti/Al/V contact (purple). (b) Schematic device cross section showing direction of applied magnetic field, B , and orientation of Al shell relative to the back-gate. (c) Effective g factor, $|g^*|$, as a function of applied back-gate voltage, V_{BG} . (d) Subgap state evolution in B , measured at $V_{BG} = 4.9$ V. The white, dashed lines correspond to $|g^*| = 19$. (e) Same as (d) taken at back-gate voltage $V_{BG} = -2.4$ V, giving $|g^*| = 4.1$.

cutter-gate voltage, V_C . The nanowire density in devices g1 and g4 was controlled with bottom-gates at voltage V_G [Figs. 3.1(a)]. Device g2 used a conducting substrate at voltage V_{BG} [Fig. 3.2(a)]. Device g3 used top-gates at voltage V_{TG} [Fig. 3.3(a)]. Device g5 used only side-gates at voltage V_{SG} . For all devices, gates were positioned on the side of the nanowire opposite to the Al shell. The magnetic field was oriented along the nanowire axis using a three-axis vector magnet. Standard ac lock-in techniques were used in a dilution refrigerator with a base temperature of ~ 20 mK. For a more detailed description of the wire growth, device fabrication and measurements see Appendix A.

3.3 STEPLIKE DECREASE

The Zeeman splitting of ABSs can be extracted from the differential conductance, $G = dI/dV$, measured as a function of applied source-drain bias, V , and magnetic field, B , along the wire. To avoid the gate-dependent level repulsion effect [64], the absolute value of the effective g factor, $|g^*|$, was measured using the lowest-energy subgap state as it moved toward zero energy with B . Figure 3.1(c) shows $|g^*|$ of the lowest energy state as a function of bottom-gate voltage V_G for device g1, displaying a characteristic steplike behavior as a function of gate voltage. A B -sweep at $V_G = 0.0$ V displays a quasi-continuous band of ABSs with $|g^*| = 34$, as shown in Fig. 3.1(d). The hard superconducting gap collapses at roughly $B = 0.2$ T, leaving a soft gap behind. At higher fields, the evolution of levels cannot be easily tracked. The main large gap at $V = 240$ μ eV—presumably arising from superconductivity among electrons that predominantly reside in the Al shell—remains visible throughout the measured range. When V_G is changed from -2 V to -4 V, $|g^*|$ abruptly decreases from 27 to 6.6 [Figs. 3.1(e) and 3.1(f)]. The effective g factor saturates at $|g^*| \sim 5$ for more negative values of V_G . In contrast to the behavior at $V_G \sim 0$ V where the continuum of states moved toward zero

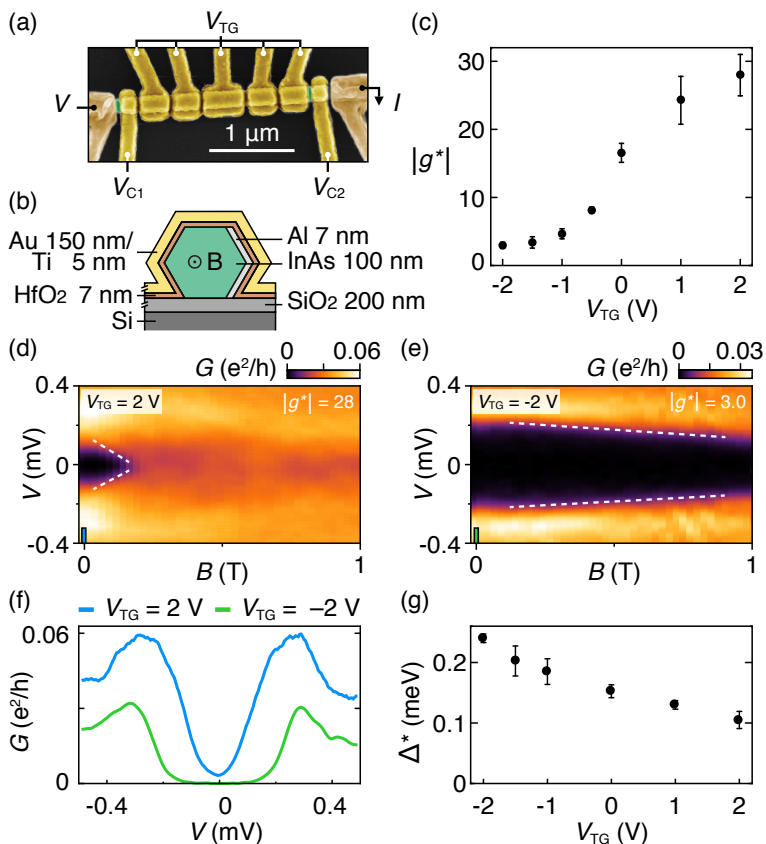


Fig. 3.3: (a) Colorized micrograph of device g3, showing InAs nanowire (green), Ti/Au contacts and top gates (yellow). (b) Schematic cross section of device g3. (c) Effective g factor, $|g^*|$, showing a steplike dependence on the top-gate voltage, V_{TG} . (d) Differential conductance, G , as a function of source-drain bias, V , and magnetic field B at $V_{TG} = 2$ V. Dashed lines correspond to $|g^*| = 28$. (e) Similar to (d) but taken at $V_{TG} = -2$ V, giving $|g^*| = 3.0$. (f) Line-cuts taken from (d) (blue) and (e) (green) at $B = 0$. (g) Effective induced superconducting gap, Δ^* , as a function of V_{TG} , defined as the maximum slope of G . Error bars in (c) and (g) are root-mean-square difference between upper (electron) and lower (hole) branches. The tunneling G was measured with negative voltage on V_{C1} and fixed $V_{C2} = 1$ V, such that the other end is open to the drain.

energy, evolution of single, discrete ABS can be clearly followed at $V_G = -7.5$ V [Fig. 3.1(e)]. In this case, the ABS with $|g^*| = 4.3$ reaches zero energy at $B = 1.5$ T, with hard gaps on both sides of the state throughout the sweep.

Qualitatively similar behavior was seen in multiple devices. For device g2 at back-gate voltages in the range of 4 V to 6 V, $|g^*|$ was ~ 20 [Fig. 3.2(c)]. A B -sweep taken at $V_{BG} = 4.9$ V shows a quasi-continuous band of subgap-states with $|g^*| = 19$ crossing zero-bias at $B = 0.4$ T, to become a quasi-continuum throughout the subgap region at higher field. For V_{BG} in the range -2 V to -8 V, $|g^*|$ remained roughly constant at ~ 5 . At $V_{BG} = -2.4$ V, a single sharp ABS was observed, with $|g^*| = 4.1$ coalescing at $B = 1$ T and sticking to zero energy for higher fields. The narrow zero-bias conductance peak remained insensitive to magnetic field from 1 to 2 T. Data from the top-gated device g3 showing a similar steplike decrease in $|g^*|$ as well as gate-voltage dependence of the effective induced superconducting gap, Δ^* is summarized in Fig. 3.3.

We propose two contributing factors to the steplike evolution of $|g^*|$ as carriers are depleted by the gate voltage. The first is the reduction of the orbital contribution to $|g^*|$ as the wire is depleted across most of its cross section [67, 68, 70]. The second is that the remaining density in the nanowire is predominately against the interface with the Al shell, strongly coupled to the superconductor [71–73].

3.4 GAP CLOSING & REOPENING

A clearer view of excited states above the lowest energy ABS, including the closing and reopening of a gap coincident with the appearance of a zero-bias conductance peak, can be seen for device g4 in Fig. 3.4. Due to the gate dependent g factor, it is natural to describe the robustness of the zero-bias state in the energy scale corresponding to Zeeman splitting. A B -sweep at $V_G = -5.0$ V reveals a quasi-

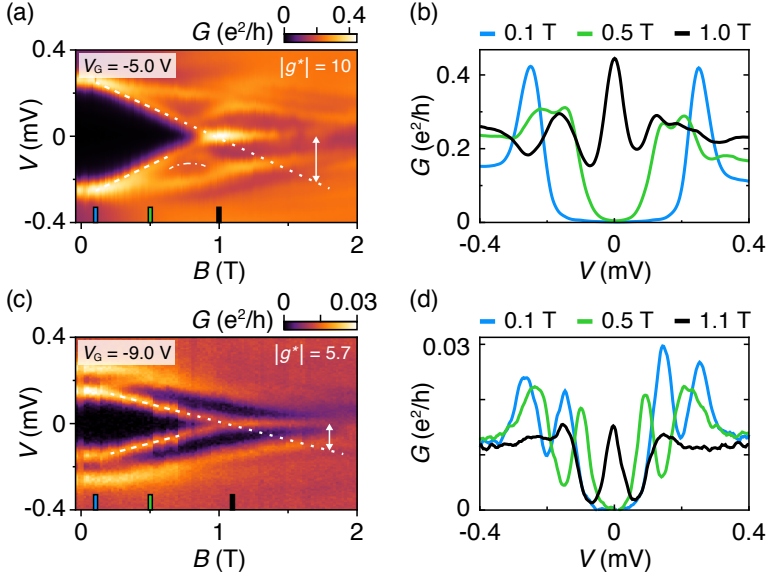


Fig. 3.4: (a) Conductance as a function of V and B from device g_4 taken at $V_G = -5.0$ V. A quasi-continuous band of ABSs have $|g^*| = 10$. The gap closing-reopening feature around $B = 0.9$ T coincides with the formation of zero-bias peak persisting up to $B \sim 1.7$ T. The white arrow indicates Zeeman splitting of ~ 225 μ eV. (b) Line-cuts taken from (a) display a hard superconducting gap evolving into a zero-bias peak in high field at a subgap-state-rich regime. (c) Similar to (a) but taken at $V_G = -9.0$ V. A discrete ABS with $|g^*| = 5.7$ coalesce at zero-energy around $B = 1.0$ T. The white arrow at $B = 1.8$ T corresponds to Zeeman splitting of ~ 125 μ eV. (d) Line-cuts taken from (c) show the emergence of a symmetric zero-bias peak with low base-conductance.

continuous band of ABSs with a $|g^*| = 10$ [Figs. 3.4(a) and 3.4(b)]. At low field, the gap is hard on the low-energy side of the ABS edge, yielding small values of G ; at higher fields, G is nonzero throughout the subgap region. Around $B = 0.9$ T an excited subgap-state [indicated by the dot-dashed line in Fig. 3.4(a)] becomes visible. It increases in energy and merges with the higher-energy ABSs around $B = 1.1$ T. The lowest energy state evolves into a zero-bias peak at roughly $B = 1.0$ T. The zero-mode can be followed up to ~ 1.7 T, whereafter it merges with the high subgap density. Extrapolating the $|g^*|$ slope of the lowest energy state [see the dashed line in Fig. 3.4(a)] infers that the zero-bias peak extends for ~ 225 μeV —comparable to the size of the main large gap.

Lowering the gate voltage changes the picture qualitatively. The tunneling spectrum dependence on magnetic field, taken at $V_G = -9.0$ V displays a discrete, low-energy ABS with $|g^*| = 5.7$ [Fig. 3.4(c)]. The ABS merge at $B = 1.0$ T to form a well-defined zero-bias peak, clearly visible up to $B = 1.8$ T, corresponding to Zeeman splitting of ~ 125 μeV . The feature of gap closing-reopening is absent in this case. The subgap conductance is low throughout the sweep [Fig. 3.4(d)], suggesting a low-density ABS regime.

The tunneling spectrum for device g5 further illustrates the reopening of the gap (Fig. 3.5). Evolution of the subgap states can be followed rather clearly: a quasi-continuous band of ABSs with $|g^*| = 10$ emerges from above the gap at $B = 0.3$ T; Around $B = 1.0$ T an excited subgap-state (indicated by the dot-dashed line) starts to gain energy with increasing field; The lowest energy state forms a zero-bias state that ranges from $B = 1.1$ T to 1.7 T, corresponding to Zeeman splitting of ~ 175 μeV (white arrow).

The evolution of V spectra with B in Figs. 3.4(a) and 3.5(a) show a gap to the lowest excited state that nearly closes then reopens at almost the same value of B where the zero-bias peak appears. This can be interpreted as a characteristic feature of a topological phase transition [74–76]. The residual gap at the phase transition in both

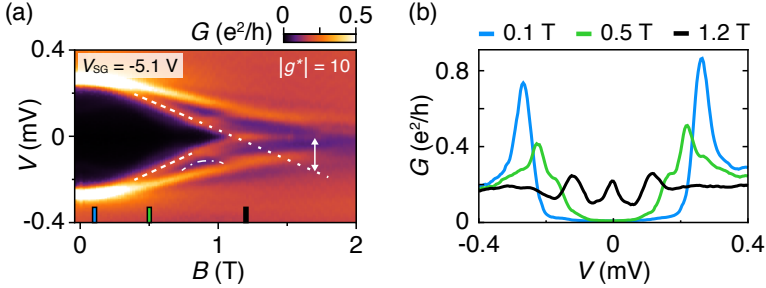


Fig. 3.5: (a) Conductance as a function of V and B for device g_5 at $V_{SG} = -5.1$ V shows subgap-states with $|g^*| = 10$ coalescing at $B \sim 1.1$ T, while an excited state increases in energy. (b) Line-cuts taken from (a) illustrate the formation of zero-bias peak at high field. A pair of low-conductance excited states resembling gap closing-reopening are visible around $B = 1.0$ T.

devices is finite, but less than half the energy of the main large gap—consistent with the length quantization of the wire [77]. It has been argued theoretically [78,79] and observed experimentally [64,80] that a zero-bias conductance anomaly can be rendered by (partially) localized ABSs/ strongly interacting MBSs. However, numerical simulations indicate, that a topological phase transition is composed of both emergent zero-bias peak and gap closing-reopening feature [78,79]. At more negative gate voltages, that is at lower electron density, the number of occupied subbands is expected to decrease. The corresponding magnetic field sweep in Fig. 3.4(c) shows a single ABS coalescing into a zero-bias peak, however, the gap closing-reopening feature is not visible in tunneling conductance. This is presumably due to the change in nanowire parameters, such as Rashba spin-orbit coupling, as the electric field generated by the gate voltage is increased [77,81].

3.5 CONCLUSION

In summary, we have measured the effective g factor of subgap states in InAs nanowires with epitaxial Al as a function of density of carriers in the wire, controlled by gate voltages, in a number of device geometries. In addition, robust zero-bias peaks—ranging for Zeeman energy comparable to the superconducting gap—have been observed at different charge carrier densities. We provide a qualitative interpretation of the data. The observations are reproduced with multiple devices. In order to understand the experimental findings in more detail, a refined electrostatic modeling considering both Zeeman and orbital contributions is desired.

4

MAJORANA MODES IN FULL-SHELL WIRES

This chapter demonstrates a novel means of creating Majorana zero modes using magnetic flux applied to a full superconducting shell surrounding a semiconducting nanowire core, unifying approaches based on proximitized nanowires and vortices in topological superconductors. In the destructive Little-Parks regime, reentrant regions of superconductivity are associated with integer number of phase windings in the shell. Tunneling into the core reveals a hard induced gap near zero applied flux, corresponding to zero phase winding, and a gapped region with a discrete zero-energy state for flux around $\Phi_0 = h/2e$, corresponding to 2π phase winding. Coulomb peak spacing in full-shell islands around one applied flux shows exponentially decreasing deviation from $1e$ periodicity with device length, consistent with the picture of Majorana modes located at the ends of the wire.

This chapter is adapted from Ref. [82], that reports experimental findings, which was later merged with the supporting theory [50] and published as Ref. [83]. The experiment was conducted under the supervision of Charles Marcus. Mingtang Deng assisted with the experiments and data analysis. The nanowires were grown by Peter Krogstrup.

4.1 WIRE-VORTEX ANALOGY

Majorana zero modes (MZMs) at the ends of one-dimensional topological superconductors are expected to exhibit non-trivial braiding statistics [24, 38], opening a path toward topologically protected quantum computing [25, 27]. Among the proposals to realize MZMs, one approach [44, 45] based on semiconductor nanowires with strong spin-orbit coupling subject to a Zeeman field and superconducting proximity effect has received particular attention, yielding numerous compelling experimental signatures [54, 59–61, 84]. An alternative route to MZMs aims to create vortices in spinless superconductors, by various means, for instance by coupling a vortex in a conventional superconductor to a topological insulator [42, 85], using doped topological insulators [86, 87], or using vortices in exotic quantum Hall analogs of spinless superconductors [88].

The conceptually new approach demonstrated in this chapter, based on superconducting phase winding in an Al shell surrounding an InAs nanowire core, contains elements of both the proximitized-wire scheme [44, 45] and vortex-based schemes [42] for creating MZMs. In the destructive Little-Parks regime [17, 89], the modulation of critical current and temperature with flux applied along the hybrid nanowire results in reentrant superconductivity [90, 91] where each region is associated with a quantized number of twists of the superconducting phase [10]. The result is a series of topologically locked boundary conditions for the proximity effect of the core, where the number of phase twists in the Al shell corresponds to the number of phase vortices in the nanowire core. Note that it is the fluxoid that is quantized, not the flux itself [10].

We observe that tunneling into the core in the zeroth superconducting lobe, around zero flux, yields a hard proximity-induced gap with no subgap features. In the superconducting regions around one quantum of applied flux, corresponding to phase twists of $\pm 2\pi$ in the shell, tunneling spectra into the core shows stable zero-bias peaks,

indicating a discrete subgap state fixed at zero energy, consistent with the Majorana picture.

Further evidence that MZMs reside at the ends of the wire is obtained by investigating Coulomb blockade conductance peaks in full-shell wire islands of various lengths. We find that in the zeroth lobe, Coulomb blockade conductance peaks show $2e$ spacing, indicating Cooper-pair tunneling and an induced gap exceeding the island charging energy. In the first lobe, peak spacings are roughly $1e$ -periodic, with slight even-odd alternation that vanishes exponentially with island length, suggesting overlapping Majorana modes at the two ends of the Coulomb island, as investigated previously [61, 92]. These experimental observations are consistent with the recent theory [50] showing that a radial Rashba field arising from the band bending at the semiconductor-superconductor interface [72, 73], along with an odd multiple of 2π phase twists in the boundary condition, can induce a topological state with MZMs. Further support for possible topological phase in full-shell nanowires is given in Ref. [93].

Phase winding in the full-shell geometry represents the continuum limit of discrete boundaries with differing phases. Phase control of Andreev bound states was investigated experimentally for two superconductors as a function of phase difference in Refs. [94–96]. In the context of topological states, Altland and Zirnbauer considered two superconducting boundaries with phase difference of π in their original study of symmetry classes of Andreev billiards [97]. Phase difference between superconducting boundaries was shown theoretically to influence the topological transition and the appearance of MZMs in long Josephson junctions [98, 99] as well as nanowire models [100–102]. Control of topological states by multiple phase differences was investigated in Refs. [103, 104]. A unique feature of the continuous superconducting shell is the rigidity of phase winding by fluxoid quantization [10]. In this case, a topologically constrained boundary condition locks the topological phase within.

4.2 FULL-SHELL DEVICES

InAs nanowires with wurtzite crystal structure (growth batch 439) were grown along the [0001] direction by the vapor-liquid-solid method using molecular beam epitaxy (MBE). The nanowires have a hexagonal cross section with maximum diameter $d = 130$ nm. A 30 nm epitaxial Al layer was grown while rotating the sample [57], yielding a fully enclosing shell [Fig. 4.1(a)]. Wires were placed on a doped Si substrate capped with thermal oxide. The Al shell was lithographically patterned and selectively etched. Ti/Au ohmic contacts were patterned and deposited following Ar-ion milling. For some devices, Ti/Au gate electrodes were patterned in a subsequent lithographic step [Fig. 4.5(a)]. Standard ac lock-in measurements were carried out in a dilution refrigerator with a base temperature of 20 mK. Magnetic field was applied parallel to the nanowire using three-axis vector magnet. Two device geometries, measured in three devices each, showed similar results. Data from two devices are presented: device f1 was used for 4-probe measurements of the shell [Fig. 4.1(b)] and tunneling spectroscopy of the core [Fig. 4.2(a)]; device f2 comprised six Coulomb islands of different lengths fabricated on a single nanowire, each with separate ohmic contacts, two side gates to trim tunnel barriers, and a plunger gate to change occupancy [Fig. 4.5(a)]. For a more detailed description of the wire growth, device fabrication and measurements see Appendix A.

Differential resistance of the shell, $R_s = dV_s/dI_s$, measured for device f1 as a function of bias current, I_s , and axial magnetic field, B , showed a lobe pattern characteristic of the destructive regime [Fig. 4.1(c)] with maximum switching current of $70 \mu\text{A}$ at $B = 0$, the center of the zeroth lobe. Between the zeroth and first lobes, supercurrent vanished at $|B| = 45$ mT, re-emerged at 70 mT, and had a maximum near the center of the first lobe, at $|B| = 110$ mT. A second lobe with smaller critical current was also observed, but no third lobe.

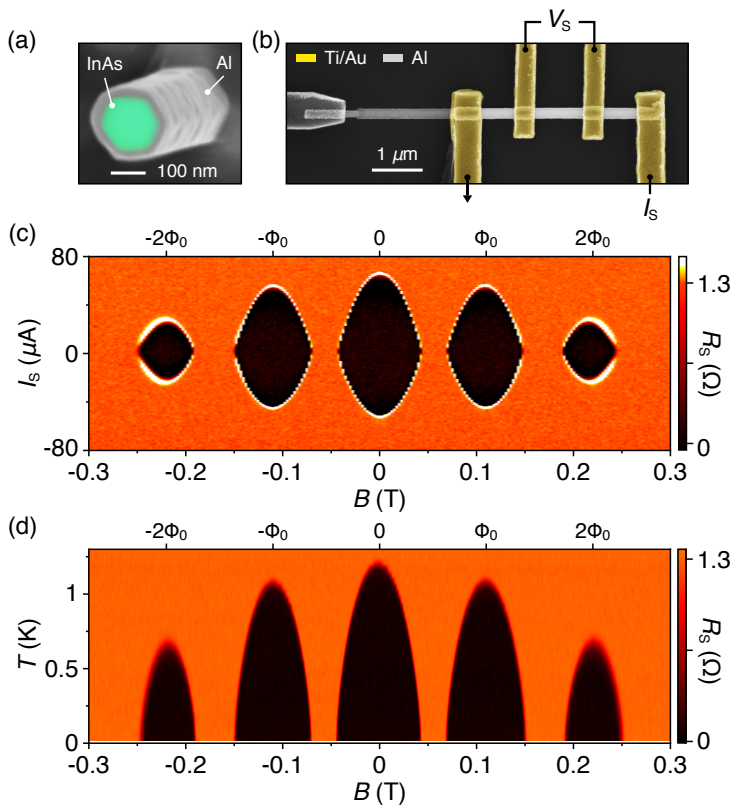


Fig. 4.1: (a) Colorized material-sensitive electron micrograph of InAs-Al hybrid nanowire. Hexagonal InAs core (maximum diameter 130 nm) with 30 nm full-shell epitaxial Al. (b) Micrograph of device f1, colorized to highlight 4-probe measurement setup. (c) Differential resistance of the Al shell, R_s , as a function of current bias, I_s , and axial magnetic field, B , measured at 20 mK. Top axis shows flux, BA_{wire} , in units of the flux quantum $\Phi_0 = h/2e$. Superconducting lobes are separated by destructive regions near odd half-integer flux quanta. (d) Temperature evolution of R_s as a function of B measured around $I_s = 0$. Note that R_s equals the normal-state resistance in all destructive regimes.

Temperature dependence of R_s around zero bias yielded a reentrant phase diagram with superconducting regions separated by destructive regions with temperature-independent normal-state resistance $R_s^{(N)} = 1.3 \Omega$ [Fig. 4.1(d)]. $R_s^{(N)}$ and shell dimensions from Fig. 4.1(a) yield a Drude mean free path of $l = 19 \text{ nm}$. The dirty-limit shell coherence length [10,105]

$$\xi_s = \sqrt{\frac{\pi \hbar v_F l}{24 k_B T_C}} \quad (4.1)$$

can then be found using the zero-field critical temperature $T_C = 1.2 \text{ K}$ from Fig. 4.1(d) and Fermi velocity of Al, $v_F = 2 \times 10^6 \text{ m/s}$ [106], with Planck constant \hbar and Boltzmann constant k_B , yielding $\xi_s = 180 \text{ nm}$. The same values for ξ_s is found using the onset of the first destructive regime [107].

4.3 TUNNELING SPECTROSCOPY

Differential conductance, $G = dI/dV$, as a function of source-drain voltage, V , measured in the tunneling regime as a probe of the local density of states at the end of the nanowire is shown in Figs. 4.2 and 4.3. The Al shell was removed at the end of the wire and the tunnel barrier was controlled by the global back-gate at voltage V_{BG} . At zero field, a hard superconducting gap was observed throughout the zeroth superconducting lobe [Figs. 4.2(b) and 4.2(c)]. Similar to the supercurrent measurements presented above, the superconducting gap in the core closed at $|B| = 45 \text{ mT}$ and reopened at 70 mT , separated by a gapless destructive regime. Upon reopening, a narrow zero-bias conductance peak was observed throughout the first gapped lobe [Figs. 4.2(b) and 4.2(d)]. Several flux-dependent subgap states are also visible, separated from the zero-bias peak in the first lobe. These nonzero subgap states are analogs of Caroli-de Gennes-Matricon bound states [108], in this case confined at the metal-semiconductor interface rather than around a vortex core.

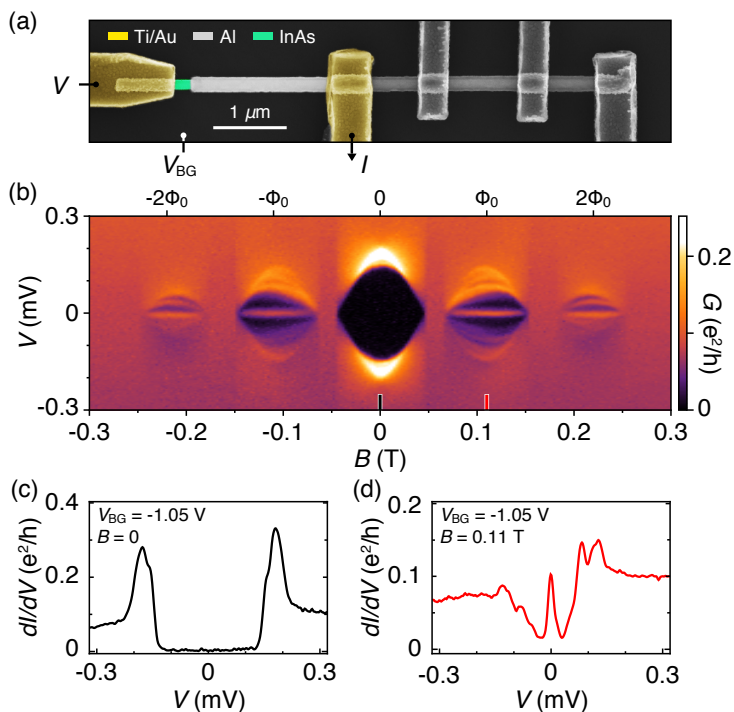


Fig. 4.2: (a) Micrograph of device f1 colored to highlight tunneling spectroscopy set-up. (b) Differential conductance, G , as a function of source-drain bias voltage, V , and axial field, B . The zeroth lobe shows a hard superconducting gap, the first lobes show zero-bias peak, the second lobes show non-zero subgap states. The lobes are separated by featureless normal-state spectra. (c) Line-cut of the conductance taken at $B = 0$ and $V_{BG} = -1.05$ V. (d) Same as (c) but measured in the first lobe at $B = 110$ mT

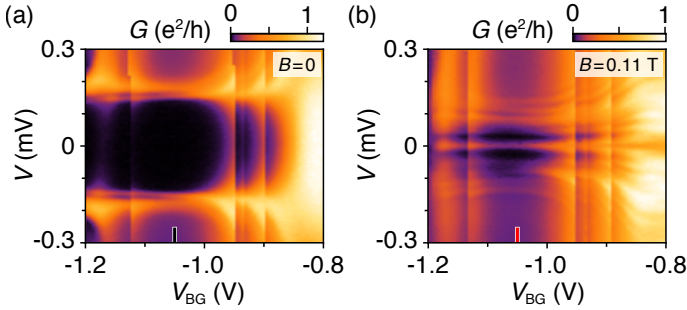


Fig. 4.3: (a) Zero-field conductance for device f1 as a function of source-drain bias voltage, V , and back-gate voltage, V_{BG} . (b) Same as (a) but measured in the first lobe at $B = 110$ mT. The ticks at $V_{\text{BG}} = -1.05$ V indicate the position of line-cuts shown in Fig. 4.2(c) and 4.2(d).

The first lobe persists to ± 150 mT, above which a second gapless destructive regime was observed. A second gapped lobe centered at $|B| \sim 220$ mT then appeared, containing several subgap states away from zero energy [4.4]. The second lobe closes at 250 mT, above which only normal-state behavior was observed.

The dependence of tunneling spectra on back-gate voltage in the zeroth lobe is shown in Fig. 4.3(a). In weak tunneling regime, for $V_{\text{BG}} < -1$ V a hard gap was observed, with $\Delta = 180 \mu\text{eV}$ [see the line-cut in Fig. 4.2(c)]. As the device is opened, for $V_{\text{BG}} \sim -0.8$ V subgap conductance is enhanced due to Andreev processes. The increase in conductance at $V_{\text{BG}} \sim -1.2$ V is likely due to a resonance in the barrier. In the first lobe, at $B = 110$ mT, the sweep of V_{BG} showed a zero-energy state throughout the tunneling regime [Fig. 4.3(b)]. The cut displayed in Fig. 4.2(d) shows a discrete zero-bias peak well separated from other states. As the tunnel barrier is opened, the zero-bias peak gradually evolves into a zero-bias dip at strong coupling, in qualitative agreement with theory supporting MZMs [109]. Several switches in data occurred at the same gate

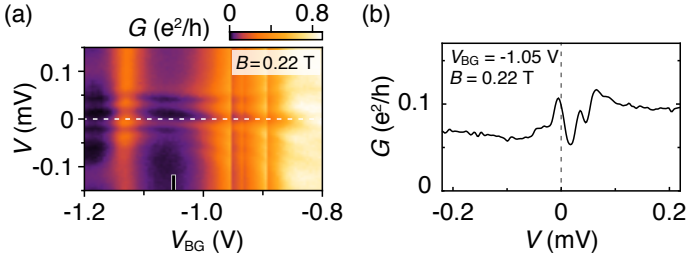


Fig. 4.4: (a) Differential conductance for device f1 as a function of source-drain voltage, V , and back-gate voltage, V_{BG} . (c) Line-cut of the conductance taken at $B = 220$ mT and $V_{BG} = -1.05$ V. The spectrum shows subgap states away from zero energy.

voltages in Figs. 4.3(a), 4.3(b) and 4.4(a), presumably due to gate-dependent charge motion in the barrier.

4.4 COULOMB SPECTROSCOPY

Hybridization of MZMs can be measured in Coulomb islands of finite length from the spacing of Coulomb blockade conductance peaks [61, 92, 110, 111]. In particular, the exponential length dependence of hybridization energy supports the Majorana interpretation and further indicates that the MZMs are located close to the ends of the wire, and not in the middle [78, 112]. We investigated full-shell islands over a range of device lengths from 210 nm to 970 nm, fabricated on a single nanowire, as shown in Fig. 4.5(a).

Zero-bias conductance as a function of plunger-gate voltage, V_G , and B for device f2 yielded series of Coulomb blockade peaks for each segment, examples of which are shown in Fig. 4.5(b). The corresponding average peak spacings, $\overline{\delta V}$, for even and odd Coulomb valleys as a function of B are shown in Fig. 4.5(c). Around zero field, Coulomb-blockade peaks with $2e$ periodicity were found. These peaks split at ~ 40 mT toward the high-field end of the zeroth

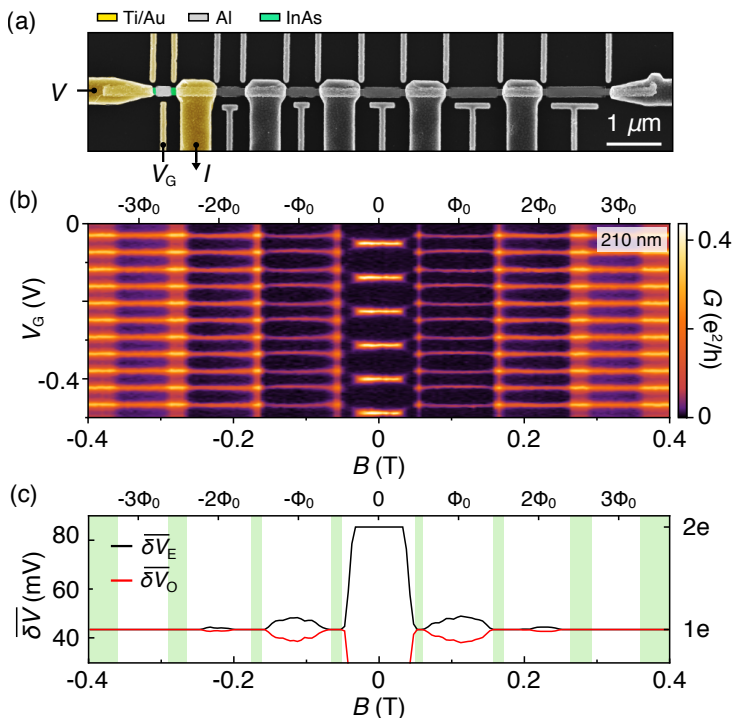


Fig. 4.5: (a) Micrograph of device f2 comprising six islands with individual gates and leads, spanning a range of lengths from 210 nm to 970 nm. The measurement setup for 210 nm segment is highlighted in colors. (b) Zero-bias conductance for the 210 nm segment showing Coulomb blockade evolution as a function of plunger gate voltage, V_G , and axial magnetic field, B . (c) Average peak spacings for even (black) and odd (red) Coulomb valleys, $\overline{\delta V}$, from the data in (a) as a function of B , with destructive regimes shown in green. Coulomb peaks spaced by $2e$ split in field and become $1e$ -periodic around 55 mT. At higher field, odd Coulomb valleys shrink, reaching a minimum around 120 mT. In the second destructive regime around 165 mT peaks are $1e$ -periodic again.

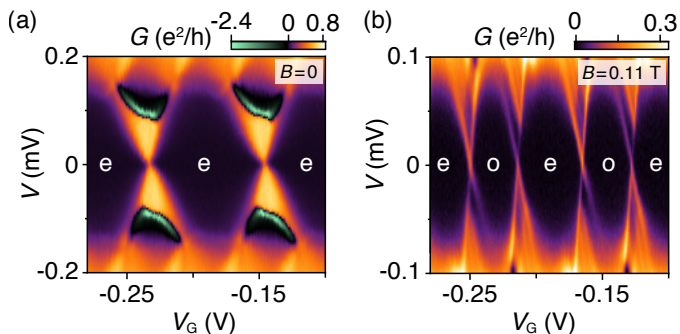


Fig. 4.6: (a) Zero-field conductance measured for device f2, 210 nm island as a function of source-drain bias voltage, V , and plunger gate voltage, V_G , showing $2e$ Coulomb diamonds with even (e) valleys only. The negative differential conductance is associated with quasiparticle trapping on the island (see text). (b) Similar to (a) but measured in the first lobe at $B = 110$ mT, reveals discrete, near-zero-energy state, even (e) and odd (o) valleys of different sizes, and alternating excited state structure.

superconducting lobe, as the superconducting gap decreased below the charging energy of the island. The peaks then became $1e$ -periodic (within experimental sensitivity) around 55 mT and throughout the first destructive regime (see Fig. 4.1 for the onset of destructive regime). When superconductivity reappeared in the first lobe, the Coulomb peaks did not become spaced by $2e$ again, but instead showed nearly $1e$ spacing with even-odd modulation. The 210 nm island showed a qualitatively similar even-odd also in the second lobe. Unlike device f1 described in Fig. 4.2, the shortest island in device f2 also showed a third superconducting lobe, which can be identified from the peak height contrast in Fig. 4.5(b). Coulomb blockade peaks were $1e$ -periodic within experimental sensitivity throughout the third lobe.

Tunneling spectra at finite source-drain bias showed $2e$ Coulomb

diamonds around zero field [Fig. 4.6(a)] and nearly $1e$ diamonds at $B = 110$ mT, near the middle of the first lobe [Fig. 4.6(b)]. The zero-field diamonds are indistinguishable from each other, showing a region of negative differential conductance associated with the onset of quasi-particle transport [113–115]. In the first lobe [Fig. 4.6(b)], Coulomb diamonds alternate in size and symmetry, with degeneracy points showing sharp, gapped structure, indicating that the near-zero-energy state is discrete. Additional resonances at finite bias reflect excited discrete subgap states away from zero energy.

All islands showed $2e$ -periodic Coulomb peaks in the zeroth lobe and nearly $1e$ spacing in the first lobe. Examining the 420 nm and 810 nm data in Fig. 4.7 already reveals that the mean difference between even and odd peak spacings in the first lobe decreased with increasing island length. To address this question quantitatively, we determine the lever arm, η , for each island independently in order to convert plunger gate voltages to chemical potentials on the islands, using the slopes of the Coulomb diamonds [61, 116]. This allows the peak spacing differences [Fig. 4.7(b) and 4.7(e)] to be converted to island-energy differences, $A(L)$, between even and odd occupations, as a function of device length, L . The measured lever arms and even-odd peak spacing difference as well as the resulting hybridization amplitudes for all six islands are summarized in Appendix B.1. A detailed, exemplar peak spacing analysis is presented in Appendix B.2.

Within a Majorana picture, the energy scale $A(L)$ reflects the length dependent hybridization energy of MZMs. Values for $A(L)$ at $B = 110$ mT, in the middle of the first lobe, spanning over two orders of magnitude are shown in Fig. 4.8. A fit to an exponential $A = A_0 e^{-L/\xi}$ yields fit parameters $A_0 = 105 \mu\text{eV}$ and $\xi = 180$ nm. The data are well described by an exponential length dependence, implying that the low-energy modes are located at the ends of the wire, not bound to impurities or local potential fluctuations as expected for overlapping Majorana modes. Along with length dependent even-odd peak spacing difference, we observe even-odd modulation

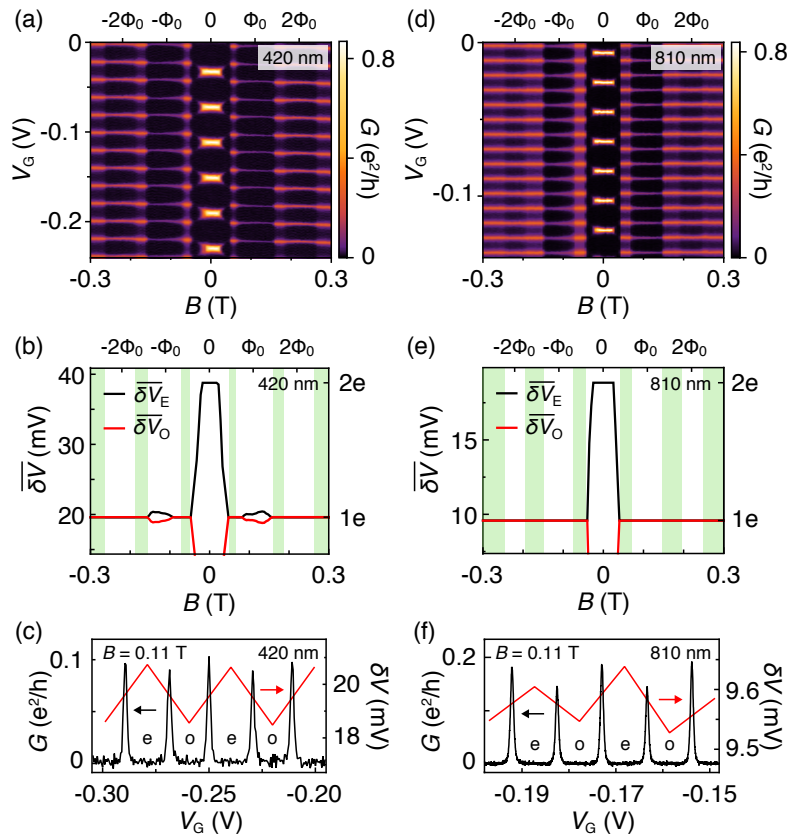


Fig. 4.7: (a) Zero-bias conductance showing Coulomb blockade evolution with V_G and B for device f2, 420 nm island. (b) Average peak spacing for data in (a). Even-odd pattern is evident in the first lobe, around $B = 110$ mT. (c) Fine-scale Coulomb peak conductance (black, left axis) and spacing (colored, right axis) as a function of plunger gate voltage, V_G at $B = 110$ mT for 420 nm island. (d)–(f) Similar to (a)–(c) for 810 nm island. Even-odd spacing in the first lobe is not visible on this scale.

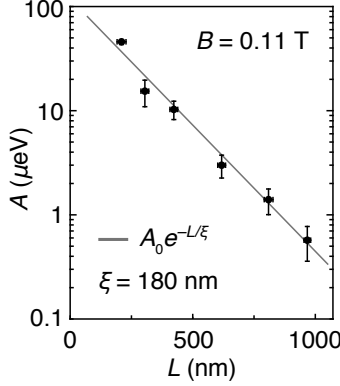


Fig. 4.8: Average even-odd peak spacing difference for device f2 converted to energy, A , using separately measured level arms for each segment, at $B = 110$ mT as a function of island length, L , along with the best fit to the exponential form $A = A_0 e^{-L/\xi}$, giving the best fit parameters $A_0 = 105 \mu\text{eV}$ and $\xi = 180$ nm. Vertical error bars indicate uncertainties from standard deviation of $\overline{\delta V}$ and lever arms. Experimental noise floor, $\sigma_A < 0.1 \mu\text{eV} \ll k_B T$, measured using $1e$ spacing in destructive regime. Horizontal error bars indicate uncertainties in lengths estimated from the micrograph.

in peak heights [Fig. 4.7(c) and 4.7(f)]. Possible explanation of these phenomena was proposed in Ref. [117]. Additionally, we find a complex alternating peak-height structure depending on magnetic field within the first lobe. Peak height modulation accompanying peak spacing modulation was observed previously [61, 110, 111].

4.5 SANITY CHECK

To investigate how coherence length ξ , extracted from the exponential decrease of even-odd peak spacing with length, depends on the superconducting gap, Δ , we examine peak spacing near

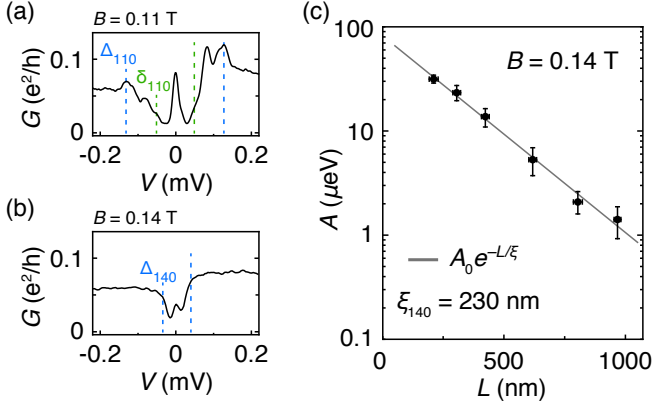


Fig. 4.9: (a) Line-cut of the conductance measured for device f1 at $B = 110$ mT and $V_{\text{BG}} = -1.05$ V. The dashed lines indicate the main superconducting gap at $\Delta_{110} = \pm 130$ μeV (blue) and the lowest excited state at $\delta_{110} = \pm 50$ μeV (green). (b) same as (a) but taken at $B = 140$ mT. The blue dashed lines indicate the gap at 140 mT, $\Delta_{140} = \pm 40$ μeV . No subgap states are observed at 140 mT. (c) Difference of average even and odd Coulomb peak spacings, A , measured for device f2 at $B = 140$ mT as a function of island length, L . The best fit to the exponential $A = A_0 e^{-L/\xi}$ (gray) yields $A_0 = 80$ μeV and $\xi_{140} = 230$ nm. Uncertainties in amplitude are deduced from standard deviation of $\overline{\delta V}$ and lever-arm; uncertainties in lengths are estimated from the electron micrograph.

the high-field edge of the first lobe, $B = 140$ mT, where the gap is reduced to $\Delta_{140} = 40$ μeV , and shows no subgap features besides the zero-bias peak [Fig. 4.9(b)]. At this reduced gap we again find an exponential dependence on length, and incompatibility with a power law, now with $\xi = 230$ nm [Fig. 4.9(c)]. We observe that $\xi_{140}/\xi_{110} = 230 \text{ nm}/180 \text{ nm} \sim 1.3$ is consistent with simple scaling, $\xi \propto \Delta^{-1}$ (not accounting for a field-dependent velocity). From Fig. 4.9, $\delta_{110}/\Delta_{140} = 50 \text{ } \mu\text{eV}/40 \text{ } \mu\text{eV} \sim 1.2$, where δ_{110} is the lowest non-zero

subgap state, and $\delta_{140} = \Delta_{140}$. We also note that both ξ_{110} and ξ_{140} are slightly smaller than the coherence length in the superconducting shell at corresponding B field values: $\xi_S(110 \text{ mT}) \sim 190 \text{ nm}$ and $\xi_S(140 \text{ mT}) \sim 250 \text{ nm}$, extracted from data in Fig. 4.1(d) using Eq. (4.1) and the corresponding values of $T_C(B)$. This discrepancy may be interpreted as resulting from the velocity renormalization in the semiconductor in the strong coupling limit [118–120].

4.6 DISCUSSION

In summary, we have demonstrated that that threading magnetic flux through a semiconductor nanowire fully covered by a superconducting shell can induce a topological phase with Majorana zero modes at the nanowire ends. While being of similar simplicity and practical feasibility [57] as the original nanowire proposals with a partial shell coverage [44, 45], full-shell nanowires may provide key advantages. First, the topological transition in a full-shell wire is driven by the field-induced winding of the superconducting order parameter, rather than by the Zeeman effect so that, as demonstrated in the reported measurements, the required magnetic fields can be very low ($\sim 0.1 \text{ T}$). Therefore, the present proposal is compatible with conventional superconducting electronics and removes the need for a large g factor semiconductor, potentially expanding the landscape of candidate materials. Moreover, the full shell naturally protects the semiconductor from impurities and random surface doping, thus enabling a reproducible way of growing many wires with essentially identical electrostatic environments. The modest magnetic field requirements, protection of the semiconductor core from surface defects, and locked phase winding in discrete lobes together suggest a new and relatively easy route to creating and controlling Majorana zero modes in hybrid materials. Our findings open a possibility to study an interplay of mesoscopic and topological physics in this novel system.

ANOMALOUS PHASE IN DESTRUCTIVE SUPERCONDUCTORS

The Little-Parks effect—a flux-dependent modulation of the transition temperature in multiply connected superconductors—results from the quantization of fluxoid through holes in superconductors. In hollow superconducting cylinders with diameter smaller than the superconducting coherence length, flux-induced supercurrents can give rise to the destructive Little-Parks effect, characterized by repeated reentrant quantum phase transitions between superconducting and metallic phases. Here, we use axial and transverse magnetic fields to control the crossover between the conventional and destructive Little-Parks regimes in nanowires with an epitaxial Al shell fully surrounding InAs core. The observed dependence on flux, transverse field, temperature, and current bias is in excellent agreement with theory. Near the crossover between the conventional and destructive regimes, an anomalous metal phase is found. The anomalous metallic phase is characterized by a field-controllable, temperature-independent resistivity between adjacent superconducting lobes.

This chapter is adapted from Ref. [121]. The experiment was conducted under the supervision of Charles Marcus. The nanowires were grown by Peter Krogstrup.

5.1 SMALL CYLINDRICAL SHELLS

Quantum phase transitions (QPT) [122, 123] in conventional superconductors serve as prototypes for related effects in more complex, strongly-correlated systems [124], including heavy-fermion materials [125] and high-temperature superconductors [126]. While low-temperature superconductors are well understood in bulk, new phenomena can arise in mesoscopic samples and reduced dimensionality [10, 127]. For instance, in two-dimensional films, electrons theoretically condense into either a superconductor or insulator in the low-temperature limit [128]. Yet, in many instances, an anomalous metallic state with finite temperature-independent resistance is found at low temperatures [129]. In one-dimensional wires, incoherent phase slips can destroy superconductivity [130] or give rise to an anomalous metallic state [131], while coherent quantum phase slips can lead to superposition of quantum states enclosing different numbers of flux quanta [132], potentially useful as a qubit [133].

Multiply connected superconductors provide an even richer platform for investigating phase transitions. Fluxoid quantization in units of $\Phi_0 = h/2e$ [134, 135], reveals not only electron pairing but a complex macroscopic order parameter, $\Delta e^{i\varphi}$ [10, 136]. The same physical mechanism underlies the Little-Parks effect, a periodic modulation of the transition temperature, T_C , of a superconducting cylinder with magnetic flux period Φ_0 [17]. For hollow superconducting cylinders with diameter, d , smaller than the coherence length, the modulation amplitude can exceed zero-field transition temperature, T_{C0} , leading to a reentrant destruction of superconductivity near odd half-integer multiples of Φ_0 [89, 107, 137].

Early experimental investigation of the destructive Little-Parks effect reported reentrant superconductivity interrupted by an anomalous-resistance phase around applied flux $\Phi_0/2$ [90]. Subsequent experiments showed a low-temperature phase with normal-state resistance, R_N , around $\Phi_0/2$, but did not display fully recovered

superconductivity at higher flux [91]. Several theoretical models were proposed to interpret these different scenarios [138–140], but no consensus emerged.

In this chapter we report a study of the Little-Parks effect in InAs nanowires with a thin epitaxial cylindrical Al shell, demonstrating the relation between destructive superconductivity and various experimentally controllable parameters. Excellent agreement with Ginzburg-Landau mean field theory is found as a function of flux, temperature, and current bias, using independently measured material and device parameters. We then investigate a field-tunable crossover from non-destructive to destructive regime. At the boundary, an anomalous metal phase is identified, characterized by a temperature-independent resistance that can be tuned over a broad range using perpendicular magnetic field, B_{\perp} . We interpret these results in terms of tunneling between two adjacent fluxoid states with different phase winding numbers giving rise to an anomalous metallic phase. However, as noted previously [139], the appear-

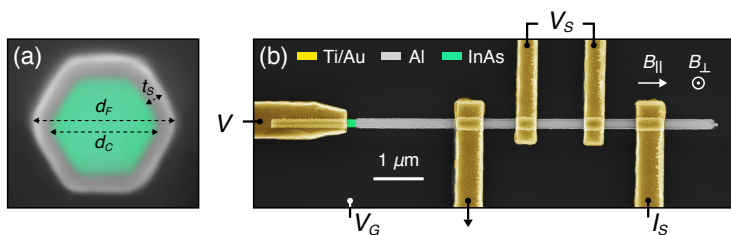


Fig. 5.1: (a) Colorized material-sensitive scanning electron micrograph of InAs-Al hybrid nanowire cross-section. The full wire diameter d_F , core diameter d_C and shell thickness t_S are indicated by dashed arrows. (b) Representative color-enhanced micrograph of a device (wire d2) consisting of an InAs core (green) with Al shell (grey), contacted with Ti/Au leads (yellow). The device can be operated in voltage (V) and current (I_S) bias measurement set-ups.

ance of a field-tunable temperature-independent resistance does not emerge naturally from simple generic models.

The devices we investigated were made using InAs nanowire grown by the vapor-liquid-solid (VLS) method using molecular beam epitaxy (MBE). Following wire growth, an epitaxial Al layer was grown within the MBE chamber while rotating the sample stage, resulting in a full cylindrical Al shell coating the wire [57], as shown in Fig. 5.1(a). Subsequent fabrication used standard electron-beam lithography, deposition, etching, and liftoff, as described in Appendix A. Devices were operated in two configurations [Fig. 5.1(b)]: In the first configuration, four Au contacts were made to the Al shell allowing four-wire resistance measurements; in the second, an additional tunneling contact to the InAs core at the end of the wire was used as a tunnel probe, giving local density of states, as discussed in Chapter 4. We investigated wires from three growth batches, denoted d1 (batch 638), d2 (batch 439), and d3 (batch 564), with different core diameters, d_C , and shell thicknesses, t_S (Appendix C.1). Transport measurements were carried out in a dilution refrigerator with a three-axis vector magnet and base temperature of 20 mK.

5.2 PAIR-BREAKING WITH TEMPERATURE & FLUX

Carrier density in the InAs core is predominantly at the Al interface due to band bending [72,73]. Moreover, the density of carriers in Al is orders of magnitude higher than in InAs. We may therefore consider current to be carried by a hollow cylinder which is threaded by flux in an axial applied magnetic field. Induced circumferential supercurrents from the applied flux lead to Cooper pair breaking, characterized by the parameter α , which controls the transition temperature $T_C(\alpha)$, as described by Abrikosov-Gorkov expression,

$$\ln\left(\frac{T_C(\alpha)}{T_{C0}}\right) = \Psi\left(\frac{1}{2}\right) - \Psi\left(\frac{1}{2} + \frac{\alpha}{2\pi T_C(\alpha)}\right) \quad (5.1)$$

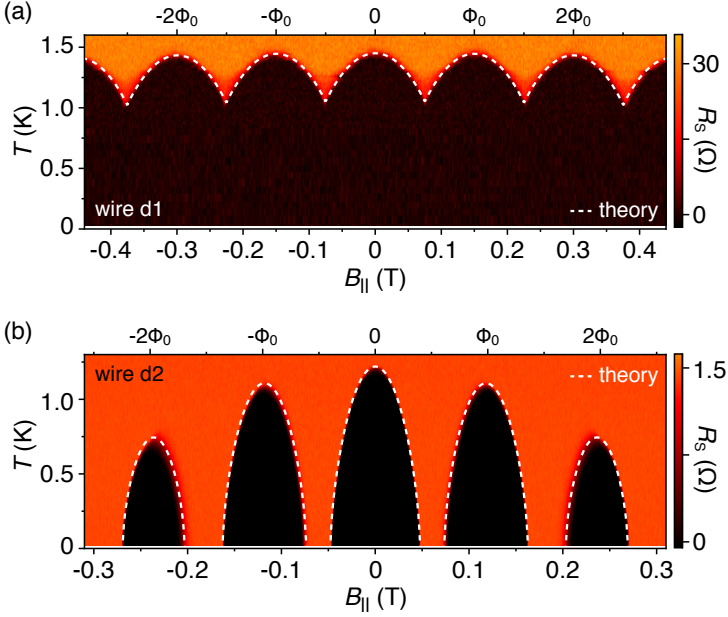


Fig. 5.2: (a) Shell resistance, R_S , measured for wire d1 with shell thickness $t_S = 7$ nm as a function of axial magnetic field, B_{\parallel} , and temperature, T . The superconducting transition temperature of the shell is periodically modulated by B_{\parallel} . The sample is superconducting for temperatures below 1 K throughout the whole measured B_{\parallel} range. The dashed theory curve is Eq. (5.1) evaluated with α_{\parallel} from Eq. (5.2) and the corresponding fit parameters measured for the wire d1. (b) Same as (a), but measured for wire d2 with shell thickness around $t_S = 25$ nm, showing the destructive regimes around $\pm\Phi_0/2$ and $\pm 3\Phi_0/2$ of the applied flux quantum.

where Ψ is the digamma function [141]. Following Refs. [91,107,138], the pair-breaking parameter for a hollow cylinder with wall thickness t_S in a parallel magnetic field B_{\parallel} is given by

$$\alpha_{\parallel} = \frac{4 \xi_S^2 T_{C0}}{A_F} \left[\left(n - \frac{\Phi}{\Phi_0} \right)^2 + \frac{t_S^2}{d_F^2} \left(\frac{\Phi^2}{\Phi_0^2} + \frac{n^2}{3} \right) \right] \quad (5.2)$$

where ξ_S is the zero-field superconducting coherence length, A_F is the area of the cylinder cross section, the integer n is the fluxoid quantum number, Φ is the applied flux, and d_F is the diameter of the cylinder [Fig. 5.1(a)]. Taking the dirty-limit expression for $\xi_S = \sqrt{\pi \hbar v_F l_e / 24 k_B T_{C0}}$ with the Fermi velocity v_F and mean free path l_e , we note that all parameters can either be measured directly from the micrograph of the device or from independent transport measurements, see Appendix C.1.

Differential shell resistances, $R_S = dV_S/dI_S$, for wires d1 and d2 are shown in Fig. 5.2 as a function of B_{\parallel} and temperature, T . Wires d1 and d2 have similar core diameters, $d_C \sim 135$ nm, but different shell thicknesses. For wire d1, with $t_S = 7$ nm, T_C is finite throughout the measured range, and varies periodically with applied axial flux with amplitude ~ 0.4 K with no clear envelope reduction up to $B_{\parallel} = 0.4$ T. Normal-state resistance of the wire yields a coherence length $\xi_S = 70$ nm, smaller than d_C (Appendix C.1). In contrast, wire d2, with $t_S = 25$ nm, has $\xi_S = 180$ nm $> d_C$, and shows destructive regimes around $\pm \Phi_0/2$ and $\pm 3\Phi_0/2$. Resistances in these destructive regimes remain equal to the normal state resistance, $R_S = R_N$, to the lowest measured temperatures.

The absence (presence) of the destructive regime in wire d1 (d2) is consistent with the criterion of the superconducting coherence length being smaller (larger) than the wire diameter [89]. To be more quantitative, we plot in Fig. 5.2 theoretical curves marking the superconductor-metal transition based on Eqs. (5.1) and (5.2) with independently measured wire parameters, using either the

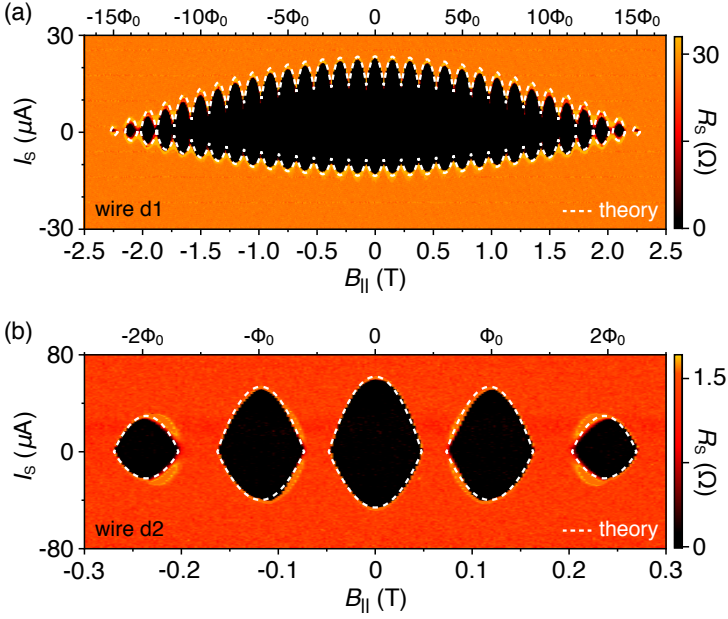


Fig. 5.3: (a) Shell resistance, R_S , measured for wire d1 with shell thickness $t_S = 7$ nm as a function of axial magnetic field, B_{\parallel} , and current bias, I_S . Both switching and re-trapping currents are periodically modulated by B_{\parallel} up to $B_{\parallel,C} = 2.3$ T, whereafter the supercurrent is suppressed. The dashed theory curve is Eq. (5.3) evaluated with α_{\parallel} from Eq. (5.2) and the corresponding fit parameters measured for wire d1. (b) Same as (a), but measured for wire d2 with shell thickness around $t_S = 25$ nm.

measured zero-field critical temperature, T_{C0} or, equivalently, the spectroscopically measured zero-field superconducting gap, Δ_0 , (Fig. C.1 in Appendix C.2), which was consistent with the BCS relation $\Delta_0 = 1.76 k_B T_{C0}$ [10]. Figure 5.2 demonstrates the remarkably good agreement found between experiment and theory. The observed increase of T_C with decreasing t_S is consistent with enhanced energy gaps for thin Al films [142].

5.3 CURRENT-DRIVEN PHASE TRANSITIONS

Similar to the effects of flux-induced circumferential supercurrent, a dc current, I_S , applied along the wire can also drive the shell normal. The field-dependent critical current $I_C(\alpha)$ can be related to the corresponding critical temperature, $T_C(\alpha)$,

$$I_C(\alpha) = I_{C0} \left(\frac{T_C(\alpha)}{T_{C0}} \right)^{3/2} \quad (5.3)$$

where I_{C0} is the zero-field critical current [143].

Base-temperature I_S - B_{\parallel} phase diagrams for wires d1 and d2 are shown in Fig. 5.3. The data are taken sweeping from negative to positive bias, so show re-trapping currents for $I_S < 0$ and switching current for $I_S > 0$, both of which are proportional to the critical current, I_C [10]. Similar to the transition temperature, I_C was observed to be Φ_0 -periodic in flux for both wires as expected from Eq. (5.3). For wire d1, a bigger range of B_{\parallel} [Fig. 5.3(a)] shows that the thin shell remains non-destructive up to ~ 2 T, corresponding to $\sim 13\Phi_0$, then enters the destructive regime twice around $14\Phi_0$ and finally turns fully normal around $B_{\parallel,C} = 2.3$ T.

Figure 5.3 shows theoretical curves based on Eqs. (5.1)–(5.3) superimposed on experimental data for both wire types. The zero-field switching and re-trapping currents were taken as input parameters, with other parameters measured independently. Again, excellent agreement between experiment and theory for both thin (wire d1)

and thick (wire d2) shells was found.

5.4 PERPENDICULAR MAGNETIC FIELD

We next consider the effects of an applied *transverse* magnetic field, B_{\perp} , which can be used to control a crossover between conventional and destructive Little-Parks regimes. We investigate the combined effects of B_{\parallel} and B_{\perp} in wire d3, with $d_C = 240$ nm and $t_S = 40$ nm. The larger diameter reduces the field value $B_{\parallel} = \Phi_0/A_F$ and the thicker shell ensures a long ξ_S , such that initially the wire is nearly destructive. The transition of the wire d3 from being non-destructive at $B_{\perp} = 0$ to destructive at $B_{\perp} = 13$ mT is depicted by I_S - B_{\parallel} phase diagrams in Figs. 5.4(a)–5.4(c).

Theoretically, the effect of B_{\perp} on the superconducting transition can be accounted for by introducing an additional pair-breaking term [124],

$$\alpha_{\perp} = \frac{4 \xi_S^2 T_{C0} \Phi_{\perp}^2}{A_F \Phi_0^2} \quad (5.4)$$

where $\Phi_{\perp} = B_{\perp} A_F$. Figures 5.4 and 5.5 show the theoretical transitions based on Eqs. (5.1)–(5.4) using $\alpha = \alpha_{\parallel} + \alpha_{\perp}$ [144] superimposed on experimental data.

Near the conventional-destructive crossover [Fig. 5.4(b)], a resistive state with R_S smaller than R_N was observed around $\pm\Phi_0/2$ and $I_S = 0$. Figures 5.6 and 5.7 examine this resistive state close to the crossover, around $B_{\perp} \sim 12$ mT, along with superimposed theory curves based on Eqs. (5.1)–(5.4). Note that unlike the situation far from the crossover [Fig. 5.6(a)], where theory and experiment agree well, in the vicinity of the crossover [Fig. 5.6(b) and 5.6(c)] mean-field theory predicted T_C deviates from the temperatures where the shell displays R_N .

Temperature dependence of R_S around $-\Phi_0/2$ for several values B_{\perp} near the conventional-destructive crossover are shown in

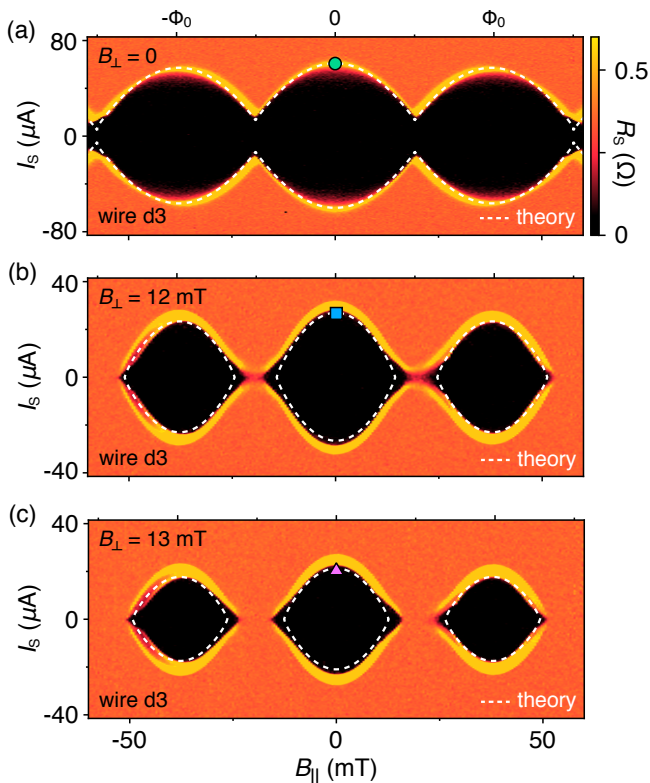


Fig. 5.4: (a) Base-temperature shell resistance, R_S , measured for wire d3 as a function of current bias, I_S , and parallel magnetic field, B_{\parallel} , at zero perpendicular magnetic field, $B_{\perp} = 0$. The wire is non-destructive throughout the whole measured B_{\parallel} range. (b) Same as (a), but at $B_{\perp} = 12$ mT. Around $\Phi_0/2$ and $I_S = 0$, an anomalous phase develops with a finite, but smaller than normal state resistance. (c) Same as (a), but measured at $B_{\perp} = 13$ mT. Around $\Phi_0/2$ quantum R_S remains at normal state value even at $I_S = 0$. The theory curves in (a)–(c) are Eq. (5.3) evaluated with $\alpha = \alpha_{\parallel} + \alpha_{\perp}$.

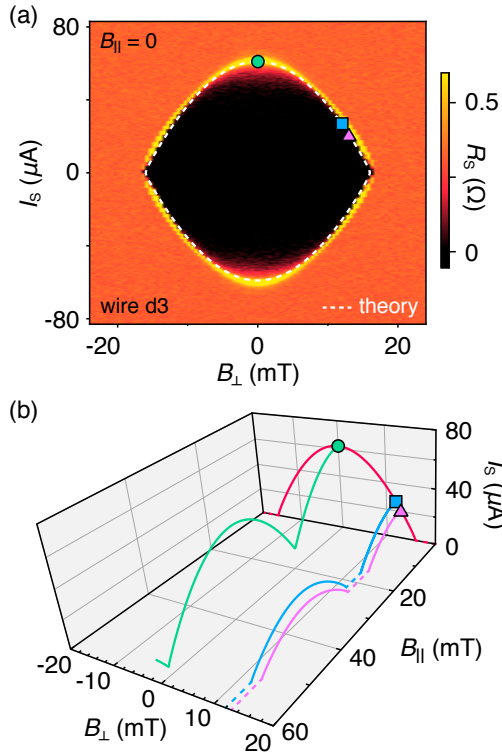


Fig. 5.5: (a) Critical current evolution for wire d3 as a function of B_{\perp} measured at $B_{\parallel} = 0$. The theory curve is Eq. (5.3) computed with α_{\perp} . (b) Schematic representation of the critical current for wire d3 as a function of B_{\parallel} and B_{\perp} . The colored markers indicate the same field and current values as in (a) and Fig 5.4.

Fig. 5.7(a). Throughout this regime, R_S was found to saturate to a temperature independent value, which can be tuned over two orders of magnitude with small changes in B_\perp . In contrast, a R_S - T trace taken close to the second destructive regime, not near a crossover ($B_\perp = 12$ mT and $B_\parallel = 52$ mT) remains temperature dependence down to the base temperature (Fig. C.2 in Appendix C.3). Qualitatively similar anomalous R_S saturation was also observed for different B_\parallel values at a fixed B_\perp , see Fig. C.3 in Appendix C.4. At base temperature the evolution of R_S as a function of B_\perp shows a steplike increase, that is mostly pronounced around $\pm\Phi_0/2$, see Fig. 5.7(b).

A possible explanation for the saturation of R_S in terms of disorder-induced variations of Δ , separating the shell into normal and superconducting segments [138] was tested by examining saturation effects in three segments of the same wire (Fig. C.4 in Appendix C.5). It was found that all segments behaved the same, arguing against long-range variation in Δ on the scale of the separation of contacts. We also note that the anomalous resistance develops predominantly above the theoretical T_C , where the sample is expected to be in the normal state (Fig. C.5 in Appendix C.6).

The steplike increase of R_S with B_\perp shown in Fig. 5.7(b) is reminiscent of phase slips, similar to the ones observed in Refs. [130, 144], except here they are activated by the perpendicular field rather than temperature. This suggests a picture in which anomalous saturating resistance results from quantum fluctuations not captured by the mean-field theory. In general, the probability of a transverse phase slip across a weak link is proportional to $\exp(-R_Q/R_N)$, with the resistance quantum R_Q , and therefore is exponentially small for wire d3 [145]. However, near one-half flux quantum, states with consecutive phase windings around the shell are degenerate, allowing quantum fluctuations to play a role.

Finally, it might be worth noting that for wire d3, $\lambda^2 \lesssim d_F t_S/2$ within the error, where λ is the effective penetration depth. In this

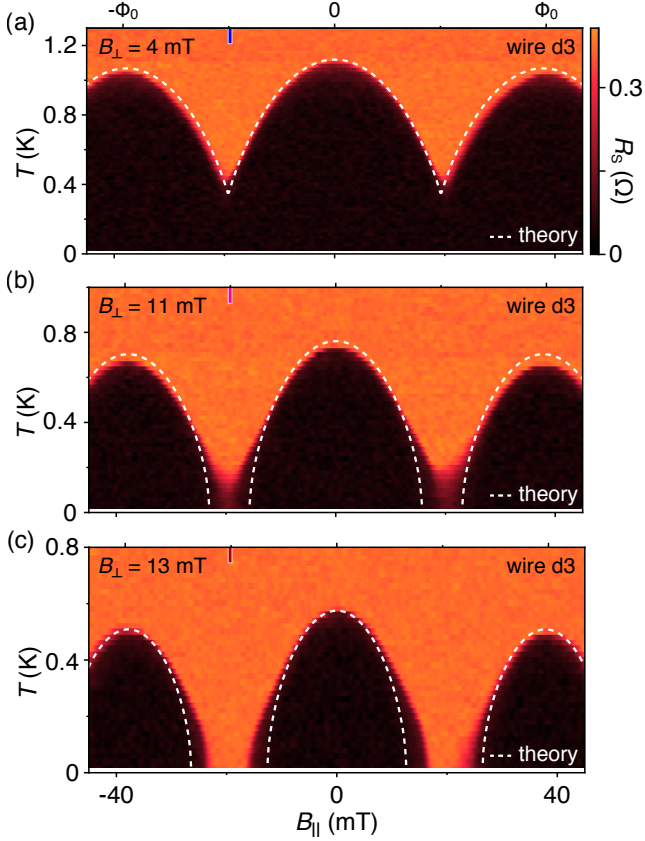


Fig. 5.6: (a) Differential shell resistance, R_S , measured for wire d3 at $B_{\perp} = 4$ mT as a function of temperature, T , and parallel magnetic field, B_{\parallel} . For small B_{\perp} the sample displays a non-destructive T - B_{\parallel} phase diagram. (b) Same as (a), but measured at $B_{\perp} = 11$ mT. Around $\pm\Phi_0/2$ an anomalous-resistance phase develops at low T . (c) Same as (a), but measured at $B_{\perp} = 13$ mT. The shell resistance increases to the normal state value as the applied flux passes $\pm\Phi_0/2$, even at the base temperature. Note that R_S is finite for all temperatures above the mean-field theory predicted T_C . The theory curves in (a)–(c) are Eq. (5.1) numerically solved for $T_C(\alpha_{\parallel} + \alpha_{\perp})$.

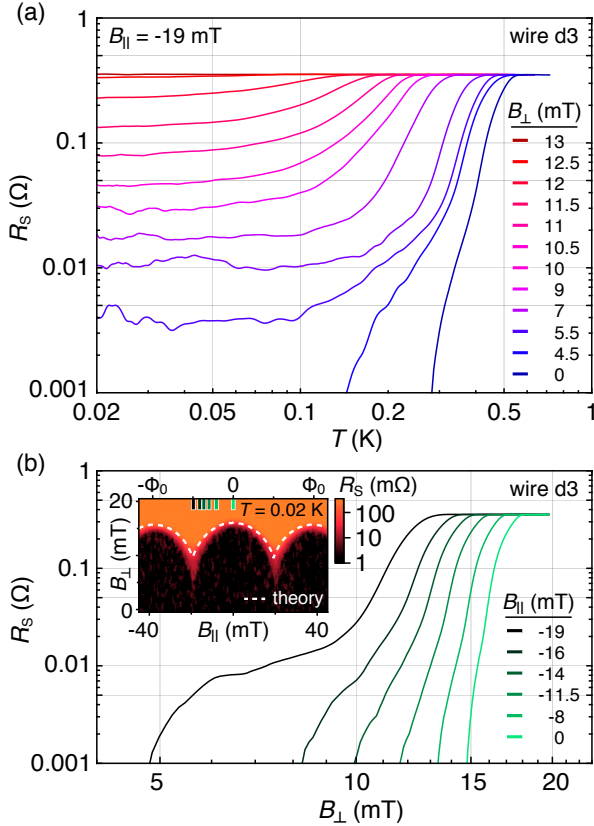


Fig. 5.7: (a) Half-flux quantum R_S for wire d3 as a function of T measured at different B_{\perp} values. Close to $B_{\perp} = 0$, as the temperature is lowered, the sample displays a conventional normal-superconducting phase transition. Around $B_{\perp} = 5$ mT the shell resistance at low T saturates to a finite, B_{\perp} -dependent value. Above $B_{\perp} = 13$ mT the shell resistance does not decrease below the normal state resistance. (b) Base-temperature R_S as a function of B_{\perp} measured at different B_{\parallel} or Φ values. The resistance increases with B_{\perp} in a steplike manner with the step feature mostly pronounced at around $-\Phi_0/2$ of the applied flux. Inset: R_S as a function of B_{\perp} and B_{\parallel} . The theory curve was computed using Eq. (5.1), where a critical B_{\perp} was found for each B_{\parallel} , above which T_C vanishes.

limit, QPT is expected to be of the first order, allowing a metastable states [136, 138]. How this would affect expectations is not known.

5.5 SUMMARY

The measured superconducting-normal phase diagrams for small epitaxial Al cylinders grown on InAs nanowires are well described by the phenomenological Ginzburg-Landau mean-field theory. Depending on the wire diameter and the shell thickness a sample can display both non-destructive and destructive Little-Parks regimes. A moderate perpendicular magnetic field can tune a non-destructive sample into an anomalous state with a saturating half-flux quantum resistance, resembling a quantum fluctuations induced tunneling of the system between two adjacent ground states characterized by different phase windings. The resulting superposition of quantum states with different numbers of flux quanta could potentially be useful as a qubit.

6

SELECTIVE AREA GROWN HYBRIDS

In this chapter we introduce selective area grown hybrid InAs/Al nanowires based on molecular beam epitaxy, allowing arbitrary semiconductor-superconductor networks containing loops and branches. Transport reveals a hard induced gap and unpoisoned $2e$ -periodic Coulomb blockade, with temperature dependent $1e$ features in agreement with theory. Coulomb peak spacing in parallel magnetic field displays overshoot, indicating an oscillating discrete near-zero subgap state consistent with device length. Finally, we investigate a loop network, finding strong spin-orbit coupling and a coherence length of several microns. These results demonstrate the potential of this platform for scalable topological networks among other applications.

6.1 LOOPS & BRANCHES

Majorana zero modes (MZMs) at the ends of one-dimensional topological superconductors are expected to exhibit non-abelian

This chapter is adapted from Ref. [146]. The experiment was conducted under the supervision of Charles Marcus. Alexander Whiticar, Mingtang Deng and Lucas Casparis assisted with the fabrication, measurements and data analysis. The TEM micrograph was taken by Sara Marti-Sanchez and Jordi Arbiol. The selective-area-grown materials were developed by Filip Krizek, Joachim Sestoft, Chris Palmstrøm, and Peter Krogstrup.

braiding statistics [24, 38], providing naturally fault-tolerant qubits [25, 27]. Proposed realizations of braiding [52, 53], interference-based topological qubits [147–149] and topological quantum computing architectures [39] require scalable nanowire networks. While relatively simple branched or looped wires can be realized by specialized growth methods [57, 150] or by etch- and gate-confined two-dimensional hybrid heterostructures [151–154], selective area growth [155] enables deterministic patterning of arbitrarily complex structures. This allows complex continuous patterns of superconductor-semiconductor hybrids and topological networks.

Following initial theoretical proposals [44, 45], a number of experiments have reported signatures of Majorana zero modes (MZMs) in hybrid semiconductor-superconductor nanowires [57], including zero-bias conductance peaks [54–56, 59, 153, 154, 156–158] and Coulomb blockade peak spacing oscillations [61, 159]. To date, experiments have used individual vapor-liquid-solid (VLS) nanowires [54–56, 59, 156, 157] or gate-confined two-dimensional heterostructures [153, 154]. Within these approaches, constructing complex topological devices and networks containing branches and loops [39, 52, 53, 147–149] is a challenge. Recently, branched and looped VLS growth has been developed toward this goal [150, 160].

In this chapter, we investigate a novel approach to the growth of semiconductor-superconductor hybrids that allows deterministic on-chip patterning of topological superconducting networks based on SAG. We characterize key physical properties required for building Majorana networks, including a hard superconducting gap, induced in the semiconductor, phase-coherence length of several microns, strong spin-orbit coupling, and Coulomb blockade peak motion compatible with interacting Majoranas. Overall, these properties show great promise for SAG-based topological networks.

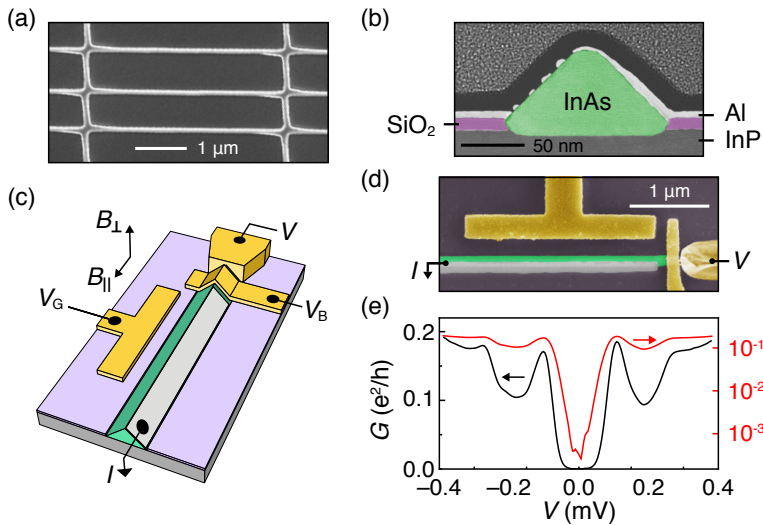


Fig. 6.1: (a) Scanning electron micrograph of a SAG hybrid network. (b) False-colored annular dark field scanning transmission electron micrograph of a nanowire cross-section displaying InP substrate, InAs (green) nanowire, Al (gray) shell and SiO_2 (purple) mask. (c) Measurement set-up for device s1 showing the gate voltages and orientations of magnetic fields used in the measurements. (d) False-colored electron micrograph of device s1. (e) Differential conductance, G , as a function of source-drain bias, V , in linear (black) and logarithmic (red) scales shows a hard superconducting gap.

6.2 ELECTRON DISTRIBUTION IN SAG WIRES

Selective area growth (batch 660) was realized on a semi-insulating (001) InP substrate. PECVD grown SiO_x was patterned using electron beam lithography and wet etching. InAs wires with triangular cross-sections were grown by molecular beam epitaxy (MBE). The Al was grown *in-situ* MBE using angled deposition covering one of the facets. The excess Al was removed by wet etching [Figs. 6.1(a)–6.1(c)]. The details of the semiconductor growth are given in Ref. [155], while it is superconductor-semiconductor proximity effects that are emphasized in the present study. Data from four devices, denoted s1 to s4, are presented. Device s1 [Fig. 6.1(d)] consists of a single barrier at the end of a $4 \mu\text{m}$ wire, defined by a lithographically patterned gate adjacent to a Ti/Au contact where the Al has been removed by wet etching. This device allowed density of states measurement at the end of the wire by means of bias spectroscopy, to investigate the superconducting proximity effect in the InAs. Evolution of Coulomb blockade in temperature and magnetic field was studied in device s2 [Fig. 6.3(b)]—a hybrid quantum dot with length of $1.1 \mu\text{m}$ defined by two Ti/Au gates adjacent to etched-Al regions. The barrier voltages V_B were used to create tunneling barriers. The chemical-potential in the wires was tuned with gate voltage V_G . Device s3—top-gated nanowire without Al (Fig. 6.5)—was used to extract the charge carrier mobility. Device s4 was a micron-size square loop [Fig. 6.6(a)] with fully removed Al, which was used to extract phase coherence lengths from weak antilocalization (WAL) and Aharonov-Bohm (AB) oscillations. The nanowires in devices s1, s2 and s3 are parallel to [100] direction, whereas the arms of device s4 are oriented along [100] and [010] directions. Standard ac lock-in measurements were carried out in a dilution refrigerator with a three-axis vector magnet. See Appendix A for more detailed description of the sample preparation and measurements.

Differential conductance, G , in the tunneling regime, as a function

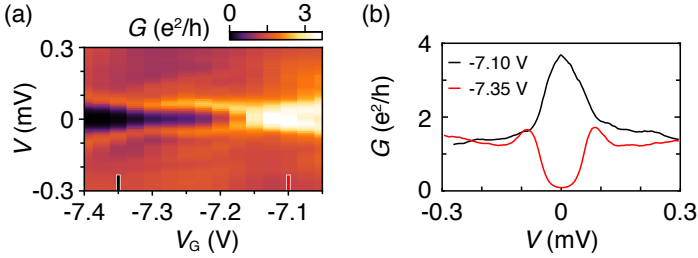


Fig. 6.2: (a) Differential conductance, G , of device s1 [Fig. 6.1(d) and 6.1(c)] as a function of source-drain bias, V , and gate voltage, V_G . (b) Line-cuts taken from (a) display Andreev reflection enhanced conductance (black) measured at $V_G = -7.10$ V evolve into superconducting gap (red) measured at $V_G = -7.35$ V.

of source-drain bias, V , for device s1 [Fig. 6.1(e)] at $V_G = -9.2$ V reveals a gapped density of states with two peaks at $V = 110 \mu\text{eV}$ and $280 \mu\text{eV}$. We tentatively identify the two peaks with two populations of carriers in the semiconductor, the one with a larger gap residing at the InAs-Al interface and with a smaller at the InAs-InP. The magnitude of the larger superconducting gap is consistent with enhanced energy gaps of $290 \mu\text{eV}$ for 7 nm Al film [142]. The zero-bias conductance is ~ 400 times lower than the above-gap conductance, a ratio exceeding VLS nanowire [58, 150, 161] and 2DEG devices [152], indicating a hard induced gap. We note, however, that co-tunneling through a quantum-dot or multichannel tunneling can enhance this ratio [162].

The spectrum evolution with V_G from enhanced to suppressed conductance around zero bias is shown in Fig. 6.2(a). Conductance enhancement in the range of $V_{SD} = -0.1$ mV to 0.1 mV is measured at $V_G = -7.10$ V [Fig. 6.2(b)]. At more negative gate voltage $V_G = -7.35$ V the conductance gets suppressed in the same range of V_{SD} .

We interpret these features to arise due to a different tunnel barrier strengths tuned by the capacitively cross-coupled V_G : at more

positive V_G , the tunneling barrier is more transparent, resulting in Andreev reflection enhanced conductance; at more negative V_G , the transport is dominated by the single electron tunneling, reflecting the local density of states at the end of the wire [19]. At $V_G = -7.10$ V the zero-bias conductance is enhanced beyond the factor of 2 compared to high bias [Fig. 6.2(b)]. We speculate that this is caused by an interfering transport mediated via multiple channels or a quantum dot [162]. A similar study of V_C dependence was not possible presumably due to a too high concentration of disorder in the junction.

6.3 THERMODYNAMICS OF COULOMB BLOCKADE

Transport through a Coulomb island geometry (Fig. 6.3) at low temperatures shows $2e$ -periodic peak spacing as a function of V_G . Coulomb diamonds at finite bias yield a charging energy $E_C = 60 \mu\text{eV}$ (see Fig. D.1 in Appendix D), smaller than the induced gap, $\Delta^* \sim 100 \mu\text{eV}$, as seen in Fig. 6.1(e). The zero-bias Coulomb blockade spacing evolves to even-odd and finally to $1e$ -periodic peaks with increasing temperature, T . The $2e$ to $1e$ transition in temperature does not result from the destruction of superconductivity, but rather arises due to the thermal excitation of quasiparticles on the island, as investigated previously in metallic islands [163, 164] and semiconductor-superconductor VLS nanowires [115].

A thermodynamic analysis of Coulomb blockade peak spacings is based on the difference in free energies, $F = F_O - F_E$, between even and odd occupied states. We consider a simple model that assumes a single induced gap Δ^* , not accounting for the double-peaked density of states in Fig. 6.1(e). At low temperatures ($T \ll E_C, \Delta^*$), F approaches Δ^* . Above a characteristic poisoning temperature, T_p , quasiparticles become thermally activated and F decreases rapidly to zero. For $F(T) > E_C$, Coulomb peaks are $2e$ periodic with even peak spacings, $S_E \propto E_C$, independent of T . For $F(T) < E_C$, odd

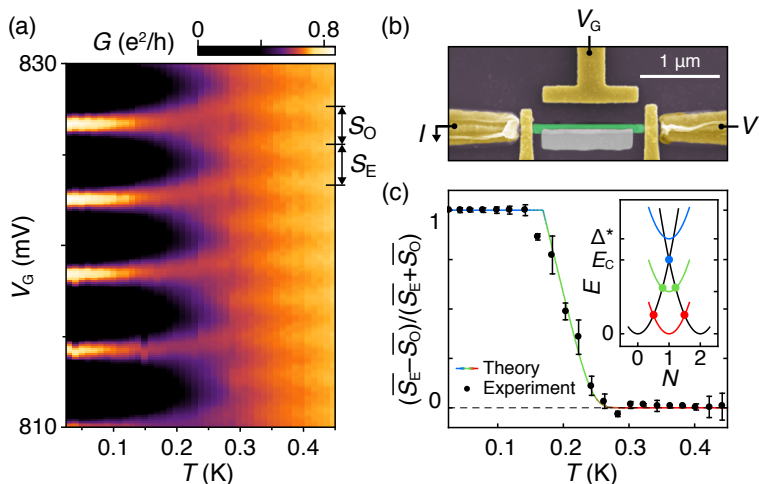


Fig. 6.3: (a) Conductance, G , of device s2 as a function of applied gate voltage, V_G , and temperature, T . A characteristic $2e$ to $1e$ transition occurs around 200 mK. The color scale was adjusted for better visibility. (b) False-colored electron micrograph of device s2. (c) Normalized even-odd peak spacing difference, $(\overline{S_E - S_O}) / (\overline{S_E + S_O})$, from the measurements shown in (a) as a function of T . The error-bars were estimated using standard deviation of the peak spacing. The theoretical fit corresponds to an induced superconducting gap $\Delta^* = 190 \mu\text{eV}$. Inset: Energy, E , of the device as a function of normalized gate voltage, N . Black (colour) parabolas correspond to even (odd)-parity ground state. Transport occurs at the charge degeneracy points indicated by filled circles.

states become occupied, and the difference in peak spacing, $S_E - S_O$, decreases with F . A full analysis following Ref. [115] yields the peak spacing difference

$$\begin{aligned} S_E - S_O &= \frac{2}{\eta e} \min(E_C, F) \\ &= (S_E + S_O) \min(1, F/E_C) \end{aligned} \quad (6.1)$$

where η is the dimensionless gate lever arm measured from Coulomb diamonds (see Appendix D).

Figure 6.3(c) shows the measured even-odd difference in peak spacing, $(\overline{S_E} - \overline{S_O})/(\overline{S_E} + \overline{S_O})$, averaged over 4 peaks in device s2, along with Eq. (6.1). Thermodynamic analysis shows an excellent agreement with the peak spacing data across the full range of temperatures. The fit uses the independently measured E_C , with the induced gap as a single fit parameter, yielding $\Delta^* = 190 \mu\text{eV}$, a reasonable value that lies between the two density of states features in Fig. 6.1(e). The island remains unpoisoned below $T_p \sim 250 \text{ mK}$.

6.4 COULOMB PEAK MOTION IN FIELD

The evolution of Coulomb blockade peaks with parallel magnetic field, B_{\parallel} , is shown in Fig. 6.4(a). In this data set, peaks show even-odd periodicity at zero field due to a gate-dependent gap or a bound state at energy E_0 less than E_C . A subgap state results in even-state spacing proportional to $E_C + E_0$ and odd-state spacing $E_C - E_0$ (see Appendix D), giving [61]

$$\begin{aligned} S_{E,O} &= \frac{1}{\eta e} [E_C \pm \min(E_C, E_0)] \\ &= \frac{S_E + S_O}{2} [1 \pm \min(1, E_0/E_C)] \end{aligned} \quad (6.2)$$

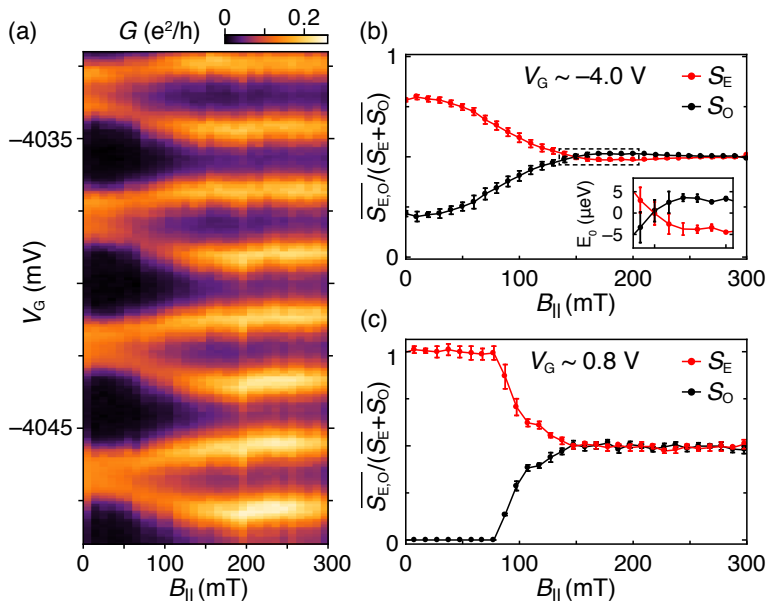


Fig. 6.4: (a) Conductance as a function of V_G and B_{\parallel} from device s2, taken at $V_G \sim -4.0$ V, shows even-odd peak spacings at zero field transit to $1e$ spacing when the field is increased. (b) Normalized even and odd Coulomb peak spacings, $\overline{S_{E,O}}/(\overline{S_E} + \overline{S_O})$, from the measurements shown in (a), as a function of B_{\parallel} . Inset: zoom-in of the peak spacing overshoot with amplitude of $7 \mu\text{eV}$ at $B_{\parallel} = 170$ mT. (c) Same as (b), but taken at $V_G \sim 0.8$ V. At positive gate voltage, the peaks become evenly spaced above $B_{\parallel} = 150$ mT. The error-bars in (a) and (b) were estimated using the standard deviation of the peak position.

Figure 6.4(b) shows the B_{\parallel} dependence of even and odd peak spacings, $\overline{S_{E,O}}/(\overline{S_E} + \overline{S_O})$, extracted from the data in Fig. 6.4(a), giving an effective g factor of ~ 13 . Even and odd peak spacings become equal at $B_{\parallel} = 150$ mT, then overshoot at higher fields with a maximum amplitude corresponding to $(7 \pm 1) \mu\text{eV}$. At more positive gate voltages [Fig. 6.4(c)], where the carrier density is higher, peaks are $2e$ -periodic at zero field, then transition through even-odd to $1e$ -periodic Coulomb blockade without an overshoot, with an effective g factor of ~ 31 .

Overshoot of peak spacing, with S_O exceeding S_E , indicates a discrete subgap state crossing zero energy [61, 165], consistent with interacting Majorana modes. The overshoot observed at more negative V_G is quantitatively in agreement with the overshoot seen in VLS wires of comparable length [61]. The absence of the overshoot and the increase of the g factor at positive V_G is consistent with the gate-tunable carrier density in VLS wires [51].

6.5 FIELD EFFECT MOBILITY

Conductance of a nanowire channel as a function of gate voltage is given by

$$G = \frac{\mu C}{l^2} (V_G - V_T), \quad (6.3)$$

where μ is the mobility, C is the capacitance between the gate electrode and the wire, l is the length of the channel, V_G is the gate voltage and V_T is the threshold voltage [166]. By introducing transconductance, dG/dV_G , the mobility can be expressed by

$$\mu = \frac{l^2}{C} \frac{dG}{dV_G}. \quad (6.4)$$

Conductance, $G_{DC} = I/V$, of device s3 (Fig. 6.5, inset) measured at ~ 4 K and $V_{DC} = 5$ mV as a function of top-gate voltage, V_G , is

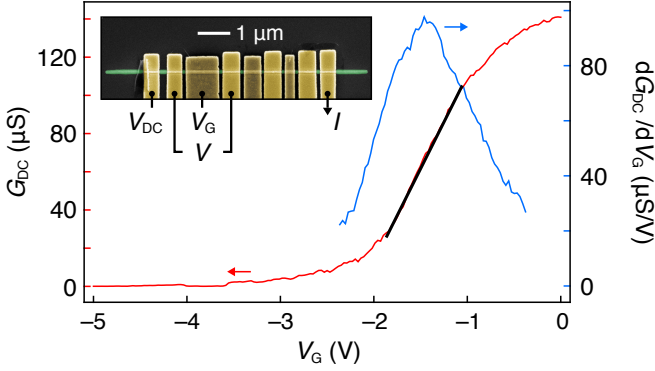


Fig. 6.5: Conductance, G_{DC} , (left axis) and transconductance, dG_{DC}/dV_G , (right axis) of device s3 as a function of gate voltage, V_G . The steepest slope extracted from the transconductance—indicated by the black line—yields field effect mobility $\mu = 700 \text{ cm}^2/(\text{V s})$. Inset: False-colored electron micrograph of device s3 overlaid with the measurement setup.

shown in Fig. 6.5. The transconductance peaks to $\sim 100 \mu\text{S}/\text{V}$ around $V_G = -1.5 \text{ V}$, corresponding to the highest change in conductance indicated by the black line. The nanowire length $l = 1 \mu\text{m}$ is set by the distance between the contacts. The capacitance $C = 1.5 \text{ fF}$ was estimated using finite element method simulation. Using Eq. (6.4) results in $\mu = 700 \text{ cm}^2/(\text{V s})$.

Measurements on a similar, chemical beam epitaxy grown SAG Hall bar with comparable mobility result in charge carrier density of $n \sim 9 \times 10^{17} \text{ cm}^{-3}$ [167]. The corresponding mean free path is

$$l_e = \frac{\hbar\mu}{e} (3\pi^2 n)^{1/3} \sim 15 \text{ nm}, \quad (6.5)$$

where \hbar is the reduced Planck constant and e is the elementary charge.

6.6 MINIMAL NETWORK

To demonstrate fabrication and operation of a simple SAG network, we investigate the coherence of electron transport in the loop structure (device s4) shown in Fig. 6.6(a), with the Al layer completely removed by wet etching. Conductance as a function of perpendicular magnetic field, B_{\perp} , shows a peak around zero magnetic field, characteristic of WAL [Fig. 6.6(b)]. A fit to a theoretical model for disordered quasi one-dimensional wires with strong spin-orbit coupling [168] yields electron phase-coherence length $l_{\phi}^{\text{WAL}} \sim 1.2 \mu\text{m}$, and spin-orbit length $l_{\text{SO}} \sim 0.4 \mu\text{m}$. We note that electrons propagating along [100] and [010] directions experience both Rashba and linear-Dresselhaus spin-orbit fields [169]. The magnitude of each field can be deduced from a combination of in-plane magnetic field angle and magnitude dependence of the conductance correction due to the weak (anti-) localization. Such study, however, is out of scope of this work.

Upon suppressing WAL with a large perpendicular field periodic conductance oscillations are observed [Fig. 6.6(c)] with period $\Delta B_{\perp} = 2.5 \text{ mT}$ corresponding to h/e AB oscillations with area of $1.7 \mu\text{m}^2$, matching the lithographic area of the loop. The oscillation amplitude, $A_{h/e}$, measured from the power spectral band around h/e [Fig. 6.6(d), inset] was observed to decrease with increasing temperature as seen in Fig. 6.6(d).

The size of $A_{h/e}$ is dictated by two characteristic lengths—thermal length, L_T , and phase-coherence length, l_{ϕ}^{AB} [168]. The thermal length is related to the energy averaging of conduction channels due to the finite electron temperature and is given by

$$L_T(T) = \sqrt{\hbar D / k_B T} \quad (6.6)$$

where D is the diffusion constant and k_B is the Boltzmann constant.

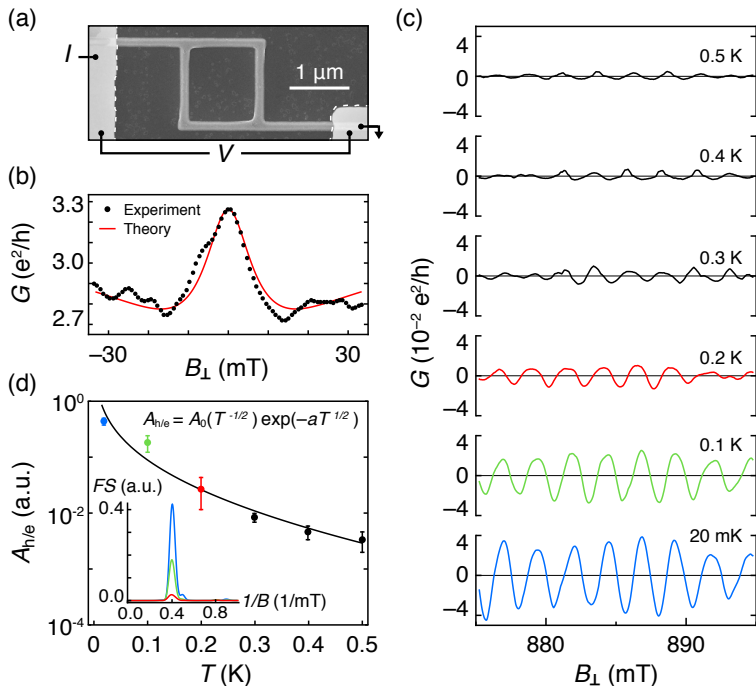


Fig. 6.6: (a) Electron micrograph of device s4 with false-colored epitaxial Al contacts (light gray) and overlaid 4-wire measurement setup. (b) Conductance, G , as a function B_{\perp} . Red curve is a theoretical magnetoconductance displaying the weak antilocalization effect in a system with spin-orbit length, $l_{SO} \sim 0.4 \mu\text{m}$, and phase-coherence length, $l_{\phi}^{\text{WAL}} \sim 1.2 \mu\text{m}$. (c) Aharonov-Bohm oscillations around $B_{\perp} \sim 900 \text{ mT}$ at different temperatures. (d) Amplitude of the h/e oscillations as a function of T . The exponential fit corresponds to the base-temperature phase-coherence length of $l_{\phi}^{\text{AB}} = 3.9 \mu\text{m}$. The error-bars correspond to the standard deviation between 4 data sets. Inset: Fourier spectra, FS , of the interference signal at 20 mK (blue), 100 mK (green) and 200 mK (red) from the measurements shown in (c).

The diffusion constant is given by

$$D = \frac{1}{3} v_F l_e \quad (6.7)$$

where $v_F = \hbar k_F / m^*$ is the Fermi velocity, with the Fermi wave vector $k_F = (3\pi^2 n)^{1/3}$ and the effective electron mass in InAs $m^* = 0.026 m_e$, yielding $D = 0.006 \text{ m}^2/\text{s}$, consistent with the values measured in vapor-liquid-solid (VLS) nanowires [170]. The resulting thermal length $L_T(20 \text{ mK}) = 1.5 \text{ }\mu\text{m}$ is comparable to the loop circumference $L = 5.2 \text{ }\mu\text{m}$ in device s4 [Fig. 6.6(a)]. As a result, energy averaging is expected to have finite contribution to the size of the conductance oscillations [168]. Taking $A_{h/e} \propto L_T(T) \exp[-L/l_\phi^{\text{AB}}(T)]$ with $L_T \propto T^{-1/2}$ and $l_\phi^{\text{AB}} \propto T^{-1/2}$ for a diffusive ring [171], a fit of the logarithmic amplitude $\log(A_{h/e}) = \log(A_0) - \frac{1}{2} \log T - a T^{1/2}$ yields $\log(A_0) \sim -1.5$ and $a \sim 6.7 \text{ K}^{-1/2}$ [Fig. 6.6(d)], giving a base-temperature phase-coherence length $l_\phi^{\text{AB}}(20 \text{ mK}) \sim 5.5 \text{ }\mu\text{m}$.

The discrepancy between the extracted l_ϕ^{WAL} and l_ϕ^{AB} has previously been observed in an experiment on GaAs/AlGaAs-based arrays of micron-sized loops [172]. It has been argued theoretically that WAL and AB interference processes are governed by different dephasing mechanisms [171]. As a result, l_ϕ^{WAL} and l_ϕ^{AB} have different temperature dependences.

6.7 SUMMARY

Our results show that selective area grown hybrid nanowires are a promising platform for scalable Majorana networks exhibiting a strong proximity effect. The hard induced superconducting gap and $2e$ -periodic Coulomb oscillations imply strongly suppressed quasiparticle poisoning. The overshoot of Coulomb peak spacing in a parallel magnetic field indicates the presence of a discrete low-energy state. Despite the relatively low charge carrier mobility,

the measured SAG-based network exhibits strong spin-orbit coupling and phase-coherent transport. Furthermore, the ability to design hybrid wire planar structures containing many branches and loops—a requirement for realizing topological quantum information processing—is readily achievable in SAG. Future work on SAG-based hybrid networks will focus on spectroscopy, correlations, interferometry, and manipulation of MZMs combining the ideas from both this and the preceding chapters.

MATERIALS & METHODS



A.1 NANOWIRE GROWTH

Hybrid nanowires used in this work were grown by molecular beam epitaxy on InAs (111)B substrate at 420 °C. The growth of both half- and full-shell wires was catalyzed by Au via the vapor-liquid-solid method. The nanowire growth was initiated with an axial growth of InAs along the [0001] direction with wurtzite crystal structure, using an In flux corresponding to a planar InAs growth rate of 0.5 $\mu\text{m/hr}$ and a calibrated As_4/In flux ratio of 14. The InAs nanowires were grown to a length of $\sim 10 \mu\text{m}$. The core diameter was tuned by changing the Au seed particle size. Subsequently, an Al shell was grown at $-30 \text{ }^\circ\text{C}$. The two- or three-facet shell was grown by properly aligning the growth substrate with respect to the Al source and keeping it fixed during the growth; the full-shell was grown on all six facets by continuously rotating the growth substrate with respect to the metal source. The shell thickness was controlled by the Al growth time. The resulting superconducting shell had an epitaxial, oxide-free interface with the semiconducting core [57].

A.2 FULL-SHELL DEVICE FABRICATION

Fabrication processes for both half-shell (Chapter 3) and full-shell (Chapters 4 and 5) devices were analogous. Without loss of generality, we describe the process for the full-shell wires.

The devices were fabricated on a degenerately n-doped Si substrate capped with a 200 nm thermal oxide. Prior to the wire deposition, the fabrication substrate was pre-fabricated with a set of alignment marks as well as bonding pads. Ti/Au (5/15 nm) bottom-gates for the devices discussed in Chapter 3 were fabricated using a single layer of A2 PMMA resists and capped with 10 nm atomic-layer-deposited HfO₂. Individual hybrid nanowires were transferred from the growth substrate onto the fabrication substrate using a manipulator station with a tungsten needle. Standard electron beam lithography techniques were used to pattern etching windows, contacts and gates.

The quality of the Al etching was found to improve when using a thin layer of AR 300-80 (new) adhesion promoter. Double layer of EL6 copolymer resists was used to define the etching windows. The Al was then selectively removed by submerging the fabrication substrate for ~70 s into MF-321 photoresist developer.

As the native InAs and Al oxides have different work functions, different cleaning processes had to be applied before contacting the wires. To contact the Al shell a stack of A4 and A6 PMMA resists was used. Normal Ti/Al (5/210 nm) ohmic contacts to Al shell were deposited after *in-situ* Ar-ion milling (RF ion source, 25 W, 18 mTorr, 9 min). To contact the InAs core, a single layer of A6 PMMA resist was used. A gentler Ar-ion milling (RF ion source, 15 W, 18 mTorr, 6.5 min) was used to clean the InAs core followed by metalization of the normal Ti/Al (5/180 nm) ohmic contacts to InAs core.

A single layer of A6 PMMA resist was used to form normal Ti/Al (5/150 nm) side-gate and top-gate electrodes, separated from the wire by ~8 nm layer of atomic layer deposited dielectric HfO₂.

A.3 SELECTIVE AREA GROWN SAMPLE PREPARATION

InAs nanowires with triangular cross-sections were selectively grown by MBE along the [100] and [010] directions on a semi-insulating (001) InP substrate with a pre-patterned (15 nm) SiO_x mask [155]. A thin (7 nm) layer of Al was grown *in-situ* at low temperatures on one facet by angled deposition, forming an epitaxial interface with InAs. For the fabrication of the devices, Al was selectively removed using electron-beam lithography and wet etch (Transene Al Etchant D, 50 °C, 10 s). Normal Ti/Al (5/120 nm) ohmic contacts were deposited after *in-situ* Ar milling (RF ion source, 15 W, 18 mTorr, 5 min). A film of HfO_2 (7 nm) was applied via atomic layer deposition at 90 °C before depositing Ti/Au (5/100 nm) gate electrodes.

A.4 MEASUREMENT SETUP

The measurements were carried out with a lock-in amplifier at frequencies $f_{ac} < 200$ Hz in a dilution refrigerator with a base temperature of $T_{base} \sim 20$ mK. Each of the dc lines used to measure and gate the devices was equipped with rf and rc filters (QDevil [173]), adding a line resistance $R_{Line} = 6.7$ k Ω . For voltage-bias differential conductance measurements, an ac signal with an amplitude of 0.1 V was applied to a sample through a homebuilt resistive voltage-divider (1 : 17.700), resulting in $V_{AC} \sim 5$ μ V excitation; the dc signal was enhanced by a factor of roughly (1 : 350). The current-bias differential resistance measurements were carried out using an ac excitation of $I_{ac} \sim 200$ nA for the full-shell wire measurements in Chapters 4 and 5, and $I_{ac} \sim 2$ nA for the selective-area-grown loop measurements in Chapter 6. The different I_{ac} excitations were chosen to account for different normal-state resistance of the samples.

COULOMB SPECTROSCOPY

B.1 HYBRIDIZATION AMPLITUDE

Coulomb peak spacing is dictated by the lowest energy state at energy E_0 , may it be a subgap state or the superconducting gap itself. The periodicity of the Coulomb peaks is determined by the ratio between E_0 and the charging energy, E_C . The Coulomb blockade is $2e$ periodic for $E_0 > E_C$; it becomes even-odd once E_0 is less than E_C ; and it is $1e$ periodic in case $E_0 = 0$. Non-interacting Majorana modes have zero energy, hence a Coulomb island hosting Majoranas can be charged in portions of single electrons. If the wavefunctions of the opposing Majorana modes have a finite overlap, for example because of the finite island length, the energy of the corresponding modes will deviate from zero [61, 92].

In the even-odd Coulomb blockade regime, the Coulomb-peak spacing, δV , is proportional to $E_C + E_0$ for even diamonds and $E_C - E_0$ for odd diamonds, which implies that $\delta V_E - \delta V_O \propto E_0$ (see Appendix D.2 and Refs. [61, 115]). This makes the Coulomb spectroscopy a powerful tool to study the interaction of Majorana modes in hybrid superconducting islands with finite size.

Device s2 discussed in Chapter 4 consists of six hybrid islands with lengths L ranging from 210 nm up to 970 nm. Figures 4.5 and 4.6 (Chapter 4) present measurements for the shortest island. The same

L (nm)	$\bar{\eta}$ (meV/V)	$\Delta\bar{\delta V}_{110}$ (mV)	A (μeV)
210	4.9	9.3	45
300	6.1	2.5	15
420	11	0.91	10
620	17	0.17	3
810	17	0.08	1.4
970	15	0.04	0.6

Table 3: Parameters for device f2 discussed in Chapter 4: L is the length of the island; $\bar{\eta}$ is the average lever arm extracted from slopes of the Coulomb diamonds measured at 110 mT; $\Delta(\bar{\delta V}_{110})$ are the differences of even and odd peak spacings measured at 110 mT; $A = \bar{\eta} \times \Delta\bar{\delta V}_{110}$ is the corresponding amplitude in energy.

measurement routine was carried out for all six islands at several different gate configurations to gather more statistics. The average lever arm, $\bar{\eta}$, the difference of average even and odd peak spacings $\Delta\bar{\delta V}_{110}$ as well as the corresponding amplitude $A = \bar{\eta} \times \Delta\bar{\delta V}_{110}$ —all measured at 110 mT, in the middle of the first lobe—are given in Table 3.

B.2 PEAK SPACING ANALYSIS

An exemplar routine of the peak spacing analysis is illustrated in Figs. B.1 and B.2 for data from device f2 [Fig. 4.5(a), Chapter 4] measured on the 810 nm Coulomb island. The peak positions and spacings are deduced from a multi-Lorentzian fit to the data. A sharp distinction between the destructive regime and the first lobe is found: while the peak spacing evolution with the plunger-gate voltage is featureless at 55 mT [Fig. B.1(a), blue line], a clear zigzag-like

alternating pattern between the adjacent spacings emerges at 110 mT [Fig. B.1(b), green line]. The destructive regime, where the Coulomb blockade is $1e$ periodic, provides a useful tool for calibrating the analysis and determining the experimental noise floor.

Conductance line shape of the Coulomb oscillations in the regime Γ (tunneling rate to the leads) $< k_B T$ (electron temperature) $< \delta$ (level spacing) $< E_C$ (charging energy) is given by [174]

$$F = A \cosh^{-2} [(p - V_G)/2w] \quad (\text{B.1})$$

where A is the amplitude of the peak, p is the peak position and w is the peak width parameter that is related to the electron temperature by $w = k_B T / \eta$, with the lever arm η . The full width at half maximum (FWHM) of the peak is given by $3.5 w$.

Figure B.1(c) shows three Coulomb peaks measured at 110 mT and fit to a linear combination of Eq. (B.1) with the parameter estimates and their standard errors given in Table 4. The average peak width $\bar{w} = (0.203 \pm 0.002)$ mV together with the lever arm $\eta = (17 \pm 1)$ meV/V, deduced from the Coulomb diamonds shown in Fig. B.2(b), yield electron temperature $T = (40 \pm 1)$ mK. Note that the effective electron temperature $w\eta/k_B$ is two orders of magnitude higher than the standard fit error of the peak-position estimate.

i	1	2	3
p_i (mV)	-115.524 ± 0.001	-105.931 ± 0.002	-96.397 ± 0.001
w_i (mV)	0.204 ± 0.001	0.198 ± 0.001	0.206 ± 0.001

Table 4: Peak index i , position p_i , and width parameter w_i , extracted by fitting Eq. (B.1) to the three-peaks data shown in Fig. B.1(c)

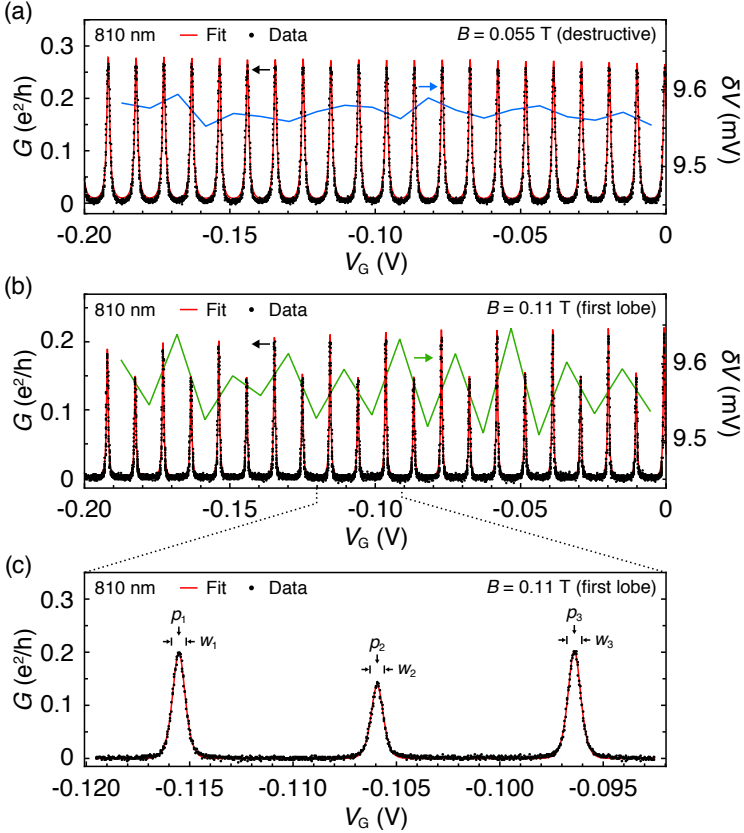


Fig. B.1: (a) Zero-bias conductance as a function of plunger gate voltage, V_G , for device f2 [Fig. 4.5(a), Chapter 4], measured on the 810 nm Coulomb island, over 20 Coulomb peaks in the destructive regime at $B = 55$ mT (black dots, left axis). The position of each peak is deduced from multi-Lorentzian fit (red line, left axis). The corresponding individual peak spacings (blue line, right axis) do not show any clear pattern—the peaks are $1e$ periodic. (b) Similar to (a) measured in the first lobe at $B = 110$ mT. Here, the peak spacings display a zigzag-like alternating pattern indicating even-odd periodicity. Note that the right-axes in (a) and (b) have the same scale. (c) Zoom-in on three peaks from (b), each consisting of ~ 25 data points over FWHM. The fit is described by Eq. (B.1), with the peak positions p_i and width parameters w_i given in Table 4. The FWHM of each peak given by $3.5 w$.

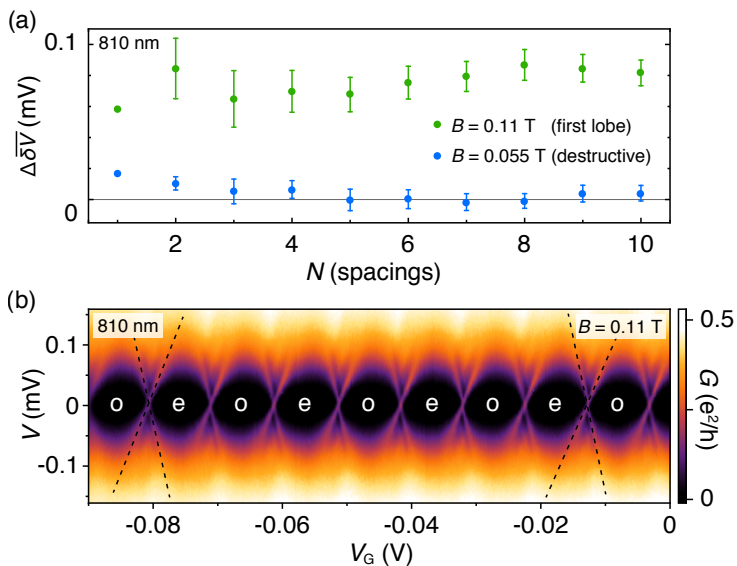


Fig. B.2: (a) Difference of the average even and odd peak spacings, $\Delta\overline{\delta V}$, as a function of number of the spacings taken to determine the average, N , measured at $B = 55$ mT (blue) and $B = 110$ mT (green), corresponding to the data in Figs. B.1(a) and B.1(b). The error bars illustrate the standard error of the mean given by σ/\sqrt{N} , where σ is the standard deviation of the spacings. Using $N = 10$ gives $\Delta\overline{\delta V}_{55} = (0.004 \pm 0.005)$ mV, which sets the experimental noise floor, and $\Delta\overline{\delta V}_{110} = (0.082 \pm 0.008)$ mV. (b) Tunneling conductance as a function of source-drain bias voltage, V , and gate voltage, V_G , measured at $B = 110$ mT, reveals nearly $1e$ -periodic Coulomb diamonds with even (e) and odd (o) valleys and discrete zero-bias peaks at the degeneracy points. The black, dashed lines illustrate the fits to the resonant energy levels used to infer the average lever arm, $\overline{\eta} = (17 \pm 1)$ meV/V, yielding electron temperature $T = (40 \pm 1)$ mK and $\Delta\overline{\delta V}_{110} = (1.4 \pm 0.2)$ μ eV for this data set.

ANOMALOUS PHASE

C.1 FULL-SHELL WIRE PARAMETERS

Full-shell wire parameters, including the ones use to compute the theory curves in Chapter 5, are summarized in Tables 5, 6 and 7. Note that the devices f1 and f2 (Chapter 4) are comprised of wire-type d2. The full-wire diameter, d_F , and the core diameter, d_C , [Fig. 5.1(a)] as well as the distance between the voltage probes, L , for each wire were measured from individual micrographs. For all the wires the Al oxide was assumed to be $t_{Ox} = 2$ nm. Using simple trigonometrical considerations one can deduce the full cross-sectional area $A_F = 3\sqrt{3}(d_F - 2t_{Ox})^2/8$, the shell thickness $t_S = \sqrt{3}(d_F - d_C)/4 - t_{Ox}$ and the mean wire diameter $d_M = (d_F - 2t_{Ox} + d_C)/2$. The normal state resistance R_N and the zero-field transition temperature T_{C0} were measured while cooling down the sample. Zero-field switching I_{S0} and re-trapping I_{R0} currents were measured at the base temperature. The period of the Little-Park oscillations in magnetic field can be calculated using $\Delta B = \Phi_0/A_M = 8\Phi_0/3\sqrt{3}d_M^2$. The shell resistivity is given by $\rho = R_N(A_F - A_C)/L$, where $A_C = 3\sqrt{3}d_C^2/2$ is the core cross-sectional area. The Drude mean free path for electrons in the shell is determined using $l_e = m_e v_F / e^2 n \rho$, with electron mass m_e , electron Fermi velocity in Al $v_F = 2.03 \times 10^6$ m/s [106], electron charge e and charge carrier density $n = k_F^3/3\pi^2$, where k_F is the

Wire	d_F (nm)	d_M (nm)	d_C (nm)	t_S (nm)	L (nm)
d1	157±5	146±4	137±5	7±3	945±5
d2	195±5	163±4	135±5	24±3	945±5
d3	340±5	288±4	240±5	41±3	920±5

Table 5: Wire dimensions measured from micrographs. Full-wire diameter d_F , mean diameter d_M , core diameter d_C , shell thickness t_S , and distance between the voltage probes L .

Wire	R_N (Ω)	T_{C0} (K)	Δ_0 (μeV)	I_{S0} (μA)	I_{R0} (μA)
d1	34.3±0.1	1.45±0.01	220±7	24±1	14±1
d2	1.6±0.1	1.22±0.01	183±3	62±2	46±2
d3	0.35±0.01	1.17±0.01	177±3	61±2	60±2

Table 6: Wire characteristics extracted from transport measurements. Normal-state resistance R_N , zero-field critical temperature T_{C0} , superconducting gap Δ_0 , zero-field switching current I_{S0} and re-trapping current I_{R0} .

Wire	ΔB (mT)	ρ (Ω nm)	l_e (nm)	ξ_S (nm)	λ (nm)
d1	150±7	110±40	4±1	71±8	200±60
d2	120±5	20±3	20 ±3	180±10	100±20
d3	38.4±0.9	14±1	29±2	224±8	89±7

Table 7: Calculated wire quantities. Flux period in magnetic field $\Delta B = \Phi_0/A_M$, resistivity ρ , mean free path l_e , zero-field superconducting coherence length ξ_S and Ginzburg-Landau penetration depth λ .

Fermi wave vector. The dirty-limit superconducting coherence length is given by [10] $\xi_S = \sqrt{\pi\hbar v_F l_e / 24k_B T_{C0}}$, where \hbar is the reduced Planck constant and k_B is the Boltzmann constant. For a dirty superconductor, the Ginzburg-Landau penetration depth is [10] $\lambda(T) = \lambda_L(T)\sqrt{\xi_0/1.33l_e}$, with the London penetration depth $\lambda_L(T) = \lambda_L(0)/\sqrt{2(1 - T/T_{C0})}$, and the coherence length is $\xi_S(T) = 0.855\sqrt{\xi_0 l_e / (1 - T/T_{C0})}$. This gives $\lambda = \lambda_L \xi_S / 1.39l_e$, with the zero-temperature London penetration depth $\lambda_L = 16$ nm [106].

C.2 DENSITY OF STATES

Some of the measured full-shell wires are equipped with tunneling S probes at ends [see Figs. 4.2(a) and 5.1(b)]. Applying voltage to the back-gate, V_{BG} , creates a tunnel barrier in the bare-semiconducting (InAs) segment, separating the normal-metal (Ti/Au) contact and the wire (Al/InAs). In the tunneling regime, the change in the current through the junction with the applied voltage bias corresponds to the local density of states (see Section 1.9). Differential tunnelling conductance, G , measured for all three wires (discussed in Chapter 5) as a function of source-drain voltage, V , is shown in Fig. C.1. For wire d1, with the thinnest shell, the measured superconducting gap is $\Delta_0 = 220$ μeV , whereas both wires d2 and d3 show a gap of around $\Delta_0 = 180$ μeV . All three gaps agree (within the experimental error) with the BCS theory predicted value $\Delta_0 = 1.764k_B T_{C0}$. Wires d1 and d2 display additional peaks in density of states at the energies below the main superconducting gap. We identify these with the proximity induced gaps inside the semiconducting cores.

C.3 NON-SATURATING RESISTANCE

Low-temperature saturation of the half-flux quantum R_S might rise a question whether it is not an artifact of a deficient cooling. In other words, if the electron temperature upon cooling would

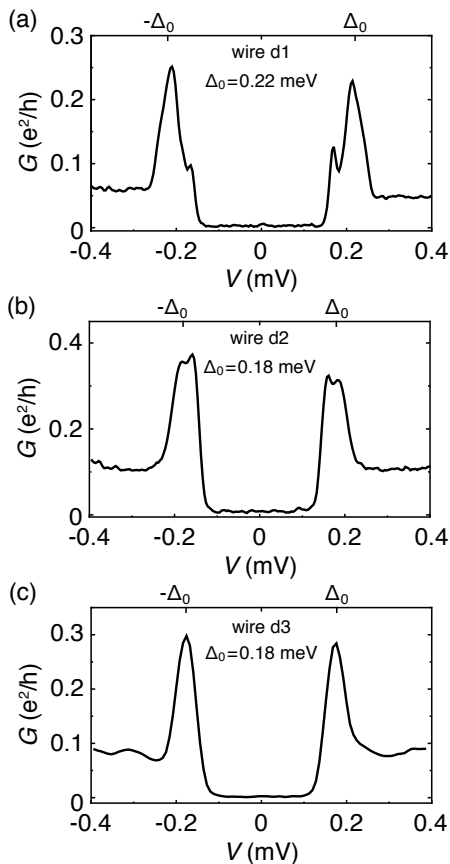


Fig. C.1: Differential conductance, G , as a function of source-drain voltage bias, V , measured for (a) wire d1, (b) wire d2, and (c) wire d3, discussed in Chapter 5.

saturate at some elevated temperature, so would the shell resistance. To rule out such an explanation for wire d3 (Chapter 5) we record

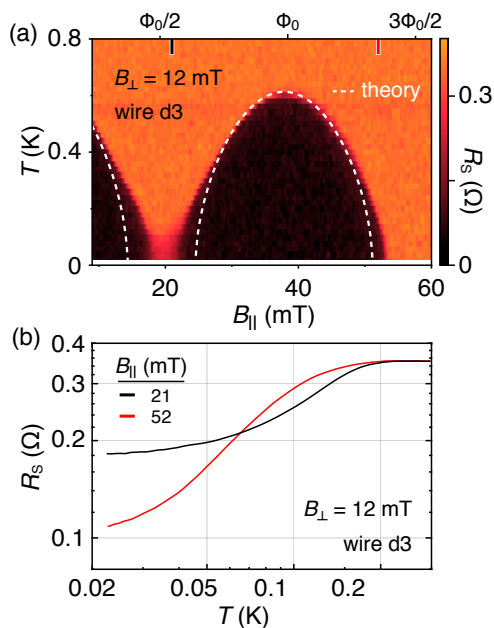


Fig. C.2: (a) Differential shell resistance, R_S , as a function of parallel magnetic field, B_{\parallel} , and temperature, T , measured for wire d3 at perpendicular magnetic field $B_{\perp} = 12$ mT. The theory curve is Eq. (5.1) (Chapter 5) computed with $\alpha = \alpha_{\parallel} + \alpha_{\perp}$ from Eqs (5.2) and (5.4). (b) R_S - T traces measured at $B_{\perp} = 12$ mT. At $B_{\parallel} = 21$ mT, close to $\Phi_0/2$ applied flux, R_S saturates at low temperatures. At $B_{\perp} = 52$ mT, before the wire enter the destructive regime around $3\Phi_0/2$, R_S shows temperature dependence even at the base temperature.

two R_S - T traces at $B_{\perp} = 12$ mT (Fig. C.2): one at $B_{\parallel} = 21$ mT, close to $\Phi_0/2$ applied flux quantum, displaying the anomalous R_S saturation; another at $B_{\parallel} = 52$ mT, before the destructive regime around $3\Phi_0/2$, with a T -dependent R_S down to the base temperature. Furthermore, the data in Fig. 5.7(a) (Chapter 5) shows that the R_S starts to saturate

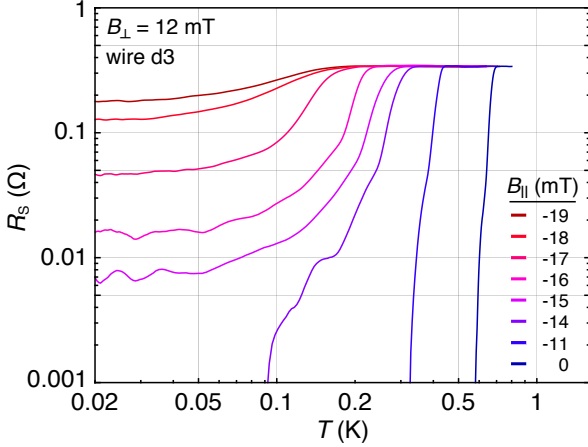


Fig. C.3: Differential shell resistance, R_S as a function of T measured at fixed $B_{\perp} = 12$ mT for wire d3 at different B_{\parallel} values. Around $B_{\parallel} = 0$, as T is lowered, the sample displays a conventional normal-superconducting phase transition. As the field is tuned to $B_{\parallel} = -14$ mT the shell resistance starts to saturate at low T to a finite, B_{\parallel} -dependent value.

at different temperatures for different B_{\perp} . Finally, it is unlikely for a poor electron cooling to cause the observed broadening of the anomalous phase in flux, see the main-text Fig. 5.6(b) and 5.6(c) (Chapter 5), as well as Fig. C.2(a).

C.4 FLUX-DEPENDENT RESISTANCE SATURATION

The data shown in Figs. 5.6 and 5.7 (Chapter 5) demonstrate that at a fixed $B_{\parallel} = -19$ mT (around $-\Phi_0/2$ of the applied flux) R_S for wire d3 saturates at low T to a B_{\perp} -dependent value. We observe a qualitatively similar B_{\parallel} -dependent anomalous saturation of R_S at a fixed $B_{\perp} = 12$ mT (Fig. C.3).

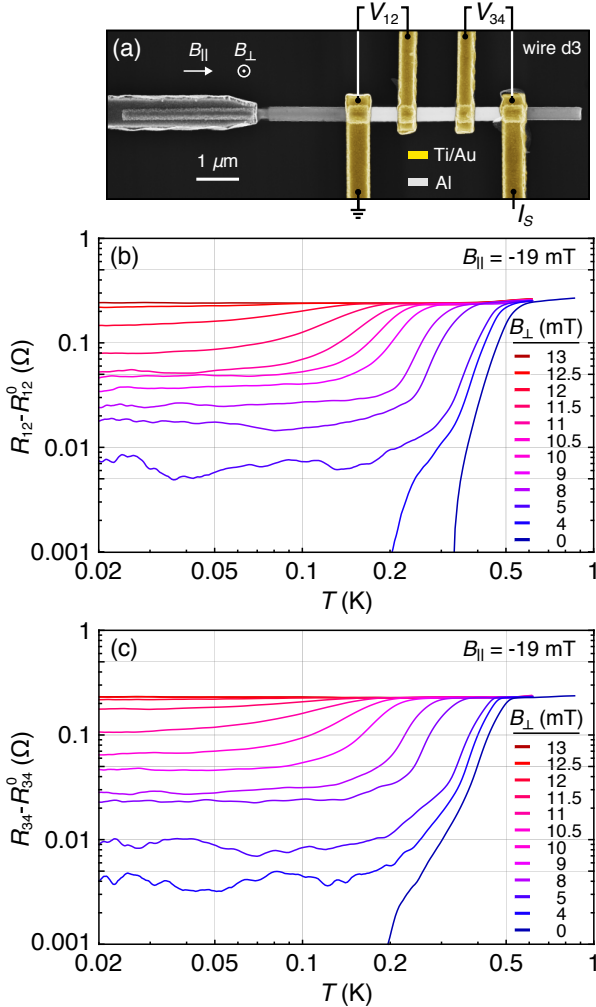


Fig. C.4: (a) Micrograph of wire d3 with the highlighted three-terminal setups for the outer segments shell resistance measurements. (b) Differential shell resistance in the left-most wire d3 segment, $R_{12} = dV_{12}/dI_S$ (with the subtracted contact resistance R_{12}^0) measured as a function of temperature T at $B_{\parallel} = -19$ mT and different B_{\perp} values. (c) Similar to (b) but measured for the right-most segment. The contact resistances R_{12}^0 and R_{34}^0 were measured around the base temperature at $B_{\perp} = 0$ and $B_{\parallel} = -19$ mT.

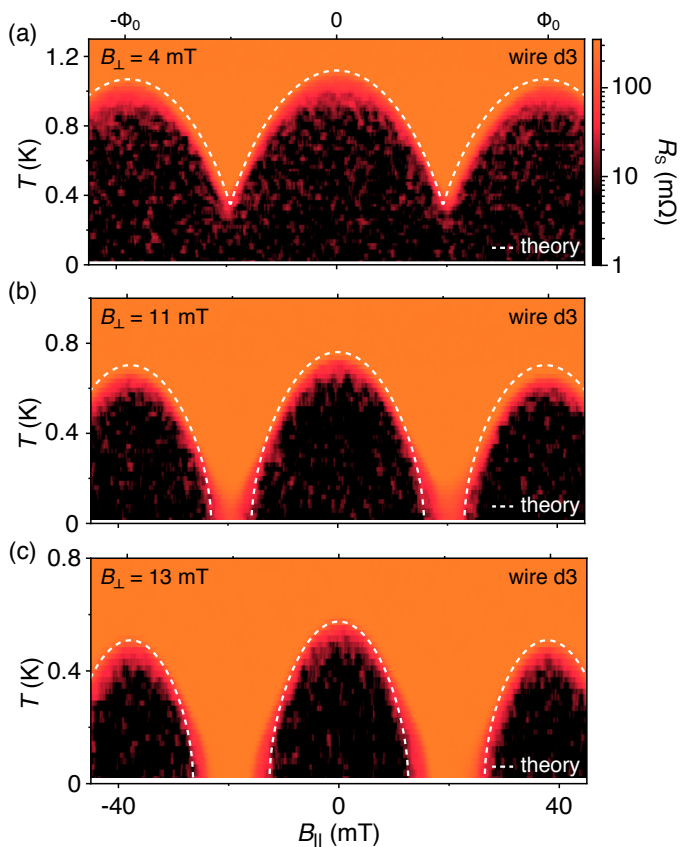


Fig. C.5: Same data as in Figs. 5.6(a), 5.6(b) and 5.6(c) (Chapter 5) but in logarithmic color scale highlighting the low-resistance features. At low T , the anomalous phase is present predominantly above the T_C predicted by the mean-field theory. The finite resistance at higher temperatures, below the arcs of the theory curves, arise presumably due to thermal fluctuations.

C.5 OUTER SEGMENTS

To demonstrate that the anomalous resistance saturation shown in Fig. 5.7(a) (Chapter 5) is not due to a local disorder in the middle-wire segment, we investigate the outer two wire segments of wire d3 using three-terminal setup, see Fig. C.4(a). Differential shell resistances $R_{12} = dV_{12}/dI_S$ and $R_{34} = dV_{34}/dI_S$ with the subtracted corresponding contact resistances measured as a function of T at $B_{\parallel} = -19$ mT and different B_{\perp} values are shown in Figs. C.4(b) and C.4(c). The contacts resistances R_{12}^0 and R_{34}^0 were measured around the base temperature at $B_{\perp} = 0$ and $B_{\parallel} = -19$ mT. The observed B_{\perp} -dependent, low-temperature anomalous shell resistances are qualitatively similar to the R_S of the middle segment. The small quantitative discrepancies between the segments might arise due to the uncertainty in the applied B_{\perp} or a small wire tapering.

C.6 ANOMALOUS PHASE VS. MEAN-FIELD THEORY

Figure C.5 shows the same data as in Figs. 5.6(a)–5.6(c) (Chapter 5), but plotted in a logarithmic color scale to highlight the low-resistance features. It appears that the anomalous resistance phase at low T develops predominantly above the mean-field theory predicted T_C , close to the $\pm\Phi_0/2$ of the applied flux. At elevated T , the wire shows finite, but reduced R_S around 0 and $\pm\Phi_0$ of the applied flux, presumably arising due to thermal fluctuations.

COULOMB BLOCKADE

D

D.1 FREE ENERGY MODEL

Theoretical fit in Fig. 6.3(c) (Chapter 6) is based on a free energy model given by Eq. (6.1), where the difference in free energy between odd and even occupied states is given by

$$F(T) = k_B T \ln \left[\frac{(1 + e^{-\Delta^*/k_B T})^{N_{\text{eff}}} + (1 - e^{-\Delta^*/k_B T})^{N_{\text{eff}}}}{(1 + e^{-\Delta^*/k_B T})^{N_{\text{eff}}} - (1 - e^{-\Delta^*/k_B T})^{N_{\text{eff}}}} \right] \quad (\text{D.1})$$

with the effective number of continuum states $N_{\text{eff}} = 2V_{\text{Al}}\rho_{\text{Al}}\sqrt{2\Delta^*k_B T}$, where V_{Al} is the volume of the island and ρ_{Al} is the density of states at the Fermi energy [163]. The fit was obtained by using $V_{\text{Al}} = 2.2 \times 10^{-6} \text{ nm}^3$, consistent with Fig. 6.3(b) (Chapter 6), electron density of states $\rho_{\text{Al}} = 23 \text{ eV}^{-1} \text{ nm}^{-3}$ [163] and $E_C = 60 \text{ meV}$, measured from Coulomb diamonds (Fig. D.1), with Δ^* as the single fit parameter.

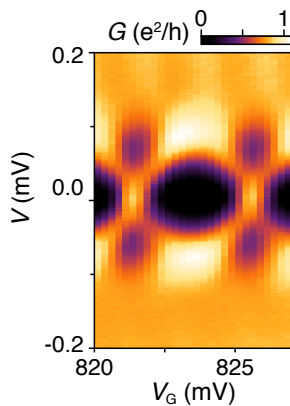


Fig. D.1: Differential conductance, G , of device s2 (Chapter 6) as a function of source-drain bias, V , and gate voltage, V_G at zero magnetic field, showing a Coulomb diamond with $2E_C = 120 \mu\text{eV}$.

D.2 DEVICE ENERGY

Energy, E , of a Coulomb blockaded device with electron occupancy, n , as a function of normalized gate voltage, N , can be defined as

$$E(N) = E_C(n - N)^2 + FN_0 \quad (\text{D.2})$$

where E_C is the charging energy, F is the relative free energy and $N_0 = 0$ (1) for even (odd) parity of the device, see Fig. 6.3(c), inset (Chapter 6). Charge degeneracy points can be extracted using Eq. (D.2), from which we can deduce the normalized even and odd peak spacings in units of charge, e , as

$$N_{E,O} = 1 \pm F/E_C \quad (\text{D.3})$$

The even and odd peak spacing difference in gate voltage is given by

$$S_E - S_O = \frac{E_C}{e\eta}(N_E - N_O), \quad (\text{D.4})$$

with the dimensionless lever arm $\eta = E_C/eS$.

Note that in the limit of zero temperature, F is defined by the size of the induced gap, Δ^* , or, if present, by the energy of a subgap state, E_0 .

PUBLICATIONS

- 1 | **S. Vaitiekėnas**, G. W. Winkler, B. van Heck, T. Karzig, M.-T. Deng, K. Flensberg, L. I. Glazman, C. Nayak, P. Krogstrup, R. M. Lutchyn, and C. M. Marcus, *Flux-induced topological superconductivity in full-shell nanowires*, Science **367**, 1442 (2020).
- 2 | **S Vaitiekėnas**, P. Krogstrup, and C. M. Marcus, *Anomalous metallic phase in tunable destructive superconductors*, Phys. Rev. B **101**, 060507(R) (2020).
- 3 | M. H. Freedman, B. van Heck, G. W. Winkler, T. Karzig, R. Lutchyn, P. Krogstrup, C. Nayak, C. M. Marcus, and **S Vaitiekėnas**, *Form and fabrication of semiconductor-superconductor nanowires and quantum devices based thereon*, US Patent Applications 20200027030 & 20200027971 (2020).
- 4 | Y. Liu, **S Vaitiekėnas**, S. Marti-Sanchez, C. Koch, S. Hart, Z. Cui, T. Kanne, S. A. Khan, R. Tanta, S. Upadhyay, M. Espineira Cachaza, C. M. Marcus, J. Arbiol, K. A. Moler, and P. Krogstrup, *Semiconductor - ferromagnetic insulator - superconductor nanowires: stray field and exchange field*, Nano Lett. **20**, 456 (2020).

- 5| **S. Vaitiekėnas**, A. M. Whiticar, M.-T. Deng, F. Krizek, J. E. Sestoft, C. J. Palmstrøm, S. Marti-Sanchez, J. Arbiol, P. Krogstrup, L. Casparis, and C. M. Marcus, *Selective-area-grown semiconductor-superconductor hybrids: a basis for topological networks*, Phys. Rev. Lett. **121**, 147701 (2018).
- 6| F. Krizek, J. E. Sestoft, P. Aseev, S. Marti-Sanchez, **S. Vaitiekėnas**, L. Casparis, S. A. Khan, Y. Liu, T. Stankevič, A. M. Whiticar, A. Fursina, F. Boekhout, R. Koops, E. Uccelli, L. P. Kouwenhoven, C. M. Marcus, J. Arbiol, and P. Krogstrup, *Field effect enhancement in buffered quantum nanowire networks*, Phys. Rev. Mater. **2**, 093401 (2018).
- 7| M.-T. Deng*, **S. Vaitiekėnas***, E. Prada, P. San-Jose, J. Nygård, P. Krogstrup, R. Aguado, and C. M. Marcus, *Nonlocality of Majorana modes in hybrid nanowires*, Phys. Rev. B **98**, 085125 (2018).
- 8| **S. Vaitiekėnas***, M.-T. Deng*, J. Nygård, P. Krogstrup, and C. M. Marcus, *Effective g factor of subgap states in hybrid nanowires*, Phys. Rev. Lett. **121**, 037703 (2018).
- 9| E. M. Spanton, M.-T. Deng, **S. Vaitiekėnas**, P. Krogstrup, J. Nygård, C. M. Marcus, and K. A. Moler, *Current-phase relations of few-mode InAs nanowire Josephson junctions*, Nat. Phys. **13** (12), 1177 (2017).
- 10| M.-T. Deng, **S. Vaitiekėnas**, E. B. Hansen, J. Danon, M. Leijnse, K. Flensberg, J. Nygård, P. Krogstrup, and C. M. Marcus, *Majorana bound state in a coupled quantum-dot hybrid-nanowire system*, Science **354**, 1557 (2016).

* Equal contribution

REFERENCES

- [1] H. Kamerlingh Onnes, *Further experiments with liquid helium. C. On the change of electric resistance of pure metals at very low temperatures, etc. IV. The resistance of pure mercury at helium temperatures*, Comm. Phys. Lab. Univ. Leiden **120b**, (1911).
- [2] L. D. Landau, *The Theory of a Fermi Liquid*, Zh. Eksp. Teor. Fiz. **30**, 1058 (1956); Soviet Phys. JETP **3**, 920 (1956).
- [3] E. Maxwell, *Isotope Effect in the Superconductivity of Mercury*, Phys. Rev. **78**, 477 (1950).
- [4] C. A. Reynolds, B. Serin, W. H. Wright, and L. B. Nesbitt, *Superconductivity of Isotopes of Mercury*, Phys. Rev. **78**, 487 (1950).
- [5] J. Bardeen, *Zero-Point Vibrations and Superconductivity*, Phys. Rev. **79**, 167 (1950); *Wave Functions for Superconducting Electrons*, Phys. Rev. **80**, 567 (1950); *Relation between Lattice Vibration and London Theories of Superconductivity*, Phys. Rev. **81**, 829 (1951); *Electron-Vibration Interactions and Superconductivity*, Rev. Mod. Phys. **23**, 261 (1951).
- [6] L. N. Cooper, *Bound Electron Pairs in a Degenerate Fermi Gas*, Phys. Rev. **104**, 1189 (1956).

- [7] J. Bardeen, L. N. Cooper, and J. R. Schrieffer, *Microscopic Theory of Superconductivity*, Phys. Rev. **106**, 162 (1957); *Theory of Superconductivity*, Phys. Rev. **108**, 1175 (1957).
- [8] P. G. de Gennes, *Superconductivity Of Metals And Alloys*, New York: Benjamin (1993).
- [9] A. B. Pippard, *An experimental and theoretical study of the relation between magnetic field and current in a superconductor*, Proc. Roy. Soc. (London) **A216**, 547 (1953).
- [10] M. Tinkham, *Introduction to Superconductivity*, New York: McGraw Hill, ed. 2 (1996).
- [11] V. L. Ginzburg and L. D. Landau, *On the Theory of superconductivity*, Zh. Eksp. Teor. Fiz. **20**, 1064 (1950).
- [12] L. P. Gor'kov, *Microscopic Derivation of the Ginzburg-Landau Equations in the Theory of Superconductivity*, Zh. Eksp. Teor. Fiz. **36**, 1918 (1959); Soviet Phys. JETP **9**, 1364 (1959).
- [13] T. P. Orlando and K. A. Delin, *Foundations of Applied Superconductivity*, Addison-Wesley (1991).
- [14] F. London and H. London, *The Electromagnetic Equations of the Supraconductor*, Proc. Roy. Soc. (London) **A149**, 71 (1935).
- [15] W. Meissner and R. Ochsenfeld, *Ein neuer Effekt bei eintritt der Supraleitfähigkeit*, Naturwiss. **21**, 787 (1933).
- [16] F. London, *Superfluids*, New York: John Wiley & Sons, Inc. (1950).
- [17] W. A. Little and R. D. Parks, *Observation of quantum periodicity in the transition temperature of a superconducting cylinder*, Phys. Rev. Lett. **9**, 9 (1962).

- [18] A. F. Andreev, *Thermal conductivity of the intermediate state of superconductors*, Sov. Phys. JETP **19**, 1228 (1964).
- [19] G. E. Blonder, M. Tinkham, and T. M. Klapwijk, *Transition from metallic to tunneling regimes in superconducting microconstrictions: Excess current, charge imbalance, and supercurrent conversion*, Phys. Rev. B **25**, 4515 (1982).
- [20] F. Dolcini, *Andreev Reflection*, Heidelberg: Lecture Notes (2009).
- [21] R. Landauer, *Spatial Variation of Currents and Fields Due to Localized Scatterers in Metallic Conduction*, IBM J. Res. Dev. **1**, 223 (1957).
- [22] Y. V. Nazarov and Y. M. Blanter, *Quantum Transport. Introduction to Nanoscience*, Cambridge University Press (2009).
- [23] E. Majorana, *Teoria simmetrica dell'elettrone e del positrone, (A symmetric theory of electrons and positrons)*, Nuovo Cim. **14**, 171 (1937).
- [24] N. Read and D. Green, *Paired states of fermions in two dimensions with breaking of parity and time-reversal symmetries and the fractional quantum Hall effect*, Phys. Rev. B **61**, 10267 (2000).
- [25] C. Nayak, S. H. Simon, A. Stern, M. Freedman, and S. Das Sarma, *Non-Abelian anyons and topological quantum computation*, Rev. Mod. Phys. **80**, 1083 (2008).
- [26] M. Sato and Y. Ando, *Topological superconductors: a review*, Rep. Prog. Phys. **80**, 076501 (2017).
- [27] S. Das Sarma, M. Freedman, and C. Nayak, *Majorana zero modes and topological quantum computation*, Npj Quantum Inf. **1**, 15001 (2015).

- [28] P. A. M. Dirac, *The quantum theory of the electron*, Proc. R. Soc. Lond. A **117**, 610 (1928).
- [29] C. D. Anderson, *The positive electron*, Phys. Rev. **43**, 491 (1933).
- [30] F. Wilczek, *Majorana returns*, Nat. Phys. **5**, 614 (2009).
- [31] N. N. Bogolyubov, *A New Method in the Theory of Superconductivity. I*, Sov. Phys. JETP **34**, 41 (1958).
- [32] A. Abrikosov, *On the Magnetic Properties of Superconductors of the Second Group*, Sov. Phys. JETP **5**, 1174 (1957).
- [33] A. Y. Kitaev, *Unpaired Majorana fermions in quantum wires*, Usp. Fiz. Nauk., **171**, 131 (2001).
- [34] J. Alicea, *New directions in the pursuit of Majorana fermions in solid state systems*, Rep. Prog. Phys. **75**, 076501 (2012).
- [35] J. M. Leinaas and J. Myrheim, *On the theory of identical particles*, Nuovo Cim. **37**, 1 (1977).
- [36] D. Arovas, J. R. Schrieffer, and F. Wilczek, *Fractional Statistics and the Quantum Hall Effect*, Phys. Rev. Lett. **53**, 722 (1984).
- [37] D. A. Ivanov, *Non-Abelian statistics of half-quantum vortices in p -wave superconductors*, Phys. Rev. Lett. **86**, 268 (2001).
- [38] A. Y. Kitaev, *Fault-tolerant quantum computation by anyons*, Ann. Phys. **303**, 2 (2003).
- [39] T. Karzig, C. Knapp, R. M. Lutchyn, P. Bonderson, M. B. Hastings, C. Nayak, J. Alicea, K. Flensberg, S. Plugge, Y. Oreg, C. M. Marcus, and M. H. Freedman, *Scalable designs for quasiparticle-poisoning-protected topological quantum computation with Majorana zero modes*, Phys. Rev. B **95**, 235305 (2017).

- [40] G. Moore and N. Read, *Nonabelions in the fractional quantum hall effect*, Nucl. Phys. B **360**, 362 (1991).
- [41] A. Stern, *Non-Abelian states of matter*, Nature **464**, 187 (2010).
- [42] L. Fu and C. L. Kane, *Superconducting Proximity Effect and Majorana Fermions at the Surface of a Topological Insulator*, Phys. Rev. Lett. **100**, 096407 (2008).
- [43] M. Leijnse and K. Flensberg, *Introduction to topological superconductivity and Majorana fermions*, Semicond. Sci. Technol. **27**, 124003 (2012).
- [44] R. M. Lutchyn, J. D. Sau, and S. D. Sarma, *Majorana Fermions and a Topological Phase Transition in Semiconductor-Superconductor Heterostructures*, Phys. Rev. Lett. **105**, 077001 (2010).
- [45] Y. Oreg, G. Rafael, and F. von Oppen, *Helical Liquids and Majorana Bound States in Quantum Wires*, Phys. Rev. Lett. **105**, 177002 (2010).
- [46] E. I. Rashba, *Symmetry of bands in wurzite-type crystals. 1. Symmetry of bands disregarding spin-orbit interaction*, Sov. Phys. Solid. State, **1**, 368 (1959).
- [47] T. D. Stanescu, *Introduction to Topological Quantum Matter & Quantum Computation*, Boca Raton: CRC Press (2017).
- [48] B. Nijholt and A. R. Akhmerov, *Orbital effect of magnetic field on the Majorana phase diagram*, Phys. Rev. B **93**, 235434 (2016).
- [49] O. Dmytruk and J. Klinovaja, *Suppression of the overlap between Majorana fermions by orbital magnetic effects in semiconducting-superconducting nanowires*, Phys. Rev. B **97**, 15540 (2018).
- [50] R. M. Lutchyn, G. W. Winkler, B. van Heck, T. Karzig, K. Flensberg, L. Glazman, and C. Nayak, arXiv:1809.05512 (2018).

- [51] S. Vaitiekėnas, M.-T. Deng, J. Nygård, P. Krogstrup, and C. M. Marcus, *Effective g Factor of Subgap States in Hybrid Nanowires*, Phys. Rev. Lett. **121**, 037703 (2018).
- [52] J. Alicea, Y. Oreg, G. Refael, F. von Oppen, and M. P. A. Fisher, *Non-Abelian statistics and topological quantum information processing in 1D wire networks*, Nat. Phys. **7**, 412 (2011).
- [53] D. Aasen, M. Hell, R. V. Mishmash, A. Higginbotham, J. Danon, M. Leijnse, T. S. Jespersen, J. A. Folk, C. M. Marcus, K. Flensberg, and J. Alicea, *Milestones Toward Majorana-Based Quantum Computing*, Phys. Rev. X **6**, 031016 (2016).
- [54] V. Mourik, K. Zuo, S. M. Frolov, S. R. Plissard, E. P. A. M. Bakkers, and L. P. Kouwenhoven, *Signatures of Majorana Fermions in Hybrid Superconductor-Semiconductor Nanowire Devices*, Science **336**, 1003 (2012).
- [55] A. Das, Y. Ronen, Y. Most, Y. Oreg, M. Heiblum, and H. Shtrikman, *Zero-bias peaks and splitting in an Al-InAs nanowire topological superconductor as a signature of Majorana fermions*, Nat. Phys. **8**, 887 (2012).
- [56] Ö. Gül, H. Zhang, J. D. S. Bommer, M. W. A. de Moor, D. Car, S. R. Plissard, E. P. A. M. Bakkers, A. Geresdi, K. Watanabe, T. Taniguchi, and L. P. Kouwenhoven, *Ballistic Majorana nanowire devices*, Nat. Nanotechnol. **13**, 192 (2018).
- [57] P. Krogstrup, N. L. B. Ziino, W. Chang, S. M. Albrecht, M. H. Madsen, E. Johnson, J. Nygård, C. M. Marcus, and T. S. Jespersen, *Epitaxy of semiconductor-superconductor nanowires*, Nat. Mater. **14**, 400 (2015).
- [58] W. Chang, S. M. Albrecht, T. S. Jespersen, F. Kuemmeth, P. Krogstrup, J. Nygård, and C. M. Marcus, *Hard gap in epitaxial*

- semiconductor-superconductor nanowires*, Nat. Nanotechnol. **10**, 232 (2015).
- [59] M.-T. Deng, S. Vaitiekėnas, E. B. Hansen, J. Danon, M. Leijnse, K. Flensberg, J. Nygård, P. Krogstrup, and C. M. Marcus, *Majorana bound state in a coupled quantum-dot hybrid-nanowire system*, Science **354**, 1557 (2016).
- [60] H. Zhang, C.-X. Liu, S. Gazibegovic, D. Xu, J. A. Logan, G. Wang, N. van Loo, J. D. S. Bommer, M. W. A. de Moor, D. Car, R. L. M. Op het Veld, P. J. van Veldhoven, S. Koelling, M. A. Verheijen, M. Pendharkar, D. J. Pennachio, B. Shojaei, J. S. Lee, C. J. Palmstrøm, E. P. A. M. Bakkers, S. Das Sarma, and L. P. Kouwenhoven, *Quantized Majorana conductance*, Nature, **556**, 74 (2018).
- [61] S. M. Albrecht, A. P. Higginbotham, M. Madsen, F. Kuemmeth, T. S. Jespersen, J. Nygård, P. Krogstrup, and C. M. Marcus, *Exponential protection of zero modes in Majorana islands*, Nature **531**, 206 (2016).
- [62] C. R. Pidgeon, D. L. Mitchell, and R. N. Brown, *Interband Magnetoabsorption in InAs and InSb*, Phys. Rev. **154**, 737 (1967).
- [63] J. Konopka, *Conduction electron spin resonance in InAs*, Phys. Lett. A **26**, 29 (1967).
- [64] E. J. H. Lee, X. Jiang, M. Houzet, R. Aguado, C. M. Lieber, and S. De Franceschi, *Spin-resolved Andreev levels and parity crossings in hybrid superconductor-semiconductor nanostructures*, Nat. Nanotechnol. **9**, 79 (2014).
- [65] S. Csonka, L. Hofstetter, F. Freitag, S. Oberholzer, C. Schönenberger, T. S. Jespersen, M. Aagesen, and J. Nygård, *Giant Fluctuations and Gate Control of the g-Factor in InAs Nanowire Quantum Dots*, Nano Lett. **8**, 3932 (2008).

- [66] M. D. Schroer, K. D. Petersson, M. Jung, and J. R. Petta, *Field Tuning the g Factor in InAs Nanowire Double Quantum Dots*, Phys. Rev. Lett. **107**, 176811 (2011).
- [67] G. Lommer, F. Malcher, and U. Rössler, *Reduced g factor of subband Landau levels in AlGaAs/GaAs heterostructures*, Phys. Rev. B **32**, 6965(R) (1985).
- [68] A. A. Kiselev, E. L. Ivchenko, and U. Rössler, *Electron g factor in one- and zero-dimensional semiconductor nanostructures*, Phys. Rev. B **58**, 16353 (1998).
- [69] M. T. Björk, A. Fuhrer, A. E. Hansen, M. W. Larsson, L. E. Fröberg, and L. Samuelson, *Tunable effective g factor in InAs nanowire quantum dots*, Phys. Rev. B **72**, 201307(R) (2005).
- [70] G. W. Winkler, D. Varjas, R. Skolasinski, A. A. Soluyanov, M. Troyer, and M. Wimmer, *Orbital Contributions to the Electron g Factor in Semiconductor Nanowires*, Phys. Rev. Lett. **119**, 037701 (2017).
- [71] G. Salis, Y. Kato, K. Ensslin, D. C. Driscoll, A. C. Gossard, and D. D. Awschalom, *Electrical control of spin coherence in semiconductor nanostructures*, Nature **414**, 619 (2001).
- [72] A. E. G. Mikkelsen, P. Kotetes, P. Krogstrup, and K. Flensberg, *Hybridization at Superconductor-Semiconductor Interfaces*, Phys. Rev. X **8**, 031040 (2018).
- [73] A. E. Antipov, A. Bargerbos, G. W. Winkler, B. Bauer, E. Rossi, and R. M. Lutchyn, *Effects of Gate-Induced Electric Fields on Semiconductor Majorana Nanowires*, Phys. Rev. X **8**, 031041 (2018).
- [74] T. D. Stanescu, S. Tewari, J. D. Sau, and S. Das Sarma, *To Close or Not to Close: The Fate of the Superconducting Gap Across*

- the Topological Quantum Phase Transition in Majorana-Carrying Semiconductor Nanowires*, Phys. Rev. Lett. **109**, 266402 (2012).
- [75] D. Chevallier, P. Simon, and C. Bena, *From Andreev bound states to Majorana fermions in topological wires on superconducting substrates: A story of mutation*, Phys. Rev. B **88**, 165401 (2013).
- [76] D. Rainis, L. Trifunovic, J. Klinovaja, and D. Loss, *Towards a realistic transport modeling in a superconducting nanowire with Majorana fermions*, Phys. Rev. B **87**, 024515 (2013).
- [77] R. V. Mishmash, D. Aasen, A. P. Higginbotham, and J. Alicea, *Approaching a topological phase transition in Majorana nanowires*, Phys. Rev. B **93**, 245404 (2016).
- [78] C.-X. Liu, J. D. Sau, T. D. Stanescu, and S. Das Sarma, *Andreev bound states versus Majorana bound states in quantum dot-nanowire-superconductor hybrid structures: Trivial versus topological zero-bias conductance peaks*, Phys. Rev. B **96**, 075161 (2017).
- [79] C. Moore, T. D. Stanescu, S. Tewari, *Two-terminal charge tunneling: Disentangling Majorana zero modes from partially separated Andreev bound states in semiconductor-superconductor heterostructures*, Phys. Rev. B **97**, 165302 (2017).
- [80] M.-T. Deng, S. Vaitiekėnas, E. Prada, P. San-Jose, J. Nygård, P. Krogstrup, R. Aguado, and C. M. Marcus, *Nonlocality of Majorana modes in hybrid nanowires*, Phys. Rev. B **98**, 085125 (2018).
- [81] C. Reeg, D. Loss, and J. Klinovaja, *Metallization of a Rashba wire by a superconducting layer in the strong-proximity regime*, Phys. Rev. B **97**, 165425 (2018).
- [82] S. Vaitiekėnas, M.-T. Deng, P. Krogstrup, and C. M. Marcus, *Flux-induced Majorana modes in full-shell nanowires*, arXiv:1809.05513 (2018).

- [83] S. Vaitiekėnas, G. W. Winkler, B. van Heck, T. Karzig, M.-T. Deng, K. Flensberg, L. I. Glazman, C. Nayak, P. Krogstrup, R. M. Lutchyn, C. M. Marcus, *Flux-induced topological superconductivity in full-shell nanowires*, *Science* **367**, 1442 (2020).
- [84] R. M. Lutchyn, E. P. A. M. Bakkers, L. P. Kouwenhoven, P. Krogstrup, C. M. Marcus, and Y. Oreg, *Majorana zero modes in superconductor-semiconductor heterostructures*, *Nat. Rev. Mater.* **3**, 52 (2018).
- [85] J.-P. Xu, M.-X. Wang, Z. L. Liu, J.-F. Ge, X. Yang, C. Liu, Z. A. Xu, D. Guan, C. L. Gao, D. Qian, Y. Liu, Q.-H. Wang, F.-C. Zhang, Q.-K. Xue, and J.-F. Jia, *Experimental Detection of a Majorana Mode in the core of a Magnetic Vortex inside a Topological Insulator-Superconductor $Bi_2Te_3/NbSe_2$ Heterostructure*, *Phys. Rev. Lett.* **114**, 017001 (2015).
- [86] P. Hosur, P. Ghaemi, R. S. K. Mong, and A. Vishwanath, *Majorana Modes at the Ends of Superconductor Vortices in Doped Topological Insulators*, *Phys. Rev. Lett.* **107**, 097001 (2011).
- [87] D. Wang, L. Kong, P. Fan, H. Chen, S. Zhu, W. Liu, L. Cao, Y. Sun, S. Du, J. Schneeloch, R. Zhong, G. Gu, L. Fu, H. Ding, and H.-J. Gao, *Evidence for Majorana bound states in an iron-based superconductor*, *Science* **362**, 333 (2018).
- [88] S. Das Sarma, M. Freedman, and C. Nayak, *Topologically Protected Qubits from a Possible Non-Abelian Fractional Quantum Hall State*, *Phys. Rev. Lett.* **94**, 166802 (2005).
- [89] P.-G. de Gennes, *Physique des basses températures Champ critique d'une boucle supraconductrice ramifiée*, *C. R. Acad. Sci. Paris* **292**, 279 (1981).

- [90] Y. Liu, Yu. Zadorozhny, M. M. Rosario, B. Y. Rock, P. T. Carrigan, H. Wang, *Destruction of the Global Phase Coherence in Ultrathin, Doubly Connected Superconducting Cylinders*, *Science* **294**, 2332 (2001).
- [91] I. Sternfeld, E. Levy, M. Eshkol, A. Tsukernik, M. Karpovski, H. Shtrikman, A. Kretinin, and A. Palevski, *Magnetoresistance Oscillations of Superconducting Al-Film Cylinders Covering InAs Nanowires below the Quantum Critical Point*, *Phys. Rev. Lett.* **107**, 037001 (2011).
- [92] B. van Heck, R. M. Lutchyn, and L. I. Glazman, *Conductance of a proximitized nanowire in the Coulomb blockade regime*, *Phys. Rev. B* **93**, 235431 (2016).
- [93] B. D. Woods, S. Das Sarma, T. D. Stanescu, *Electronic structure of full-shell InAs/Al hybrid semiconductor-superconductor nanowires: Spin-orbit coupling and topological phase space*, *Phys. Rev. B* **99**, 161118(R) (2019).
- [94] J-D. Pillet, C. H. L. Quay, P. Morfin, C. Bena, A. Levy Yeyati, and P. Joyez, *Andreev bound states in supercurrent-carrying carbon nanotubes revealed*, *Nat. Phys.* **6**, 965 (2010).
- [95] W. Chang, V. E. Manucharyan, T. S. Jespersen, J. Nygård, and C. M. Marcus, *Tunneling Spectroscopy of Quasiparticle Bound States in a Spinful Josephson Junction*, *Phys. Rev. Lett.* **110**, 217005 (2013).
- [96] L. Bretheau, J. I-J. Wang, R. Pisoni, K. Watanabe, T. Taniguchi, and P. Jarillo-Herrero, *Tunnelling spectroscopy of Andreev states in graphene*, *Nat. Phys.* **13**, 756 (2017).
- [97] A. Altland and M. R. Zirnbauer, *Nonstandard symmetry classes in mesoscopic normal-superconducting hybrid structures*, *Phys. Rev. B* **55**, 1142 (1997).

- [98] M. Hell, M. Leijnse, and K. Flensberg, *Two-Dimensional Platform for Networks of Majorana Bound States*, Phys. Rev. Lett. **118**, 107701 (2017).
- [99] F. Pientka, A. Keselman, E. Berg, A. Yacoby, A. Stern, and B. I. Halperin, *Topological Superconductivity in a Planar Josephson Junction*, Phys. Rev. X **7**, 021032 (2017).
- [100] P. Kotetes, *Topological superconductivity in Rashba semiconductors without a Zeeman field*, Phys. Rev. B **92**, 014514 (2015).
- [101] E. B. Hansen, J. Danon, and K. Flensberg, *Phase-tunable Majorana bound states in a topological N-SNS junction*, Phys. Rev. B **93**, 094501 (2016).
- [102] T. D. Stanescu, A. Sitek, and A. Manolescu, *Robust topological phase in proximitized core-shell nanowires coupled to multiple superconductors*, Beilstein J. Nanotechnol. **9**, 1512 (2018).
- [103] B. van Heck, S. Mi, and A. R. Akhmerov, *Single fermion manipulation via superconducting phase differences in multiterminal Josephson junctions*, Phys. Rev. B **90**, 155450 (2014).
- [104] R.-P. Riwar, M. Houzet, J. S. Meyer, and Y. V. Nazarov, *Multi-terminal Josephson junctions as topological matter*, Nat. Commun. **7**, 11167 (2016).
- [105] J. M. Gordon, C. J. Lobb, and M. Tinkham, *Divergent phase-breaking rate in aluminum films from magnetoconductance measurements*, Phys. Rev. B **29**, 5232(R) (1984).
- [106] C. Kittel, *Introduction to Solid State Physics*, New Delhi: Wiley, ed. 8 (2005).
- [107] G. Schweite, Y. Oreg, *Persistent Current in Small Superconducting Rings*, Phys. Rev. Lett. **103**, 037001 (2009).

- [108] C. Caroli, P. G. de Gennes, and J. Matricon, *Bound Fermion states on a vortex line in a type II superconductor*, Phys. Lett. **9**, 307 (1964).
- [109] A. Vuik, B. Nijholt, A. R. Akhmerov, M. Wimmer, *Reproducing topological properties with quasi-Majorana states*, SciPost Phys. **7**, 061 (2019).
- [110] E. C. T. O'Farrell, A. C. C. Drachmann, M. Hell, A. Fornieri, A. M. Whiticar, E. B. Hansen, S. Gronin, G. C. Gardener, C. Thomas, M. J. Manfra, K. Flensberg, C. M. Marcus, and F. Nichele, *Hybridization of Subgap States in One-Dimensional Superconductor-Semiconductor Coulomb Islands*, Phys. Rev. Lett. **121**, 256803 (2018).
- [111] J. Shen, S. Heedt, F. Borsoi, B. van Heck, S. Gazibegovic, R. L. M. Op het Veld, D. Car, J. A. Logan, M. Pendharkar, S. J. J. Ramakers, G. Wang, D. Xu, D. Bouman, A. Geresdi, C. J. Palmstrøm, E. P. A. M. Bakkers, and L. P. Kouwenhoven, *Parity transitions in the superconducting ground state of hybrid InSb-Al Coulomb islands*, Nat. Commun. **9**, 4801 (2018).
- [112] C. Moore, T. D. Stanescu, and S. Tewari, *Two-terminal charge tunneling: Disentangling Majorana zero modes from partially separated Andreev bound states in semiconductor-superconductor heterostructures*, Phys. Rev. B **97**, 165302 (2018).
- [113] F. W. J. Hekking, L. I. Glazman, K. A. Matveev, and R. I. Shekhter, *Coulomb blockade of two-electron tunneling*, Phys. Rev. Lett. **70**, 4138 (1993).
- [114] J. M. Hergenrother, M. T. Tuominen, and M. Tinkham, *Charge transport by Andreev reflection through a mesoscopic superconducting island*, Phys. Rev. Lett. **72**, 1742 (1994).

- [115] A. P. Higginbotham, S. M. Albrecht, G. Kiršanskas, W. Chang, F. Kuemmeth, P. Krogstrup, T. S. Jespersen, J. Nygård, K. Flensberg, and C. M. Marcus, *Parity lifetime of bound states in a proximitized semiconductor nanowire*, Nat. Phys. **11**, 1017 (2015).
- [116] J. M. Thijssen, H. S. J. Van der Zant, *Charge transport and single-electron effects in nanoscale systems*, Phys. Status Solidi **245**, 1455 (2008).
- [117] E. B. Hansen, J. Danon, and K. Flensberg, *Probing electron-hole components of subgap states in Coulomb blockaded Majorana islands*, Phys. Rev. B **97**, 041411(R) (2018).
- [118] T. D. Stanescu, R. M. Lutchyn, and S. Das Sarma, *Majorana fermions in semiconductor nanowires*, Phys. Rev. B **84**, 144522 (2011).
- [119] S. Nadj-Perge, I. K. Drozdov, B. A. Bernevig, and A. Yazdani, *Proposal for realizing Majorana fermions in chains of magnetic atoms on a superconductor*, Phys. Rev. B **88**, 020407(R) (2013).
- [120] Y. Peng, F. Pientka, L. I. Glazman, and F. von Oppen, *Strong Localization of Majorana End States in Chains of Magnetic Adatoms*, Phys. Rev. Lett. **114**, 106801 (2015).
- [121] S. Vaitiekėnas, P. Krogstrup, and C. M. Marcus, *Anomalous Metallic Phase in Tunable Destructive Superconductors*, Phys. Rev. B **101**, 060507(R) (2020).
- [122] S. L. Sondhi, S. M. Girvin, J. P. Carini, and D. Shahar, *Continuous quantum phase transitions*, Rev. Mod. Phys. **69**, 315 (1997).
- [123] T. Vojta, *Quantum phase transitions in electronic systems*, Ann. Phys. **9**, 403 (2000).

- [124] N. Shah and A. Lopatin, *Microscopic analysis of the superconducting quantum critical point: Finite-temperature crossovers in transport near a pair-breaking quantum phase transition*, Phys. Rev. B **76**, 094511 (2007).
- [125] Q. Si and F. Steglich, *Heavy Fermions and Quantum Phase Transitions*, Science **329**, 1161 (2010).
- [126] M. R. Norman, *The Challenge of Unconventional Superconductivity*, Science **332**, 196 (2011).
- [127] A. Del Maestro, B. Rosenow and S. Sachdev, *Theory of the pair-breaking superconductor-metal transition in nanowires*, Ann. Phys. **324**, 523 (2009).
- [128] A. M. Goldman, *Superconductor—insulator transitions*, Int. J. Mod. Phys. B **24**, 4081 (2010).
- [129] A. Kapitulnik, S. A. Kivelson, and B. Spivak, *Anomalous metals: Failed superconductors*, Rev. Mod. Phys. **91**, 011002 (2019).
- [130] A. Bezryadin, C. N. Lau, and M. Tinkham, *Quantum suppression of superconductivity in ultrathin nanowires*, Nature **404**, 971 (2000).
- [131] A. D. Zaikin, D. S. Golubev, A. van Otterlo, and G. T. Zimányi, *Quantum Phase Slips and Transport in Ultrathin Superconducting Wires*, Phys. Rev. Lett. **78**, 1552 (1997).
- [132] O. V. Astafiev, L. B. Ioffe, S. Kafanov, Yu. A. Pashkin, K. Yu. Arutyunov, D. Shahar, O. Cohen, and J. S. Tsai, *Coherent quantum phase slip*, Nature **484**, 355 (2012).
- [133] J. E. Mooij and C. J. P. M. Harmans, *Phase-slip flux qubits*, N. J. Phys. **7**, 219 (2005).

- [134] B. S. Deaver Jr. and W. M. Fairbanks, *Experimental Evidence for Quantized Flux in Superconducting Cylinders*, Phys. Rev. Lett. **7**, 43 (1961).
- [135] H. Doll and M. Näbauer, *Experimental Proof of Magnetic Flux Quantization in a Superconducting Ring*, Phys. Rev. Lett. **7**, 51 (1961).
- [136] D. H. Douglass Jr. *Properties of a Thin Hollow Superconducting Cylinder*, Phys. Rev. **132**, 513 (1963).
- [137] R. M. Arutyunyan and G. F. Zharkov, *Thin-wall current-carrying superconducting cylinder in a magnetic field*, Zh. Eksp. Teor. Fiz. **79**, 245 (1980).
- [138] V. H. Dao and L. F. Chibotaru, *Destruction of global coherence in long superconducting nanocylinders*, Phys. Rev. B **79**, 134524 (2009).
- [139] O. Vafek, M. R. Beasley, and S. A. Kivelson, *Disorder induced non-Fermi liquid near a metal-superconductor quantum phase transition*, arXiv:0505688 (2005).
- [140] A. V. Lopatin, N. Shah, and V. M. Vinokur, *Fluctuation conductivity of thin films and nanowires near a parallel-field-tuned superconducting quantum phase transition*, Phys. Rev. Lett. **94**, 037003 (2005).
- [141] A. A. Abrikosov and L. P. Gorkov, *Contribution to the Theory of Superconducting Alloys with Paramagnetic Impurities*, Sov. Phys. JETP **12**, 1243 (1961).
- [142] N. A. Court, A. J. Ferguson and R. G. Clark, *Energy gap measurement of nanostructured aluminium thin films for single Cooper-pair devices*, Supercond. Sci. Technol. **21**, 015013 (2008).

- [143] J. Bardeen, *Critical Fields and Currents in Superconductors*, Rev. Mod. Phys. **34**, 667 (1962).
- [144] A. Rogachev, A. T. Bollinger, and A. Bezryadin, *Influence of High Magnetic Fields on the Superconducting Transition of One-Dimensional Nb and MoGe Nanowires*, Phys. Rev. Lett. **94**, 017004 (2005).
- [145] M. Vanević and Y. V. Nazarov, *Quantum Phase Slips in Superconducting Wires with Weak Inhomogeneities*, Phys. Rev. Lett. **108**, 187002 (2012).
- [146] S. Vaitiekėnas, A. M. Whiticar, M.-T. Deng, F. Krizek, J. E. Sestoft, C. J. Palmstrøm, S. Marti-Sanchez, J. Arbiol, P. Krogstrup, L. Casparis, and C. M. Marcus, *Selective-Area-Grown Semiconductor-Superconductor Hybrids: A Basis for Topological Networks*, Phys. Rev. Lett. **121**, 147701 (2018).
- [147] K. Flensberg, *Non-Abelian Operations on Majorana Fermions via Single-Charge Control*, Phys. Rev. Lett. **106**, 090503 (2011).
- [148] S. Plugge, A. Rasmussen, R. Egger, and K. Flensberg, *Majorana box qubits*, New J. Phys. **19**, 012001 (2017).
- [149] S. Vijay and L. Fu, *Teleportation-based quantum information processing with Majorana zero modes*, Phys. Rev. B. **94**, 235446 (2016).
- [150] S. Gazibegovic, D. Car, H. Zhang, S. C. Balk, J. A. Logan, M. W. A. de Moor, M. C. Cassidy, R. Schmits, D. Xu, G. Wang, P. Krogstrup, R. L. M. Op het Veld, K. Zuo, Y. Vos, J. Shen, D. Bouman, B. Shojaei, D. Pennachio, J. S. Lee, P. J. van Veldhoven, S. Koelling, M. A. Verheijen, L. P. Kouwenhoven, C. J. Palmstrøm, and E. P. A. M. Bakkers, *Epitaxy of advanced nanowire quantum devices*, Nature **548**, 434 (2017).

- [151] J. Shabani, M. Kjaergaard, H. J. Suominen, Y. Kim, F. Nichele, K. Pakrouski, T. Stankevic, R. M. Lutchyn, P. Krogstrup, R. Feidenhans'l, S. Kraemer, C. Nayak, M. Troyer, C. M. Marcus, and C. J. Palmstrøm, *Two-dimensional epitaxial superconductor-semiconductor heterostructures: A platform for topological superconducting networks*, Phys. Rev. B **93**, 155402 (2016).
- [152] M. Kjaergaard, F. Nichele, H. J. Suominen, M. P. Nowak, M. Wimmer, A. R. Akhmerov, J. A. Folk, K. Flensberg, J. Shabani, C. J. Palmstrøm, and C. M. Marcus, *Nat. Commun. Quantized conductance doubling and hard gap in a two-dimensional semiconductor-superconductor heterostructure*, **7**, 12841 (2016).
- [153] H. J. Suominen, M. Kjaergaard, A. R. Hamilton, J. Shabani, C. J. Palmstrøm, C. M. Marcus, and F. Nichele, *Zero-Energy Modes from Coalescing Andreev States in a Two-Dimensional Semiconductor-Superconductor Hybrid Platform*, Phys. Rev. Lett. **119**, 176805 (2017).
- [154] F. Nichele, A. C. C. Drachmann,¹ A. M. Whiticar, E. C. T. O'Farrell,¹ H. J. Suominen, A. Fornieri, T. Wang, G. C. Gardner, C. Thomas, A. T. Hatke, P. Krogstrup, M. J. Manfra, K. Flensberg, and C. M. Marcus, *Scaling of Majorana Zero-Bias Conductance Peaks*, Phys. Rev. Lett. **119**, 136803 (2017).
- [155] F. Krizek, J. E. Sestoft, P. Aseev, S. Marti-Sanchez, S. Vaitiekėnas, L. Casparis, S. A. Khan, Y. Liu, T. Stankevič, A. M. Whiticar, A. Fursina, F. Boekhout, R. Koops, E. Uccelli, L. P. Kouwenhoven, C. M. Marcus, J. Arbiol, P. Krogstrup, *Field effect enhancement in buffered quantum nanowire networks*, Phys. Rev. Mater. **2**, 093401 (2018).
- [156] M. T. Deng, C. L. Yu, G. Y. Huang, M. Larsson, P. Caroff, and H. Q. Xu, *Anomalous Zero-Bias Conductance Peak in a Nb-InSb Nanowire-Nb Hybrid Device*, Nano Lett. **12**, 6414 (2012).

- [157] H. Zhang, C.-X. Liu, S. Gazibegovic, D. Xu, J. A. Logan, G. Wang, N. van Loo, J. D. S. Bommer, M. W. A. de Moor, D. Car, R. L. M. Op het Veld, P. J. van Veldhoven, S. Koelling, M. A. Verheijen, M. Pendharkar, D. J. Pennachio, B. Shojaei, J. S. Lee, C. J. Palmstrøm, E. P. A. M. Bakkers, S. Das Sarma, L. P. Kouwenhoven, *Quantized Majorana conductance*, *Nature* **556**, 74 (2018).
- [158] J. E. Sestoft, T. Kanne, A. N. Gejl, M. von Soosten, J. S. Yodh, D. Sherman, B. Tarasinski, M. Wimmer, E. Johnson, M.-T. Deng, J. Nygård, T. S. Jespersen, C. M. Marcus, P. Krogstrup, *Engineering hybrid epitaxial InAsSb/Al nanowires for stronger topological protection*, *Phys. Rev. Mater.* **2**, 044202 (2018).
- [159] D. Sherman, J. S. Yodh, S. M. Albrecht, J. Nygård, P. Krogstrup, and C. M. Marcus, *Normal, superconducting and topological regimes of hybrid double quantum dots*, *Nat. Nanotechnol.* **12**, 212 (2017).
- [160] F. Krizek, T. Kanne, D. Razmadze, E. Johnson, J. Nygård, C. M. Marcus, and P. Krogstrup, *Growth of InAs Wurtzite Nanocrosses from Hexagonal and Cubic Basis*, *Nano Lett.* **17**, 6090 (2017).
- [161] H. Zhang, Ö. Gül, S. Conesa-Boj, M. P. Nowak, M. Wimmer, K. Zuo, V. Mourik, F. K. de Vries, J. van Veen, M. W. A. de Moor, J. D. S. Bommer, D. J. van Woerkom, D. Car, S. R. Plissard, E. P. A. M. Bakkers, M. Quintero-Pérez, M. C. Cassidy, S. Koelling, S. Goswami, K. Watanabe, T. Taniguchi, and L. P. Kouwenhoven, *Ballistic superconductivity in semiconductor nanowires*, *Nat. Commun.* **8**, 16025 (2017).
- [162] C. W. J. Beenakker, *Quantum transport in semiconductor-superconductor microjunctions*, *Phys. Rev. B* **46**, 12841 (1992).

- [163] M. T. Tuominen, J. M. Hergenrother, T. S. Tighe, and M. Tinkham, *Experimental evidence for parity-based $2e$ periodicity in a superconducting single-electron tunneling transistor*, Phys. Rev. Lett. **69**, 1997 (1992).
- [164] P. Lafarge, P. Joyez, D. Esteve, C. Urbina, and M. H. Devoret, *Measurement of the even-odd free-energy difference of an isolated superconductor*, Phys. Rev. Lett. **70**, 994 (1993).
- [165] C.-K. Chiu, J. D. Sau, and S. Das Sarma, *Conductance of a superconducting Coulomb-blockaded Majorana nanowire*, Phys. Rev. B. **96**, 054504 (2017).
- [166] Ö. Gül, D. J. van Woerkom, I. van Weperen, D. Car, S. R. Plissard, E. P. A. M. Bakkers, and L. P. Kouwenhoven, *Towards high mobility InSb nanowire devices*, Nanotechnology **26**, 215202 (2015).
- [167] J. S. Lee, S. Choi, M. Pendharkar, D. J. Pennachio, B. Markman, M. Seas, S. Koelling, M. A. Verheijen, L. Casparis, K. D. Petersson, I. Petkovic, V. Schaller, M. J. W. Rodwell, C. M. Marcus, P. Krogstrup, L. P. Kouwenhoven, E. P. A. M. Bakkers, and C. J. Palmstrøm, *Selective-area chemical beam epitaxy of in-plane InAs one-dimensional channels grown on InP(001), InP(111)B, and InP(011) surfaces*, Phys. Rev. Mater. **3**, 084606 (2019).
- [168] C. Kurdak, A. Chang, A. Chin, and T. Chang, *Quantum interference effects and spin-orbit interaction in quasi-one-dimensional wires and rings*, Phys. Rev. B. **46**, 6846 (1992).
- [169] A. Sasaki, S. Nonaka, Y. Kunihashi, M. Kohda, T. Bauernfeind, T. Dollinger, and J. Nitta, *Direct determination of spin-orbit interaction coefficients and realization of the persistent spin helix symmetry*, Nat. Nanotechnol. **9**, 703 (2014).

-
- [170] T. S. Jespersen, M. L. Polianski, C. B. Sørensen, K. Flensberg, and J. Nygård, *Mesoscopic conductance fluctuations in InAs nanowire-based SNS junctions*, *New J. Phys.* **11**, 113025 (2009).
- [171] T. Ludwig and A. D. Mirlin, *Interaction-induced dephasing of Aharonov-Bohm oscillations*, *Phys. Rev. B.* **69**, 193306 (2004).
- [172] M. Ferrier, A. C. H. Rowe, S. Guéron, H. Bouchiat, C. Texier, and G. Montambaux, *Geometrical Dependence of Decoherence by Electronic Interactions in a GaAs/GaAlAs Square Network*, *Phys. Rev. Lett.* **100**, 146802 (2008).
- [173] QDevil ApS, www.qdevil.com.
- [174] C. W. J. Beenakker, *Theory of Coulomb-blockade oscillations in the conductance of a quantum dot*, *Phys. Rev. B* **44**, 1646 (1991).

